Østen Jensen

Behaviour of aluminium extrusion subjected to axial loading

Doktoravhandling
for graden doktor ingeniør

Trondheim, mars 2005

Norges teknisk-naturvitenskapelige universitet
Fakultet for ingeniørvitenskap og teknologi
Institutt for konstruksjonsteknikk

◙ NTNU

Abstract

This thesis deals with the transition from progressive to global buckling of axially loaded thin-walled aluminium extrusions. The behaviour of the extrusions was studied experimentally and numerically using the finite element code LS-DYNA. Material tests were performed to provide stress-strain characteristics of the material to be used in the numerical simulations.

The transition between progressive and global buckling of axially loaded aluminium extrusions in alloy AA6060 temper T6 was studied by quasi-static and dynamic tests. The primary variables in the tests were the local (b/h = 17.78 - 40) and global (L/b = 5 - 24) slenderness of the extruded members and the impact velocity. The critical global slenderness is defined as the slenderness where direct global buckling or a transition from progressive to global buckling occurs. In the quasi-static tests the critical global slenderness was found to be an increasing function of the local slenderness. In contrast, the critical global slenderness was a decreasing function of the local slenderness when the impact velocity was 20 m/s. The energy absorption was found to be very dependent on the collapse mode. Significantly more energy is absorbed in the progressive buckling mode than in the global bending mode. In the case of transition from progressive to global buckling, the energy absorption depends on the time of transition. The difference in energy absorption between the different deformation modes decreases for increasing impact velocity. This is due to inertia forces preventing the direct global buckling mode and the early transition from progressive to global buckling.

In addition to experimental tests, numerical simulations using LS-DYNA were carried out. A numerical model was validated against the experimental tests. Good agreement between the progressive buckling pattern in the numerical simulations and experimental tests was found. The numerical simulations were capable of

giving a relatively accurate prediction of the collapse mode found in the experimental tests. However, the numerical model underestimated the mean force level found in the experimental tests. Thus, additional simulations were performed to investigate the influence from some key parameter on the mean force level. Stabilization of the behaviour and increasing the critical global slenderness by use of a trigger has been investigated. The introduction of a heat affected zone at the impacted end caused the progressive buckling to start from this end. This had a positive effect on the critical buckling length.

Finally the maximum and mean forces found in the experimental tests were compared to existing analytical expressions and a design code. A relatively good agreement was found. The collapse modes observed in the quasi-static experimental tests were compared to analytical models for predicting the response of axially loaded aluminium extrusions. The analytical models for predicting the global buckling gave relatively accurate results.

Acknowledgement

Contents

Notation

A	cross-sectional area
a, b	plate length and width
A_c	area enclosed by the cross-section
A_e	effective cross-section
b	width of the test specimen
b_m	$b_m = b - h$
C_{ine}	dynamic amplification constant
D	plate stiffness
$d(t), \dot{d}(t), \ddot{d}(t)$	rigid body displacement, velocity and acceleration
$d(t_b), d_b$	calculated axial displacement at buffer activation time
d_{max}	maximum deformation
E	modulus of elasticity
$EI, \overline{EI}, EI^*$	bending stiffness, bending stiffness of compressed column and bending stiffness of partly compressed column
E_p	energy absorbed at bottoming out for a member collapsing progressively
E_s	secant modulus
E_r	double modulus
E_t	tangent modulus
E_T	energy absorbed at transition
e_l	engineering strain in length direction
e_u	engineering strain at maximum engineering stress
F, $F(t)$	axial force, dynamic force
F_{avg}^0	dynamic mean force
f_0	characteristic strength in Eurocode 9
f_p	proportionality limit of the material
h, h_1, h_2, h_3, h_4	wall thickness, nominal wall thickness

h_0, h	initial and final thickness of gauge area
H	potential of external load
$h_{contact}$	thickness used in contact formulation
h_{eff}	effective thickness
$h_{initial}$	initial wall thickness
I	second moment of area
k_{EI}	reduction factor, bending stiffness
k_1, k_2	reduction factors, asymmetry and mechanical imperfections respectively
k_σ	buckling load coefficient
L	free length of the test specimen
$L_1, L_2, \overline{L}$	length of deformed, undeformed and total length of partly compressed column
l	length
l_b	measured distance to buffer
l_{edge}	element side edge length
L_k	buckling length
m	hardening parameter (Ramberg Osgood)
M	moment
M_B	mass of projectile
M_N	nose mass of load cell
M_{cap}, M_p	moment capacity
M_y	moment at "yielding" in deformed part of column
n	hardening parameter (power law)
N	axial load
$N_{b,Rd}$	critical buckling load
N_{cr}	elastic column buckling load
N_E	Euler buckling load
N_m	mean force (progressive buckling)
N_p	axial plastic load capacity
$P(t)$	measured force (at the location of the strain gauges)

P_{max}	maximum load
P_m	mean force
P_m^*	energy absorbed until transition divided by bottoming out length
R	plastic strain ratio
t	time
t_b	buffer activation time
s	engineering stress
s_1	characteristic stress
U	internal elastic energy
u	total deflection
u_0	initial imperfection
v_0	impact velocity
V_k, V_m	strain rate constants
W	elastic section modulus
w	out of plane deflection
w_0, w	initial and final width of gauge area
w_T	deformation at time of transition
α	imperfection factor according to Eurocode 9
χ	reduction factor for flexural buckling
δ	total deformation, total deflection amplitude
δ_0	initial imperfection amplitude
δ_{00}, δ_{0f}	initial and final imperfection amplitude in collapse model
δ_g, δ_l	global and local initial imperfections
Δ_b	accuracy parameters
$d\varepsilon_t^p$, $d\varepsilon_w^p$	incremental plastic strains in thickness and width directions
ε^p	true plastic strain
ε_l	true strain in length direction
ε_l^p	true plastic strain in length direction
ε_z	normal strain

ε_0	material parameter in power law hardening curve
ϕ	solidity ratio
γ_{m1}	partial safety factor
η	structural effectiveness
η_e	factor for local buckling in class 4 elements ($\eta_e = A_e/A$)
η_S	plastic reduction factor according to Stowell theory
κ	reduction factor that accounts for welding
λ	proportionality limit, slenderness ratio
$\overline{\lambda}_0$	limit of horizontal plateau according to Eurocode 9
$\overline{\lambda}_k$	reduced slenderness ratio
λ_k	slenderness ratio $\lambda_k = L_k/i$ where $i = \sqrt{I/A}$
$\overline{\lambda}_p$	reduced slenderness ratio for the plate
ν	Poisson's ratio
θ	rotation
ρ_0	density of extrusion material
ρ_c	local buckling coefficient
σ	true stress
σ_0, Q_n, C_n	material constants
σ_0	characteristic stress
$\sigma_{0.2}$	0.2 % proof strength
σ_{cr}	critical stress
$\sigma_{cr,pl}$	critical stress for a plate
$\sigma_{cr,pl}^{el}$	elastic buckling capacity of a plate
$\sigma_{cr,pl}^{pl}$	plastic buckling capacity of a plate
$\sigma_{cr,pl}^{St}$	buckling stress according to Stowell theory
σ_{cr}^{E}	Euler buckling stress
$\sigma_{cr}^{pl,t}$	plastic buckling stress, tangent modulus theory
σ_{global}	global buckling stress
$\sigma_{prog.}$	progressive buckling stress
σ_y	yield stress
σ_{xx}, σ_{yy}	true stress components

σ_z normal stress

ς_f rigid body load factor

1 Introduction

The demand for aluminium has increased drastically during the last 100 years. The automotive industry is a particularly interesting customer for aluminium producers, since environmental demands have forced this rather conservative automotive industry into considering new materials and technical solutions. Reducing the weight of the car is of special importance in order to reduce fuel consumption and consequently lower carbon dioxide emissions. Because of the low density of aluminium compared to steel, a weight reduction of up to 300 kg is possible in a medium size vehicle (1400 kg) with the extensive use of aluminium. This has made the aluminium space frame concept, see Figure 1-1, interesting for the automotive industry. As a result, the average European car contains a variety of cast and extruded aluminium components such as cylinder heads, wheels, radiators, side impact bars, bumper beams and crash boxes. These components typically amount to 65 kg or 6 % of the total weight.

Figure 1-1 Audi A2 space frame.

1.1 Problem definition

As aluminium is a relatively new material in car body design, thorough testing is required to validate its energy absorbing characteristics, since the automotive industry has become increasingly more concerned about safety of the passengers in the case of a crash. In addition to national safety standards, different programmes exist that evaluate the crashworthiness of new cars. These programmes make it easier for the safety focused customer to choose a crashworthy car. For a vehicle to perform well in a New Car Assessment Programme (NCAP) test or in a real life impact, it is important that the energy absorption capabilities are predictable. Thus, these capabilities have to be evaluated in order to ensure the integrity of the passengers' compartment.

1.1.1 Collapse mode of axially loaded thin-walled extrusions

In modern car body design, extruded thin-walled aluminium members are used in crash boxes, bumper beams and space frames. For longitudinal members the energy absorption should take place by extensive folding or progressive buckling of the extruded aluminium members, see Figure 1-2. This is a preferable deformation mode as the energy absorption is at a maximum and the dynamic load shortening characteristics of the members can easily be predicted. However, when increasing the length of the members or changing the thickness, a change in response to either global buckling or a transition mode may occur. This may lead to far less efficient energy absorption and transmission of large forces to other parts of the structure.

1.1.2 Finite element methods and vehicle crashworthiness

Numerical methods such as the finite element method are invaluable tools in the assessment of the crash behaviour of vehicles. Numerical simulations enable evaluation to be made of new materials, technologies and designs without expensive, time consuming testing. The first vehicle impact simulations had only

lumped masses, springs and dampers where the stiffness and other physical properties of each spring had to be found from testing on the corresponding structural component. This has led to an improvement and refinement numerical models used in the finite element method. Nowadays two- and three-dimensional finite elements describe the true geometry and mass of the vehicle. The latest models have approximately 600 000 elements and the number of elements will probably continue to increase.

Even with the improvement of the numerical code it is important to validate the numerical models against physical tests. In the space frame concept the major part of the deformation will take place as a combination of progressive buckling and bending. It is important that the numerical model is capable of handling both these collapse modes. The numerical model should be able to predict the collapse mode with a high level of certainty in order to ensure robust design.

Figure 1-2 Collapse modes for axially loaded thin-walled components; progressive, global and transition mode.

1.2 Previous work

Energy absorption in thin-walled tube-like structures have been extensively studied and comprehensive reviews can be found in the literature (Johnson and Reid, 1978, 1986; Reid, 1993; Alghamdi, 2001; Jones, 2003; Abramowicz, 2003). However, a limited amount of information about the behaviour of long aluminium tubes subjected to axial impact has been found.

Abramowicz and Jones (1984, 1986, 1997) performed static and dynamic tests on steel tubes and found that the critical length/width ratio, i.e. the global slenderness at which the transition to global buckling occurs, increased for increasing width/thickness ratios. Hsu and Jones (2003, 2004) performed experimental tests on cylindrical AA6061-T6 aluminium shells, where the influence from striking mass, initial velocity and specimen length on the behaviour of the tubes was studied. It was found that the inertia properties of the striker have an important effect on the initiation of buckling for high velocity impacts and that the development of the buckling process is sensitive to the initial velocity and the specimen length. Karagiozova and Alves (2004a-b) studied the transition from progressive buckling to global bending of circular shells. Through experimental tests and numerical simulations they found that the critical buckling length was very dependent on the impact velocity (Karagiozova and Alves, 2004a) Simple theoretical models (Karagiozova and Alves, 2004b) were used to analyze the numerical results. Karagiozova (2003) found that variation of the yield stress can change the collapse mode of axially loaded long circular tubes from progressive buckling to global bending. Teramoto and Alves (2004) studied the buckling transition of axially impacted open shells as a function of the impacting mass and velocity. No unique collapse transition was found for the open shells.

A considerable amount of work has been carried out on relatively short tubes that have been subjected to axial impact. Langseth et al. (1996, 1999) found that the tubes folded in a symmetric mode during static testing, while a mixture of local

buckling modes was found in the dynamic tests. The mean dynamic force was higher than the mean static force for a given displacement. Gupta and Abbas (2001) considered the influence from varying wall thickness during the crushing process of relatively short circular tubes. They found that the change in thickness during folding had little effect on the crushing load. Karagiozova et al. (2001, 2000) have carried out numerical studies on progressive buckling and inertia effects, and found the energy absorption to be both mass and velocity sensitive. Larger energies can be absorbed when increasing the impact velocity and reducing the striking mass. The influence from stress wave propagation on the initiation of dynamic progressive and dynamic plastic buckling were studied numerically by Karagiozova and Jones (2001, 2000). Su et al. (1995) studied the influence from inertia and strain rates on the behaviour of energy absorbing structures. The dynamic behaviour differed considerably from the quasi-static behaviour even when strain rate effects were excluded.

It can be concluded from existing studies that the response of thin-walled extrusions to axial impact depends on several factors, such as:

> Geometry: length, width and thickness of the member.
> Material properties: elasticity modulus, yield stress and strain hardening.
> Boundary conditions: clamped, pinned or free.
> Impact velocity: strain rate and inertia effects.
> Imperfections: amplitude and shape.

1.3   Objectives and scope

In the present study the main objectives have been to investigate the behaviour of axially loaded square thin-walled aluminium extrusions. The objectives are met by a combination of laboratory tests and numerical simulations. The experiments are used to validate a numerical model for parametric studies.

The following activities were defined.

> ➢ Material tests were performed to provide material data for analytical modelling and numerical simulations. To establish the variation in material parameters all thicknesses were tested. In addition three different directions were tested for one thickness to evaluate the anisotropy of the material.

> ➢ Experimental investigations were carried out on the behaviour of axially loaded thin-walled aluminium extrusions. Four different thicknesses were tested quasi-statically and at two different impact velocities. The influence of specimen geometry and impact velocity on the response was investigated.

> ➢ A numerical model of quasi-static and dynamic axial loading of aluminium extrusion has been established for validation purposes. Focus was placed on the force-deformation response and the ability to predict the correct deformation mode.

> ➢ The numerical model was used in a parametric study in which the influence from velocity, material properties and triggers were investigated.

> ➢ A comparison between the experimental results and existing analytical methods and the design code for aluminium structures Eurocode 9 were performed.

> ➢ An analytical model for the response of axially loaded thin-walled aluminium extrusions has been established and compared to the experimental results.

2   Material properties

This chapter provides stress-strain characteristics of extruded profiles made of aluminium alloy 6060 temper T6. This is an Al-Mg-Si-alloy with the nominal composition shown in Table 2-1. Specimens were cut from different directions in order to study the anisotropy of the material.

The material tests were performed to provide material data for analytical modelling and numerical simulations.

2.1   Uniaxial tensile tests

2.1.1   Test specimen and test setup

The aluminium alloy AA6060-T6 has been characterized by means of uniaxial tensile tests. Three test specimens were cut in the extrusion direction from members with different wall thicknesses. The geometry of the test specimens is depicted in Figure 2-1.

In order to investigate the anisotropy of the material, three test specimens were machined from each of the 0°, 45° and 90° directions of the 3.5 mm thick extrusions, where 0° is the extruding direction. Owing to the size of the aluminium profile, small test specimens with an overall length of 80 mm had to be used, see Figure 2-2.

Table 2-1 Chemical composition of aluminium alloy 6060.

Si	Fe	Mg	Mn	Cu	Ti	B	Zn	Al
0.44 %	0.22 %	0.48 %	0.016 %	0.003 %	0.007 %	0.001 %	0.01 %	balance
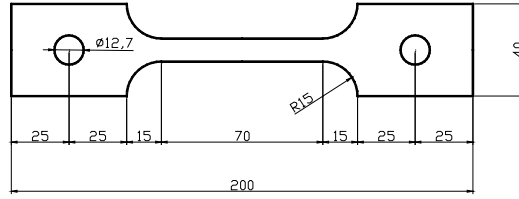
Figure 2-1 Large test specimens for tensile testing.
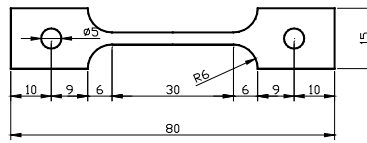
Figure 2-2 Small test specimens for tensile testing.

The material tests were performed in an Instron hydraulic testing machine under displacement control at a constant strain rate of approximately $5 \cdot 10^{-4} s^{-1}$. The length strain was measured with an extensometer, which was attached until fracture.

2.1.2 Identification procedure

For each test the true stress σ and the true strain in the length direction ε_l were calculated as

$$\sigma = s(1 + e_l) \qquad (2\text{-}1)$$

$$\varepsilon_l = \ln(1 + e_l) \qquad (2\text{-}2)$$

where s and e_l are the corresponding engineering values of stress and strain. From these values true plastic strain was calculated as

$$\varepsilon_l^p = \varepsilon_l - \frac{\sigma}{E} \qquad (2\text{-}3)$$

where E is the modulus of elasticity and superscript p indicates plastic strain. It was chosen to represent the stress-strain curves of the material in a parametric form of the type

$$\sigma_{eff} = \sigma_0 + \sum_{i=1}^{2} Q_i (1 - \exp(-C_i \varepsilon_{eff}^p)) \qquad (2\text{-}4)$$

where the constants σ_0, Q_i and C_i were obtained using the method of least squares. Table 2-2 compiles the material parameters and 0.2 % proof strengths obtained from tensile tests in the 0º direction for all thicknesses and from tensile tests in the 0º, 45º and 90º directions for 3.5 mm thickness.

The plastic strain ratio is defined as the ratio of the width-to-thickness incremental plastic strain and gives information on the plastic flow of the material. Mathematically it is expressed as (Hosford and Caddel, 1993)

$$R = \frac{d\varepsilon_w^p}{d\varepsilon_t^p} \qquad (2\text{-}5)$$

where $d\varepsilon_w^p$ and $d\varepsilon_t^p$ are the incremental plastic strains in the width and thickness directions, respectively. Since only the longitudinal strain was measured during the test, the incremental width and thickness strains were not available. However, assuming that the plastic strain ratio is constant during straining, which is often a good approximation, the R-value can be estimated based on measurements of width and thickness outside the necking area as (Hosford and Caddel, 1993)

$$R \approx \frac{\ln\left(w_0 / w\right)}{\ln\left(h_0 / h\right)} \qquad (2\text{-}6)$$

where w_0 and w are the initial and final width and h_0 and h are the initial and final thickness of the gauge section.

2.1.3   Test results

The measured average R-values were in the range of 0.43 – 0.52, 0.20 – 0.29 and 1.28 - 1.48 for the 0º, 45º and 90º directions respectively. The strain ratio, R, equals unity for an isotropic material. Hence, the measured R-values clearly indicate anisotropy in plastic flow for AA6060-T6 alloy. In the 0º and 45º directions, the thickness strain is greater than the width strain, while in the 90º direction the width strain is the largest. These data are important in the identification of an anisotropic yield criterion for the alloy when the associated flow rule is accepted (Hosford and Caddel, 1993).

Typical true stress-true strain curves for the different thicknesses are shown in Figure 2-3. The results from all material tests are presented in Appendix A. Only small variations were observed between the stress-strain curves for the same thickness. The figure shows that the AA6060-T6 alloy experiences small variations in strength for specimens with different thickness (see also Table 2-2). The largest difference in 0.2 % proof stress, approximately 5 %, was observed between members with wall thickness of 2.5 mm and 4.5 mm.
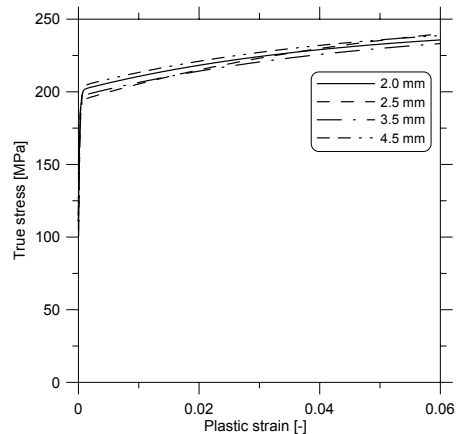
Figure 2-3. Typical true stress vs. true plastic strain curves for different wall thicknesses (0° direction).

Figure 2-4 presents the true stress-strain curves from the 0º, 45º and 90º directions for wall thickness 3.5 mm. Results from all tests in all directions are presented in Appendix A. The scatter in stress-strain curves for the same direction was small. It is evident that the AA6060-T6 alloy experiences insignificant anisotropy in strength, $\sigma_{0.2}$, (see also Table 2-2). The strength in the 90º direction is approximately 2 % higher than the strength in the 45º direction.

Table 2-2 Tensile test data for large specimens with different thickness (0° direction) and small specimens in different directions (3.5 mm thickness).

Thickness/ Direction	σ_0	Q_1	C_1	Q_2	C_2	$\sigma_0 + \sum_i Q_i$	$\sigma_{0.2}$
	[N/mm^2]	[N/mm^2]	[-]	[N/mm^2]	[-]	[N/mm^2]	[N/mm^2]
2.0 mm	122	81	6086	47	24	249	205
2.5 mm	115	79	7565	68	19	262	196
3.5 mm	148	48	10492	49	22	246	199
4.5 mm	90	114	4295	47	24	250	206
0°	128	78	2749	49	21	255	208
45°	166	44	1621	43	19	253	209
90°	167	38	1764	42	20	247	206
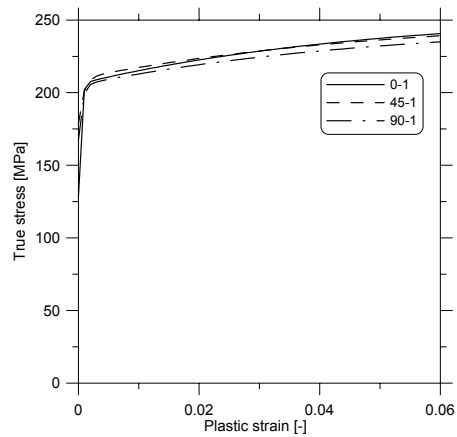
Figure 2-4 Typical true stress vs. true plastic strain curve in the 0°, 45° and 90° directions (3.5 mm thickness).

3 Test set-up

In this chapter the experimental test programme and setup are presented. Extruded aluminium tubes with four different wall thicknesses were tested quasi-statically and dynamically. The experimental data will be used to validate a finite element model used in Chapter 5.

3.1 Test programme and initial measurements

Square thin-walled extrusions made of aluminium alloy AA6060 (a commonly used alloy in the automotive industry) in temper T6 were tested under quasi-static and dynamic axial loading conditions. The test programme is presented in Table 3-1. The wall thickness was varied between four different nominal values: $h_1 = 2.0$ mm, $h_2 = 2.5$ mm, $h_3 = 3.5$ mm and $h_4 = 4.5$ mm. The width of the extrusion was kept constant at a nominal value of 80 mm. The length of the extrusions was varied within the limits specified in Table 3-1 in order to trigger the different deformation modes. None of the specimens were triggered to initiate a particular deformation mode. Prior to testing, the width and wall thickness of the extrusions were measured. The wall thickness was measured using a micrometer at both ends of the extruded members, while the width was measured using a digital slide calliper at both ends and at the mid section. All specimens were measured prior to testing and an average width of 79.84 mm and average thickness of 1.93 mm, 2.47 mm, 3.35 mm and 4.35 mm, respectively, was found. The variation in thickness and width was relatively small for all wall thicknesses. The coefficient of variation (CoV = Standard deviation / average value * 100 %) was in the range 0.6 - 2.2 % for the thickness and 0.05 - 0.13 % for the width; the variation being largest for the specimens with the lowest wall thickness. The length was measured using a measuring tape. The test specimens were clamped at the lower end and friction prevented sideways movement at the top.

Table 3-1 Test specimen geometry and support conditions.

Test set-up	Parameters
Static Hydraulic actuator	Wall thickness 2.0 mm 2.5 mm 3.5 mm 4.5 mm
	Length 454 – 1919 mm
Dynamic	Wall thickness 2.0 mm 2.5 mm 3.5 mm 4.5 mm
	Length 638 – 1920 mm
	Impact velocity and mass 13 m/s and 1400 kg 20 m/s and 600 kg
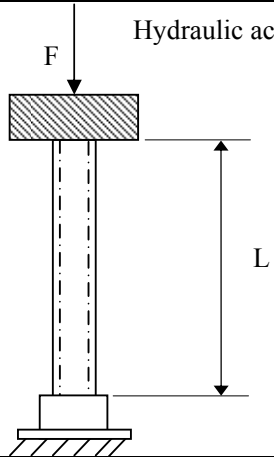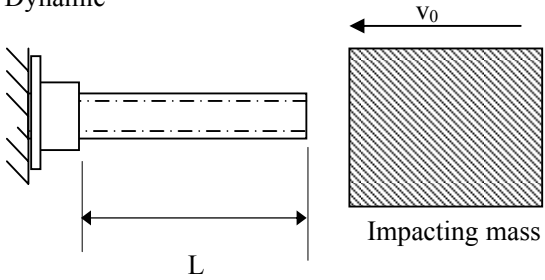
During quasi-static loading the crosshead speed was kept constant at 150 mm/min, whereas the impact tests were carried out while keeping the impact energy constant. The impact velocity was chosen as 13 m/s and 20 m/s with a corresponding mass of the impactor equal to 1400 kg and 600 kg, respectively.

3.2 Quasi-static tests

The quasi-static tests were carried out in a Dartec 500 kN testing machine (accuracy ± 1 % of applied load). The lower 100 mm of the test specimens was fixed by means of the clamping device shown in Figure 3-3c. To prevent local

buckling of the extrusion walls inside the clamping device, a wooden block was inserted at the clamped end. The height of the wooden block was the same as the height of the clamping device. The load was applied through a rigid steel plate connected to the hydraulic actuator to ensure uniform load distribution. Friction between the test specimen and the rigid steel plate prevented sideways movement of the upper end during the tests. The data logging system that was used was running at a constant frequency of 10 Hz, sampling the internal force and displacement signals from the Dartec machine. The load was applied at a constant crosshead speed of 150 mm/min.

3.3 Dynamic tests

3.3.1 Pendulum accelerator

This section provides an overview of the pendulum accelerator, see Figure 3-1, used for dynamic testing. This overview and the description of the operation of the pendulum accelerator given in Section 3.3.4, is based on the description given by Hansen et al. (2003). The test specimens were fixed to the reaction wall using the same clamping device as in the quasi-static tests, see Figure 3-3c. The pendulum accelerates a trolley on rails towards the test specimens. The accelerating system consists of an arm that rotates around a set of bearings, i.e. the arm is free to rotate in the plane of Figure 3-1. Note that the arm is open like a crankshaft at the bearing end. The arm itself is connected to a hydraulic/pneumatic actuator system, which provides the moving force. This system accelerates the trolley up to the desired impact velocity. The trolley traverses the length of the rails and hits the test specimen located at the far end. The impact velocity v_0 of the trolley is measured by means of a photocell system located directly in front of the test specimen.

In general, the test specimen will not have enough capacity to absorb all the kinetic energy of the trolley by itself, i.e. a secondary energy absorbing system is required to prevent bottoming out of the test specimens which will lead to a drastic increase

in force and possible damage to the load cell. The trolley has rigid buffer plates on both sides of the load cell. These buffer plates hit crash boxes fixed to the reaction wall, which ensure the integrity of the load cell. Figure 3-3a shows a plan view of the experimental test set up at the reaction wall.

3.3.2   Trolley and load cell

In order to measure the interface force between the specimen and the impactor, a special purpose load cell was designed, see Figure 3-2. The load cell is machined from one piece of high strength steel with a minimum yield stress of 600 MPa. The central shaft of the load cell is a hollow cylinder with outer diameter 58.5 mm and a wall thickness of 4.25 mm.

The load cell is mounted in the front of the trolley. A detailed view of the trolley is given in Figure 3-3a.
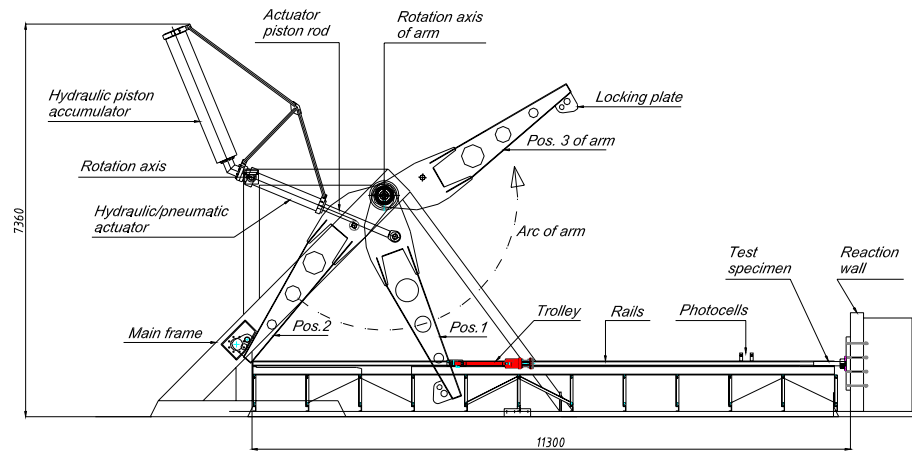
Figure 3-1 Pendulum accelerator.
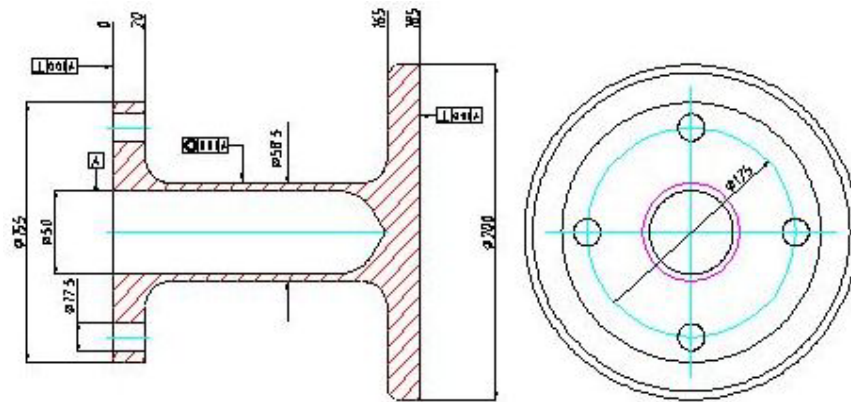
Figure 3-2 Load cell measurements.
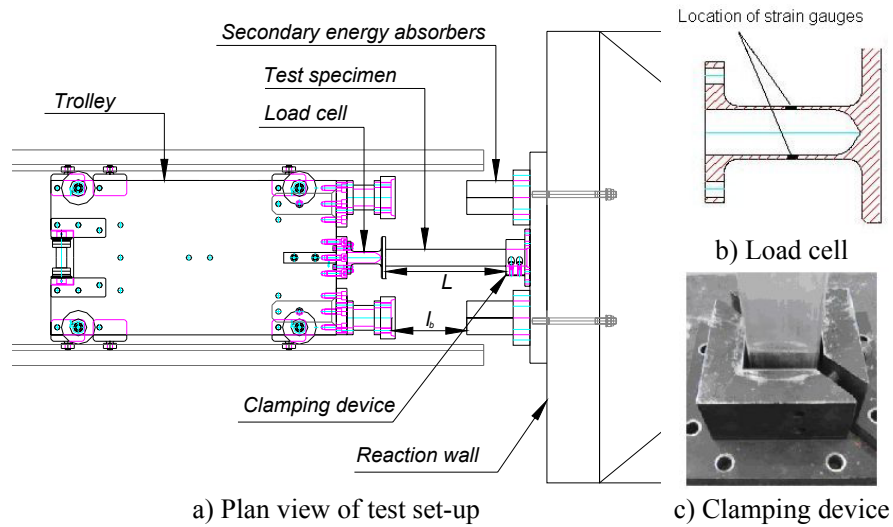
a) Plan view of test set-up   c) Clamping device

Figure 3-3. Test set-up dynamic tests.

The load cell has strain gauges applied for the measurement of the impacting force as function of time. Two strain gauges are located diagonally in the middle of the hollow cylindrical portion of the load cell. The strain gauges applied were of type Tokyo Sokki Kenkyujo FCA-2-11-1L with gauge factor of 2.12, gauge length 2 mm, gauge width 0.9 mm and resistance 120 Ω.

As the load cell is made of high strength steel, it is assumed to behave elastic during impact. Thus, the force-voltage characteristics are obtained statically using a hydraulic actuator.

The mass behind the strain gauges M_B is referred to as the backing mass. The mass of the load cell in front of the strain gauges M_N is called the nose mass. The force recorded by the strain gauges is $P(t)$, whereas the real impact force acting directly on the test specimen is $F(t)$, see Figure 3-4.

The techniques described in the following are established to estimate $F(t)$ and $d(t)$ using the recorded strain-gauge force $P(t)$. Assuming a rigid body motion of the impacting mass, the equations of motion for the backing mass M_B and nose mass M_N are

$$F(t) = (M_B + M_N)\ddot{d} \tag{3-1}$$

$$P(t) = M_B\ddot{d} \Leftrightarrow \ddot{d} = \frac{P(t)}{M_B} \tag{3-2}$$

$$F(t) - P(t) = M_N\ddot{d} \tag{3-3}$$
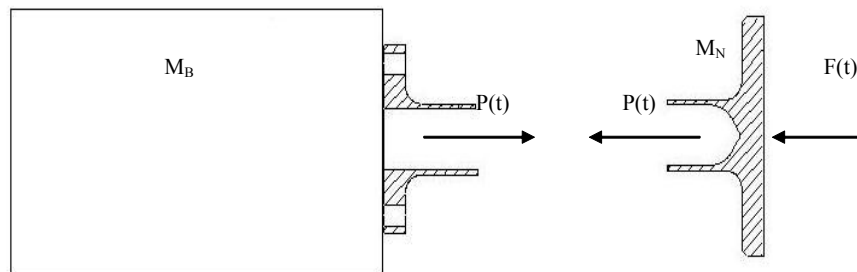
Figure 3-4 Contact force and recorded force.

$$F(t) = P(t) + M_N \ddot{d} = P(t)\left(1 + \frac{M_N}{M_B}\right) = P(t)\varsigma_f \qquad (3\text{-}4)$$

$$\varsigma_f = \left(1 + \frac{M_N}{M_B}\right) \qquad (3\text{-}5)$$

Here ς_f is the rigid-body load factor. The mass of the load cell in front of the strain gauges is 3.8 kg, whereas the backing mass is either 600 kg or 1400 kg depending on the impact velocity chosen giving a rigid body load factor of 1.0063 and 1.0027 respectively. The rigid body velocity and displacement can be expressed as

$$\dot{d}(t) = v_0 + \int \ddot{d}(t)dt \qquad (3\text{-}6)$$

$$d(t) = \int \dot{d}(t)dt \qquad (3\text{-}7)$$

Accuracy control of the measurements is obtained by using information from the high-speed video camera. Assume that the impact starts at $t = 0$ and that the trolley activates the buffer system at time $t = t_b$. From the video recordings it is possible to obtain t_b. Based on the measured force signal $F(t)$, the displacement of the trolley at $t = t_b$ is found from Equation (3-7). The distance from the test specimen activation until the trolley hits the buffers l_b is easily measured prior to each test, see Figure 3-3a. Hence, a reliable measurement is ensured if $d(t_b) \approx l_b$ and the following accuracy parameter is defined

$$\Delta_b = \frac{d(t_b)}{l_b} \qquad (3\text{-}8)$$

The above equations are only valid until the trolley activates buffer system at time $t = t_b$. In some tests the specimens absorbed all the kinetic energy before the trolley activated the buffer system. In these cases the accuracy parameter Δ_b is taken as

the ratio between the calculated maximum displacement of the trolley and the measured permanent deformation of the specimen after impact.

In the dynamic tests there are a lot of elastic stress waves in the load cell propagating through the strain gauges, see Figure 3-5. The force signal has been filtered using a running average. To establish the correct filtering frequency, the test set-up was modelled using LS-DYNA. The force in a cross-section, $P(t)$, at the same location as the strain gauges was compared to the contact force, $F(t)$, and the correct filtering frequency was found using the method of least squares. A sampling rate of 500 000 points per second was used in the impact tests. All experimentally obtained force time curves were smoothed using a moving average algorithm of 385 points, corresponding to a filtering frequency of 1300 Hz. The smoothing algorithm starts the averaging gradually, i.e. in the beginning of the signal the first data point is the original one, the next point is the average of the foregoing point, itself and the subsequent point. This process is continued until reaching the maximum number of smoothing points, here 385. Then 385 points is used in the smoothing of the main signal until approaching the end of the signal. At the end of the signal, the number of averaging data point is reduced in the same manner as was done at the start of the signal.
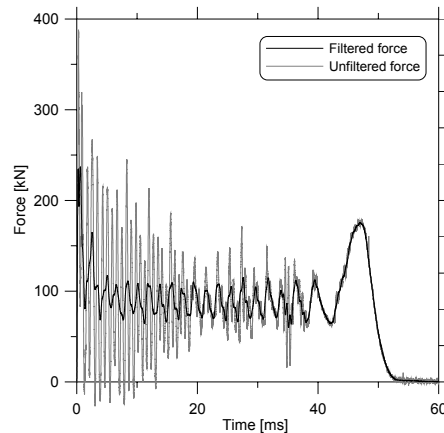
Figure 3-5. Filtering of measured force-time curves.

The running average will reduce the initial peak force and the oscillations in force level, but the absorbed energy will be correctly estimated. No other filtering methods were investigated.

3.3.3   High speed camera

A Phantom v5.0 high-speed monochrome digital video camera was used to record the impact events. The monochrome model offers a higher sensitivity and better image resolution than the colour model. The camera has a maximum frame rate of 64 000 pictures per second and a maximum resolution of 1024x1024 pixels. The frame rate is dependent on the choice of resolution, the higher the resolution the lower the maximum frame rate will be. In the impact tests a resolution of 512x1024 pixels were used, giving a maximum frame rate of approximately 2200 frames per second (Phantom, 2004). When recording at 1,200 pictures per second and higher, image blur can still be a problem with fast moving subjects without the aid of additional shuttering. The Phantom's SR-CMOS sensor allows continuously variable shutter speeds down to 10 micro seconds (1/100 000 second) with intervals of 5 micro seconds (Phantom, 2004). The shutter is a true "snap shot," or synchronous shutter. A standard Nikon AF Zoom-Nikkor lens with focal length 20-35mm was used.

The picture sequence is stored in the camera during filming and transferred to a pc after the test using FireWire data transfer. The camera has 1 gigabyte of image memory. Prior to the test, the camera is set to continuously film using a FIFO (first in first out) memory buffer system. At the chosen frame rate and resolution the camera memory can store 1 second of film. Manual post-triggering was used, i.e. the camera was triggered after the test was completed and all pictures already in the memory were transferred to the computer used to store the films from the experimental tests.

3.3.4   Operation of the pendulum accelerator

The operation of the machine will now be described (Hanssen et al., 2003). Assume that the arm is in its neutral position, a little to the right of the vertical (Pos. 1, Figure 3-1). The arm is connected to the piston rod of a hydraulic/pneumatic actuator that is directly connected to a hydraulic accumulator of the piston type. The volume between the actuator piston and the accumulator piston is filled with hydraulic oil. When preparing for a test, a valve is opened to let pressurised air from the house mains into the piston rod side of the actuator. The arm will move slowly back as the excess oil flows back to the tank of the hydraulic power supply. When the arm has reached its starting position (Pos. 2, Figure 3-1) two hydraulic cylinders, one on each side, will lock the arm by pressing against the locking plate.

The gas (nitrogen) pressure in the accumulator is normally much higher than the air pressure from the house main. Therefore the accumulator piston remains in its lowest position (against the bottom stop) while the arm is moved from Pos. 1 to Pos. 2. After the arm has been locked, a valve is opened so that the volume on the rod side of the actuator is vented to the air. The trolley is now brought up with the thrust roller snug against the arm. Figure 3-3a shows the thrust roller at the rear of the trolley that is in contact with the arm. The machine is then charged by pumping in hydraulic oil under a pressure higher than the final pressure in the accumulator until the accumulator piston reaches its top position (against the top stops). This is indicated by a sudden rise in the oil pressure. The gas (nitrogen) volume in the accumulator has now been reduced by approximately 20 % with a corresponding increase in pressure (the maximum gas volume is about 200 litres, whereas the minimum gas volume is approximately 160 litres). This compressed gas is the energy source for the accelerating system. Hence, it is the initial gas pressure in the accumulator that determines the force that can be produced. The test is now started by releasing the hydraulic cylinders locking the arm and the arm pushes the trolley along its rails. The connection of the actuator piston rod to the arm introduces a 1:5

lever action, i.e. the force acting on the trolley is 1/5 of the piston rod force, but the velocity at the trolley level is 5 times greater. Once the arm has passed the useful part of its arc a sensor applies disc brakes in the arm hubs to stop the arm. After the test, the brakes are released and the arm dropped to its neutral position. Note that the actuator/accumulator assembly has to be able to rotate around an axis trough the end of the actuator, Figure 3-1.

The maximum change in gas volume of the 200-litre gas section of the hydraulic accumulator is 39 litres. The maximum working pressure of the accumulator is 200 bar. A constant pressure of 200 bars expanding by 39 litres yields an energy output of 780 kJ. However, the trolley leaves the arm after about 2/3 the stroke. Hence, the maximum energy delivered to the trolley is approximately 500 kJ. For a trolley weighing 600 kg this indicates a maximum speed of 40 m/s.

4 Experimental results

4.1 Quasi-static tests

In this chapter quasi-static and dynamic tests on axially loaded thin-walled aluminium extrusions are presented. Four different thicknesses and a high number of different lengths were tested. The purpose of these tests is to provide load displacement data for axial loading of thin-walled aluminium extrusions collapsing in different modes. The experimental data will be used to validate the finite element model.

4.1 Quasi-static tests

The results from the quasi-static tests are presented in Table 4-1. The mean force P_m is calculated as the absorbed energy divided by the total deformation of the extruded member, δ, where the absorbed energy is equal to the area under the force-displacement curve. In order to compare the energy absorption of members with the same cross-section, but different collapse modes, P_m^* is calculated as the energy absorbed until the time of transition divided by the displacement corresponding to bottoming out. The displacement at bottoming out was chosen as 0.73L (Jones, 1989) where L is the free length of the member. The displacement w_T at the time of transition was taken when a sudden drop in the force-displacement curve occurred. Thus, for members collapsing in progressive buckling mode, $P_m^* = P_m$. As a reference P_m^* for members collapsing in global buckling is also presented. Here w_T is chosen as 40 mm which is beyond the maximum load. Force-deformation curves and pictures from all tests are presented in Appendix B.

Table 4-1 Results from the quasi-static tests.

Test #	L	h	δ	w_T	P_{max}	P_m	P_m^*	Mode[1]
	(mm)	(mm)	(mm)	(mm)	(kN)	(kN)	(kN)	
S1	1280	4.5	76	40	267	99	6	G
S2	1278	3.5	138	40	207	39	4	G
S3	959	2.5	718	-	136	49	-	P
S4	959	2.0	725	-	91	32	-	P
S5	799	4.5	236	40	267	60	11	G
S6	802	3.5	595	-	216	87	-	P
S7	799	2.5	605	-	111	50	-	P
S8	639	4.5	244	40	284	75	15	G
S9	638	2.5	446	-	148	50	-	P
S10	800	2.0	335	250	100	25	12	T
S11	800	2.5	610	-	146	50	-	P
S12	720	2.0	539	-	94	30	-	P
S13	639	3.5	456	-	218	85	-	P
S14	638	2.0	455	-	99	35	-	P
S15	1280	2.0	477	250	102	23	8	T
S16	1280	2.5	974	-	147	49	-	P
S17	1120	2.0	900	-	96	34	-	P
S18	879	3.5	633	-	201	80	-	P
S19	560	4.5	375	-	286	142	-	P
S20	1120	2.5	860	-	136	50	-	P
S21	1200	2.0	962	-	93	33	-	P
S22	1360	2.0	1081	-	88	32	-	P
S23	1438	2.5	492	360	143	43	18	T
S24	1360	2.5	982	-	146	50	-	P
S25	1520	2.0	1222	-	100	35	-	P
S26	560	4.5	375	-	290	146	-	P
S27	480	4.5	251	40	292	81	21	G
S28	454	4.5	223	40	288	100	22	G
S29	454	4.5	249	-	301	147	-	P
S30	1040	3.5	741	-	174	76	-	P
S31	959	3.5	702	-	207	84	-	P
S32	1679	2.0	493	250	82	25	7	T
S33	1839	2.0	634	550	93	31	14	T
S34	1200	3.5	398	310	177	71	28	T
S35	1120	3.5	496	300	185	66	30	T
S36	1520	2.5	973	-	151	51	-	P
S37	1760	2.5	970	-	149	49	-	P
S38	1680	2.5	740	-	143	47	-	P
S39	400	4.5	211	-	291	146	-	P
S40	1919	2.0	233	90	91	26	2	T
S41	1919	2.5	232	140	140	43	5	T
S42	1840	2.5	726	-	145	49	-	P

[1] G = global buckling, P = progressive buckling and T = transition.

Three different deformation modes were observed in the quasi-static tests, when varying the length and wall thickness of the specimens. In the case of progressive buckling, see Figure 4-1a, the deformation starts with plate buckling in the extrusion walls. The position of the first lobe along the length of the member appeared to be random for all thicknesses. For all four thicknesses an axisymmetric collapse mode was observed. The axisymmetric collapse mode is here defined as the mode where two opposing extrusion walls move inwards and the other two move outwards. As seen in Figure 4-1b, an initial peak related to the initiation of the first buckle is always observed in the force-displacement curve, followed by oscillations around a mean force level.

Direct global buckling, or Euler buckling, was observed for some of the specimens when the length of the specimen was increased, see Figure 4-2a. This response was only observed for the more thick-walled members with wall thickness of 3.5 and 4.5 mm. This collapse mode is characterized by large lateral displacements. As observed by Abramowicz and Jones (1997), the large lateral displacements induced localized sectional collapse of the mid and end sections of the extruded member.

a) Deformation mode   b) Force-deformation curve
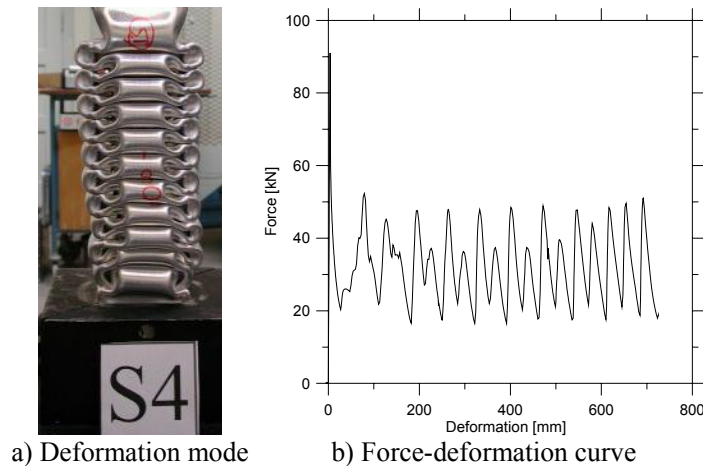
Figure 4-1 Quasi-static test #S4 (see Table 4-1). Progressive buckling.

a) Deformation mode   b) Force-deformation curve
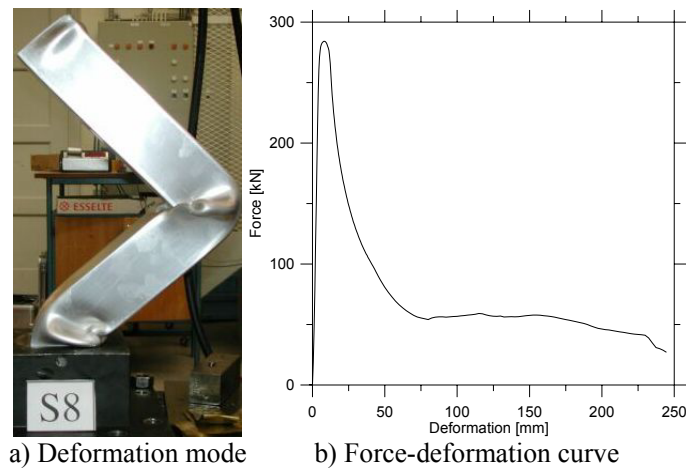
Figure 4-2 Quasi-static test #S8 (see Table 4-1). Global buckling,

The initial peak in the force-displacement curve is followed by a drop to a low and relatively constant force level, see Figure 4-2b.

The members with wall thicknesses of 2.0 mm, 2.5 mm and 3.5 mm experienced a transition from progressive to global buckling when the length of the test specimen was increased, see Figure 4-3a. The deformation started as in the case with progressive buckling. However, it was observed that the lobes started to develop eccentrically. This eccentricity continued to grow in many cases and after some deformation a transition from progressive to global buckling with large lateral displacements occurred. The initial peak force was followed by oscillations in the force level as in the case of a progressive buckling mode, but as can be seen from Figure 4-3b, there is a significant drop in force level when the transition to the global failure mode occurs.

A relatively large variation in initial peak force was observed for members with identical cross-sectional area collapsing in the same collapse mode, see Figure 4-4a. For the members with a wall thickness of 2.5 mm collapsing in progressive

a) Deformation mode   b) Force-deformation curve
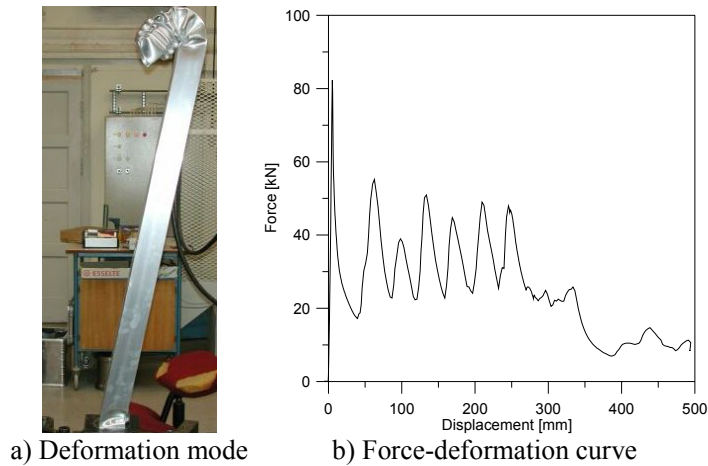
Figure 4-3 Quasi-static test #S32 (see Table 4-1). Transition from progressive to global buckling.

buckling the variation in peak force was as large as 36 %. The variation in peak force was somewhat smaller for the other thicknesses. It was observed that the members collapsing in a direct global mode experienced a somewhat smaller peak force than the members collapsing in progressive buckling or in transition from progressive to global buckling. No relationship was found between the measured peak force and the location of the first lobe. As can be seen from Figure 4-4b the maximum stress is close to the yield stress, $\sigma_{0.2}$, for the members with wall thickness 2.5 mm, 3.5 mm and 4.5 mm. Søvik Opheim (1996) did bending tests on thin-walled aluminium extrusions and found that the peak load was very sensitive to variations in the material curve parameters and to σ_0 in particular. Thus variation of buckling stress for axial loaded extrusions should be expected when buckling occurs early in the plastic region.

Figure 4-5 shows the deformation modes as a function of the global slenderness (L/b) and local slenderness (b/h) of the members. As can be seen, the members with a nominal wall thickness of 4.5 mm (b/h = 18.2) experienced only progressive or global buckling. The members with a wall thickness of 3.5 mm (b/h = 23.9)

a) Peak force   b) Maximum stress.
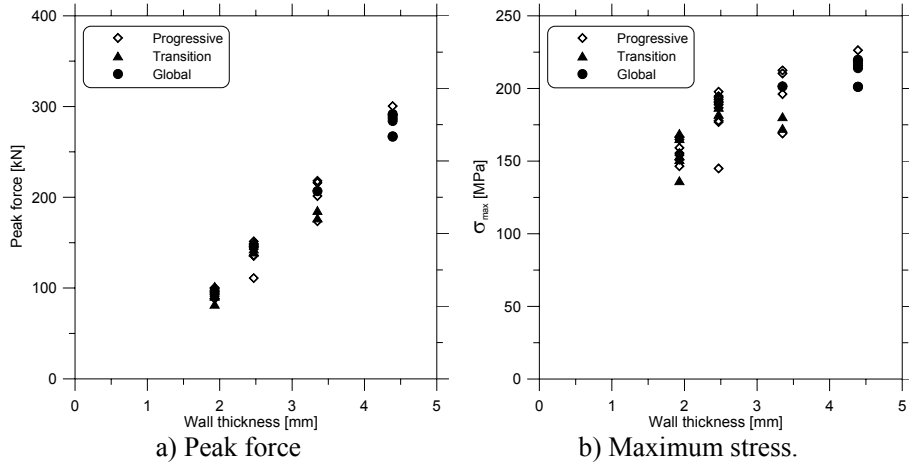
Figure 4-4 Quasi-static tests.
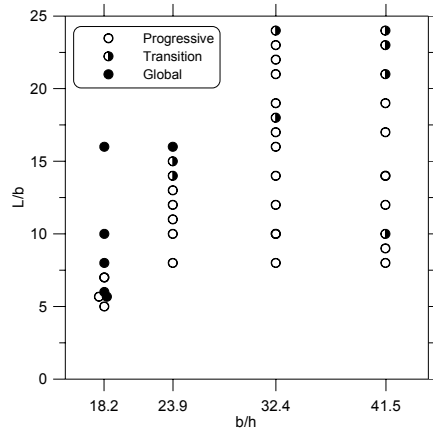
Figure 4-5 Collapse modes in quasi-static tests.

collapsed in either progressive buckling, direct global buckling or in a transition from progressive to global buckling. The more thin-walled members with a wall thickness of 2.5 mm (b/h = 32.4) or 2.0 mm (b/h = 41.5) collapsed in either progressive buckling or in a transition from progressive to global buckling. The critical global slenderness is defined as the slenderness where direct global buckling or a transition from progressive to global buckling occurs. The critical global slenderness appears to be rising for increasing local slenderness. This is

consistent with the results found by Abramowicz and Jones (1997). As can be seen from Figure 4-5, however, there are some anomalous results. When increasing the global slenderness for a given local slenderness, the response can change from a progressive to a global mode and back again to a progressive mode. Sometimes for a given combination of local and global slenderness, progressive buckling occurred in one parallel test while in the next test global buckling occurred. Hsu and Jones (2004) also reported an unexpected scatter in the tests on circular tubes made of aluminium alloy 6063-T6.

4.2 Dynamic tests

The results from dynamic tests with initial impact velocity of 13 m/s and 20 m/s are presented in Table 4-2 and Table 4-3 respectively. The mean force presented in Table 4-2 and Table 4-3 is calculated based on the absorbed energy at a deformation equal to d_b which is the deformation at the time the impacting mass hits the buffer system. P_m^* is calculated as in the quasi-static tests. Force-deformation curves from all dynamic tests are presented in Appendix C and Appendix D respectively.

As can be seen from Table 4-2 and Table 4-3 the accuracy parameter Δ_b is within the range of 0.96-1.06, indicating a very good accuracy of the recorded force. In some of the tests, the test specimen had large lateral displacements and hit the buffer system before the impacting mass hit the buffer system. In these cases the accuracy parameter Δ_b has not been calculated.

The same deformation modes were observed in the dynamic tests as in the quasi-static tests. A sequence of photos showing progressive buckling is shown in Figure 4-6 together with the corresponding force-time curve. The dots in the force-time curve represent the different deformation stages shown in the photos. The dominating local collapse mode was axisymmetric, which was observed for all four

Table 4-2 Results from impact tests, $V_0 = 13$ m/s.

Test #	L (mm)	h (mm)	l_b (mm)	d_b (mm)	w_T (mm)	Δ_b (-)	P_m (kN)	P_m^* (kN)	Mode[1]
D1-1	1598	2.5	939	951	800	1.01	51	39	T
D1-2	1360	2.5	751	751	425	1.00	57	25	T
D1-3	1597	2.0	940	934	770	0.99	33	24	T
D1-4	1598	4.5	942	309	40	-	99	17	G
D1-5	1359	2.0	873	848	-	0.97	38	-	P
D1-6	1598	3.5	1015	904	900	-	98	75	T
D1-7	1358	3.5	732	705	-	0.96	96	-	P
D1-8	1199	4.5	684	393	40	-	86	22	G
D1-9	799	4.5	426	-	-	-	-	-	P
D1-10	1201	3.5	693	680	-	0.98	94	-	P
D1-11	798	3.5	370	357	-	0.97	104	-	P
D1-12	1198	2.0	685	676	-	0.99	37	-	P
D1-13	1361	4.5	979	462	40	-	85	19	G
D1-14	1040	4.5	507	-	-	-	-	-	P
D1-15	959	4.5	407	-	-	-	-	-	G
D1-16	1380	3.5	850	-	-	-	-	-	P
D1-17	958	2.5	490	-	-	-	-	-	P
D1-18	1120	3.5	690	666	-	0.97	95	-	P
D1-19	880	3.5	440	434	-	0.99	91	-	P
D1-20	1437	2.0	904	898	-	0.99	39	-	P
D1-21	1197	2.5	745	736	-	0.99	56	-	P
D1-22	1440	3.5	925	903	-	0.98	86	-	P
D1-23	1280	2.5	800	787	-	0.98	56	-	P
D1-24	1120	2.5	696	689	-	0.99	57	-	P
D1-25	1520	2.0	990	982	680	0.99	31	24	T
D1-26	1118	4.5	670	290	220	-	151	50	T
D1-27	958	4.5	527	515	-	0.98	159	-	P
D1-28	878	4.5	490	221	40	-	90	22	G
D1-29	1280	2.0	745	-	-	-	-	-	P
D1-30	680	4.5	260	-	-	-	-	-	P

[1] G = global buckling, P = progressive buckling and T = transition.

Table 4-3 Results from impacts tests, V_0 = 20 m/s.

Test #	L (mm)	h (mm)	l_b (mm)	d_b (mm)	Δ_b (-)	w_T (mm)	P_m (kN)	P_m^* (kN)	Mode[1]
D2-1	640	4.5	355	343	0.97	-	172	-	P
D2-2	639	3.5	355	345	0.97	-	102	-	P
D2-3	639	4.5	355	352	0.99	-	167	-	P
D2-4	639	2.5	380	368	0.97	-	58	-	P
D2-5	800	3.5	441	431	0.98	-	97	-	P
D2-6	638	2.0	322	316	0.98	-	41	-	P
D2-7	800	4.5	442	430	0.97	-	161	-	P
D2-8	799	2.5	462	453	0.98	-	57	-	P
D2-9	800	2.0	536	530	0.99	530	42	38	T
D2-10	959	4.5	541	546	1.01	-	151	-	P
D2-11	960	3.5	588	588	1.00	-	95	-	P
D2-12[2]	820	2.0	-	-	-	-	-	-	-
D2-13	1119	4.5	707	703	0.99	-	148	-	P
D2-14	1120	3.5	725	724	1.00	-	91	-	P
D2-15	1117	2.5	708	706	1.00	-	56	-	P
D2-16	879	2.0	469	465	0.99	-	36	-	P
D2-17	1440	3.5	805	794	0.99	-	92	-	P
D2-18	1437	4.5	790	834	1.06	-	146	-	P
D2-19	1438	2.5	860	480	-	410	59	25	T
D2-20	1280	2.5	620	614	0.99	-	53	-	P
D2-21	1119	2.0	580	572	0.99	-	36	-	P
D2-22	1600	3.5	940	928	0.99	600	66	46	T
D2-23	1602	4.5	818	848	1.04	-	142	-	P
D2-24	1761	4.5	800	788	0.99	-	155	-	P
D2-25	1440	2.0	868	848	0.98	-	42	-	P
D2-26	799	2.0	364	375	1.03	-	38	-	P
D2-27	1359	2.5	700	684	0.98	850	56	39	T
D2-28	1519	3.5	980	976	1.00	-	88	-	P
D2-29	1840	4.5	805	854	1.06	-	143	-	P
D2-30	1920	4.5	1443	415	-	300	153	41	T
D2-31	1760	3.5	1100	1088	0.99	-	89	-	P
D2-32	1839	3.5	1199	1169	0.97	1140	93	79	T
D2-33	1919	3.5	1289	1251	0.97	900	72	61	T
D2-34	1438	2.0	840	822	0.98	570	31	23	T
D2-35	1520	2.0	-	-	-	-	-	-	T
D2-36	1279	2.0	876	535	-	440	35	18	T

[1] G = global buckling, P = progressive buckling and T = transition.
[2] Specimen was not tested.

thicknesses. However, some of the test specimens sometimes experienced a pure extensional mode where all four extrusion walls moved first outwards and then inwards. The formation of these lobes was only observed when the deformation started at the clamped end. However, after the formation of the first few lobes the mode of deformation changed to an axisymmetric mode. With an impact velocity of 13 m/s, the extensional mode was only observed for some of the 3.5 mm and 4.5 mm thick specimens. At 20 m/s the extensional mode was found for all thicknesses. For the members with a wall thickness of 4.5 mm a higher number of pure extensional lobes was observed than for the specimens with smaller wall thickness.

At 13 m/s the first lobes were always initiated at the clamped end for members with wall thicknesses 2.0 mm, 2.5 mm and 3.5 mm. For the members with a wall thickness of 4.5 mm the location of the first lobes was more random. In four of the tests the deformation started at the impacted end, while in two tests it started at the clamped end. At 20 m/s the formation of the first lobes was more or less random for the members with wall thicknesses 2.5 mm and 4.5 mm. In seven of the tests of specimens with a wall thickness of 2.0 mm the deformation started at the impacted end and only once at the clamped end. For nine of the tests with a wall thickness of 3.5 mm the deformation started at the clamped end and only once at the impacted end.

In the case of progressive buckling, an initial peak is always observed, see Figure 4-6b. The initial peak is followed by oscillations around a mean force level. When the extrusion is compressed to approximately 70 % of the initial length, it is not possible to form new lobes, the lobes will be compressed and the force level will increase rapidly.

| t = 1.02 ms | t = 7.17 ms | t = 19.99 ms | t = 30.24 ms | t = 41.00 ms |

a) Typical stages of deformation.

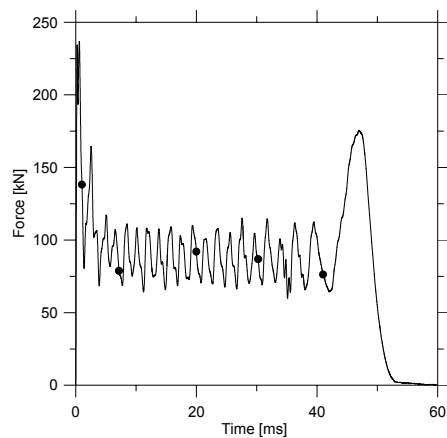
b) Typical force vs. time history.
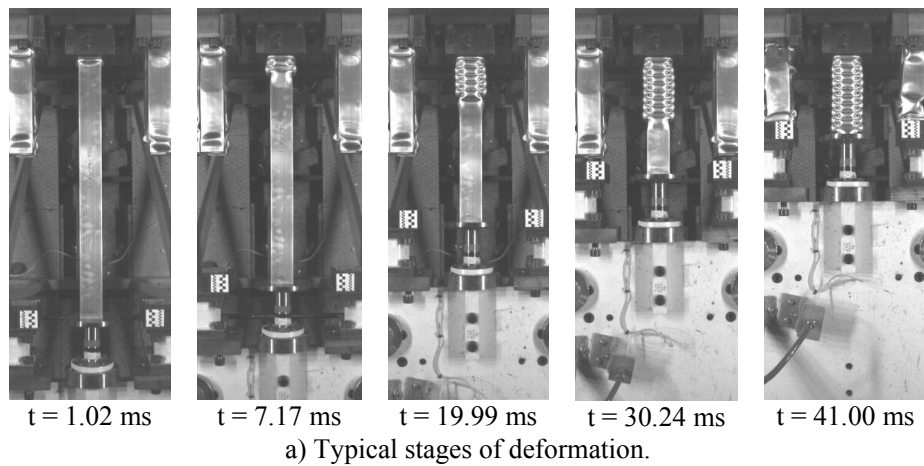
Figure 4-6. Impact test #D2-11 (see Table 4-3). Progressive buckling.

In the impact tests at 13 m/s direct global buckling was observed for some of the specimens with a wall thickness of 4.5 mm, see Figure 4-7a. We see the same characteristic peak force followed by a drop in force as in the quasi-static case, see Figure 4-7b.

| t = 1.65 ms | t = 2.20 ms | t = 3.30 ms | t = 8.80 ms | t = 18.16 ms |

a) Typical stages of deformation.
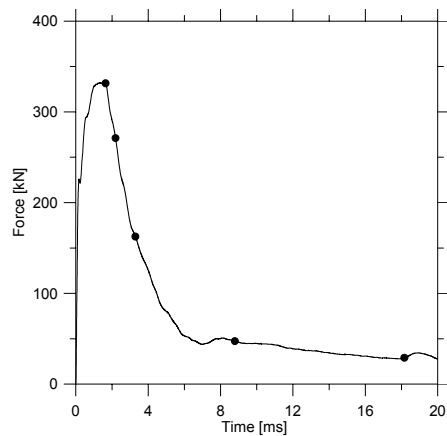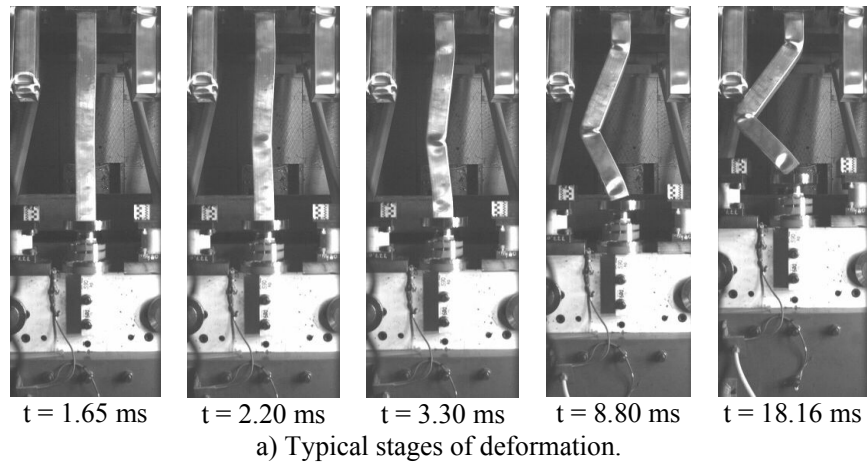
b) Typical force vs. time history.

Figure 4-7. Impact test #D1-28 (seeTable 4-2). Global buckling,

At 13 m/s and 20 m/s a transition from progressive to global buckling was observed for all thicknesses when the length of the members was increased, see Figure 4-8a. The deformation follows the same course as in the quasi-static tests, an initial peak followed by oscillations around a mean force level and a sudden drop in force level when the transition occurs, see Figure 4-8b. It was observed that

the transition occurred at a later stage of the deformation than in the quasi-static tests.

In the dynamic tests with impact velocity of 13 m/s, the members with a wall thickness of 4.5 mm (b/h = 18-2) collapsed in progressive buckling, direct global buckling or in a transition from progressive to global buckling, see Figure 4-9a.

t = 1.55 ms   t = 12.97 ms   t = 33.73 ms   t = 38.92 ms   t = 56.57 ms
a) Typical stages of deformation.

b) Typical force vs. time history.

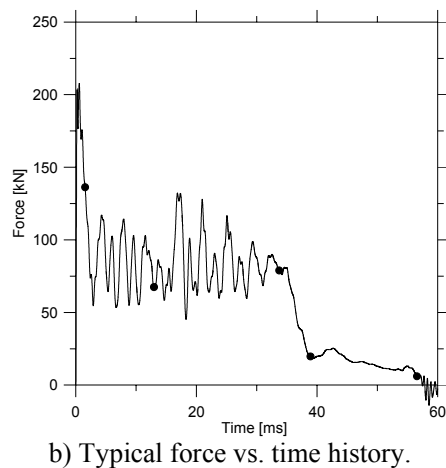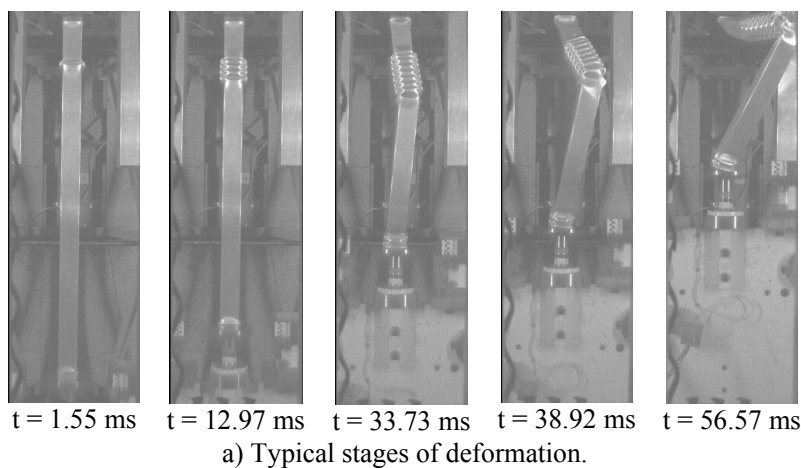*Figure 4-8. Impact test #D2-22 (seeTable 4-3). Transition from progressive to global buckling.*

a) v_0 = 13 m/s   b) v_0 = 20 m/s
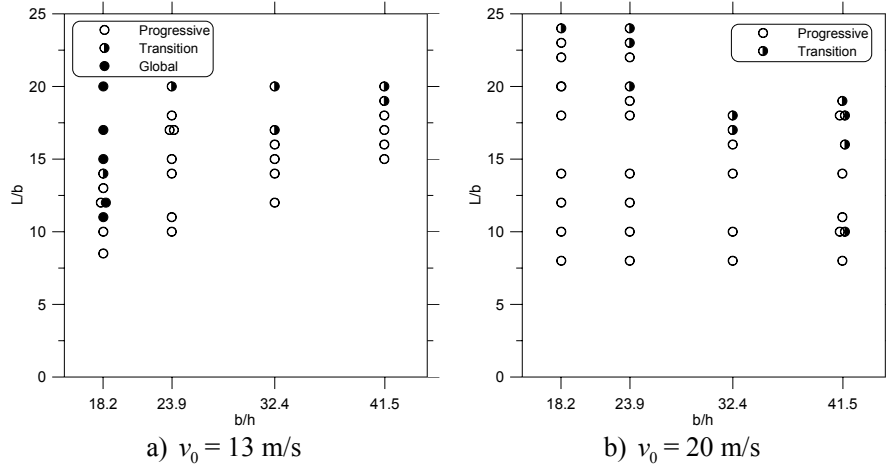
Figure 4-9 Collapse modes in impact tests.

The members with a wall thickness of 3.5 mm (b/h = 23.9), 2.5 mm (b/h = 32.4) or 2.0 mm (b/h = 41.5) collapsed in either progressive buckling or in a transition from progressive to global buckling. As can be seen from Figure 4-9b, only progressive buckling and a transition from progressive to global buckling were observed when the impact velocity was increased to 20 m/s.

The tests with impact velocity of 13 m/s showed an increase in critical global slenderness when reducing the wall thickness from 4.5 mm to 3.5 mm, but a further reduction in wall thickness did not lead to a continued increase in critical global slenderness. The members with a wall thickness of 3.5 mm and 4.5 mm experienced an increase in critical global slenderness compared to the quasi-static tests, see Figure 4-5 and Figure 4-9a. This is probably due to inertia forces preventing direct global bending and the transition from progressive to global buckling for the members with wall thicknesses of 3.5 mm and 4.5 mm. In contrast, the more thin-walled members with a wall thickness of 2.0 mm and 2.5 mm experienced a decrease in critical global slenderness compared to the quasi-static tests. It was observed that the members with a wall thickness of 2.0 mm and 2.5 mm had a tendency to develop lobes at several places along the length of the

member simultaneously, thus making the member more unstable and increasing the probability of a transition from progressive to global buckling. At 20 m/s the critical global slenderness was further increased for members with wall thicknesses 3.5 mm and 4.5 mm, and further reduced for members with wall thicknesses 2.0 mm and 2.5 mm; giving decreasing critical global slenderness as a function of the local slenderness, see Figure 4-9b. This dramatic change in response compared to the quasi-static tests can be critical if the design of components subjected to dynamic axial loading is based on quasi-static or low velocity impact behaviour.

As in the quasi-static tests, there are some anomalous results, see Figure 4-9. When increasing the global slenderness for a given local slenderness, the response will change between progressive and global buckling or between progressive buckling and a transition from progressive to global buckling. Two different collapse modes were observed for members with the same local and global slenderness.

4.3   Summary

The results from both quasi-static and impact tests are summarized in Figure 4-10. The solid line separates, approximately, the regions with progressive buckling, and direct global buckling or transition from progressive to global buckling.

Combinations of local and global slenderness ratios below the line will give progressive buckling, if the impact velocity does not exceed 20 m/s. Slenderness ratios above the line will give either a transition from progressive to global buckling mode or a direct global buckling mode, depending on impact velocity and slenderness ratios. From Figure 4-10 it can be concluded that the extrusions with nominal wall thickness 2.5 mm (global slenderness 32.4) has the highest critical global slenderness when the impact velocity is kept below 20 m/s. The extrusions with wall thickness 4.5 mm has the lowest critical global slenderness in the quasi-static tests, and the highest in the impact tests with impact velocity 20 m/s.
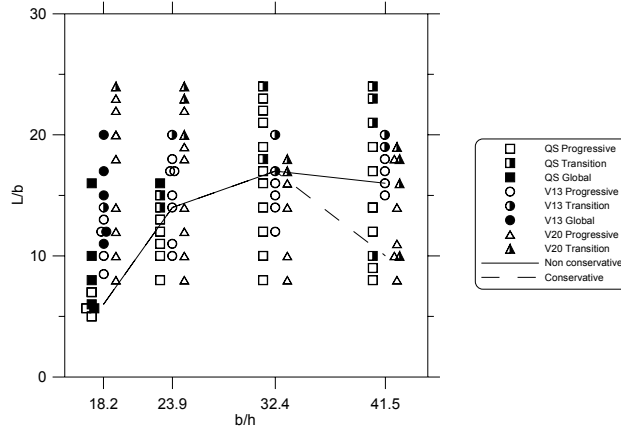
Figure 4-10 Collapse modes in experimental tests.

Abramowicz and Jones (1997) performed quasi-static and dynamic tests on simply supported square and circular tubes made of six different types of mild steel. In the quasi-static tests on square tubes, they found the following expression to separate the progressive buckling and global bending regions

$$\left(\frac{L}{b}\right)_{cr} = 2.482 \exp\left(0.0409\frac{b}{h}\right)$$ (4-1)

In Figure 4-11 the experimental results from the present quasi-static tests are presented together with the empirical expression given by Abramowicz and Jones (1997).

As can be seen from Figure 4-11, the aluminium extrusions in the present study, except the most thick-walled tubes, have a significantly higher critical global slenderness than the mild steel tubes examined by Abramowicz and Jones (1997). Thus, for a given cross-section a longer tube can be used, and if the characteristic stress is the same, more energy can be absorbed.
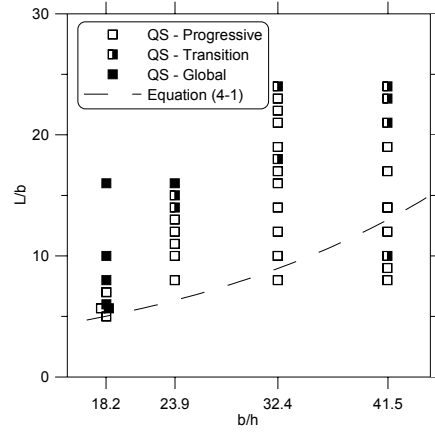
Figure 4-11 Quasi-static tests.

Abramowicz and Jones (1997) also performed dynamic tests on the same types of mild steel tubes at different impact velocities. The tubes were impacted at velocities up to 12.14 m/s. They found that the following expressions separated, approximately, the regions with global bending, transition mode and progressive buckling.

$$\left(\frac{L}{b}\right)_{cr} = 2.453\exp\left(0.08\frac{b}{h}\right) \qquad (4\text{-}2)$$

$$\left(\frac{L}{b}\right)_{cr} = 3.423\exp\left(0.04\frac{b}{h}\right) \qquad (4\text{-}3)$$

Equation (4-2) and Equation (4-3) gives, respectively, the critical global slenderness where direct global buckling and a transition mode will occur. In Figure 4-12 the collapse modes found in the experimental tests at 13 m/s is compared with the empirical expressions given by Abramowicz and Jones (1997).
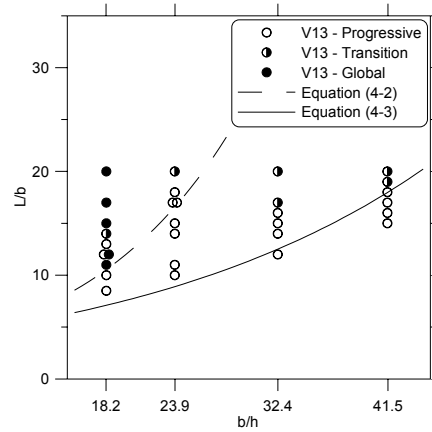
Figure 4-12 Dynamic tests.

The aluminium extrusions with wall-thickness 4.5 mm experienced direct global buckling at approximately the same global slenderness as the steel tubes studied by Abramowicz and Jones (1997). The transition mode occurs at a higher global slenderness ratio in the aluminium extrusion with wall thickness 2.5 mm, 3.5 mm and 4.5 mm than in the steel tubes with the same local slenderness. Aluminium extrusions with wall thickness 2.0 mm experience the transition from progressive to global buckling at approximately the same global slenderness as steel tubes with the same local slenderness.

In general it appears that the aluminium extrusions in the present study collapsed progressively for higher slenderness ratios than the steel tubes examined by Abramowicz and Jones (1997). This may be due to different boundary conditions and/or initial imperfections.

5 Numerical simulations

The main objective of this chapter is to investigate the ability of the finite element code LS-DYNA (Hallquist, 1998) to predict the response of axially loaded thin-walled aluminium extrusions. The main focus is placed on predicting the correct folding and collapse mode, the correct mean force level and for the implicit simulations also the peak force.

A baseline model was established and the numerical simulations were compared with the experimental results presented in Chapter 4. The explicit version of LS-DYNA was used for the simulation of the impact tests. Both explicit and implicit versions of the code were used in the simulations of the quasi-static tests. The advantage of using the implicit version for the quasi-static tests is that stress waves and inertia effects are not present in implicit simulations. Unless otherwise specified, the default parameters of LS-DYNA have been used in the numerical model. The influence from some key parameters on the mean force level has been investigated.

A parametric study has been carried out using the baseline model. The influence from impact velocity and material properties on the collapse mode and mean force level has been studied. Finally, means to stabilize the response and thus increasing the critical global slenderness by introducing triggers have been investigated.

5.1 Finite element model

In the experimental tests a symmetric deformation mode was generally observed, implying use of symmetry. Both extensional and axisymmetric modes of deformation can be considered as symmetric with respect to modelling of the geometry. However, preliminary simulations showed that use of symmetry in some

cases prevented transition from progressive folding to global buckling, thus a full model should be used when studying the transition from progressive to global buckling of thin-walled aluminium extrusions. Consideration was given to make the numerical model as simple and CPU efficient as possible without sacrificing the validity of the simulations compared to the experimental tests.

In order to give an accurate description of both small and large strains, a multi-exponent strain hardening rule was used, see Equation (2-4), i.e. LS-DYNA material model 103 (Hallquist, 2003). For simplicity isotropic elasticity, the von Mises yield criterion, the associated flow rule and isotropic hardening were used. The yield criterion of extruded aluminium has a shape in the $\sigma_{xx} - \sigma_{yy}$ space which is somewhere between the von Mises and the Tresca criterion. Lademo (1999) found the Yld96 criterion proposed by Barlat best suited to describe the behaviour of extruded aluminium profiles. However, this yield criterion is very CPU time consuming compared to the von Mises criterion. Preliminary simulations have shown that the choice of yield criterion has small influence on the mean force level, thus it was chosen to use the von Mises yield criterion in the simulations.

The clamping device used in the experimental test, see Figure 3-3, was not modelled in the numerical model, instead the clamped part of the extruded member was modelled with all rotational and lateral degrees of freedom fixed to account for the boundary conditions imposed by the clamping device. The axial degree of freedom was free in the clamped part allowing for stress wave propagation and stress wave reflection in this part. The bottom row of nodes was fixed in all degrees of freedom to fix the member in space. The upper end was unrestrained.

During axial crushing of an extruded member, the sidewalls will bend and lobes will form. As the axial deformation increases the lobes will come in contact with each other. To account for this contact the automatic single surface contact algorithm in LS-DYNA (Hallquist, 2003) with no friction was used.

The imperfections of the extruded member were observed to be small. Both local and global initial imperfections were modelled. For the global imperfections a half sine wave with amplitude δ_g equal to L/2000, L being the length of the specimen, was used. For the local imperfections a half sine wave across the width of the profile and uniform in the extrusion direction were used, see Figure 5-1c. The amplitude of the local imperfections was δ_l = b/200. The chosen imperfection amplitudes are based on tolerances given by the extrusion producer for an industrial bar. Be aware that in the figure the amplitude is greatly magnified to show the shape of the imperfections. The chosen local imperfections will trigger the correct folding mode, but since the local imperfections are uniform along the length of the specimen the location of the first lobe will not be dictated by the choice of local imperfections. In some of the experimental tests the formation of one or two extensional lobes was observed when the deformation started in the clamped end. The formation of extensional lobes at the clamped end was not prevented by the chosen local imperfection shape.

Shell elements were used due to CPU efficiency. It was chosen to use quadratic element geometry. As earlier mentioned it was chosen to use the default values of LS-DYNA wherever possible and the default shell elements (type 2) was used. However, in order to get the correct folding mode, the option for "membrane strain causing thickness change" had to be used. If not using this option an extensional

a) Explicit model b) Implicit model c) Cross-section with imperfections
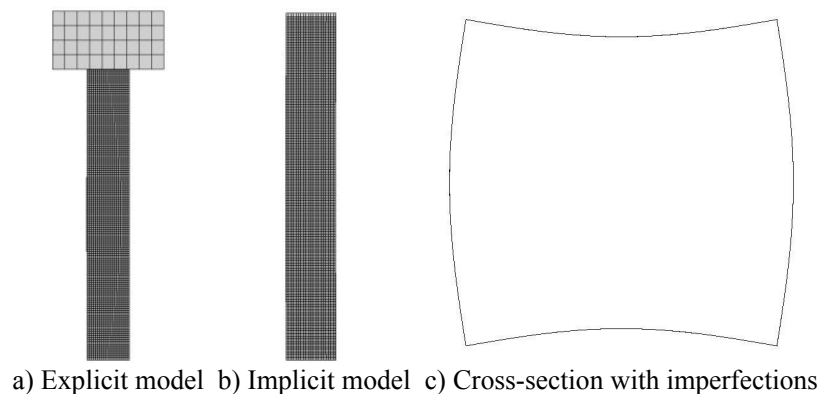
Figure 5-1 Geometry numerical model.

deformation mode was found instead of the axisymmetric mode that was the dominant mode in the experiments. In addition seven integration points through the thickness was used. The default of two integration points through the thickness should only be used if the elements are behaving elastically. In a buckling analysis the bending of the element during folding will give rise to a highly non-linear stress distribution over the thickness of the element. Several simulations were carried out to determine the sufficient number of elements. A 640 mm long specimen with wall thickness 2.5 mm and impacted at 20 m/s was modelled with an increasing number of elements over the width, and the deformation mode was compared to the one observed in the experimental tests, see Figure 5-2.

| 6 elements | 8 elements | 10 elements | 12 elements | 16 elements |

| 18 elements | 20 elements | 26 elements | 30 elements | Component test |
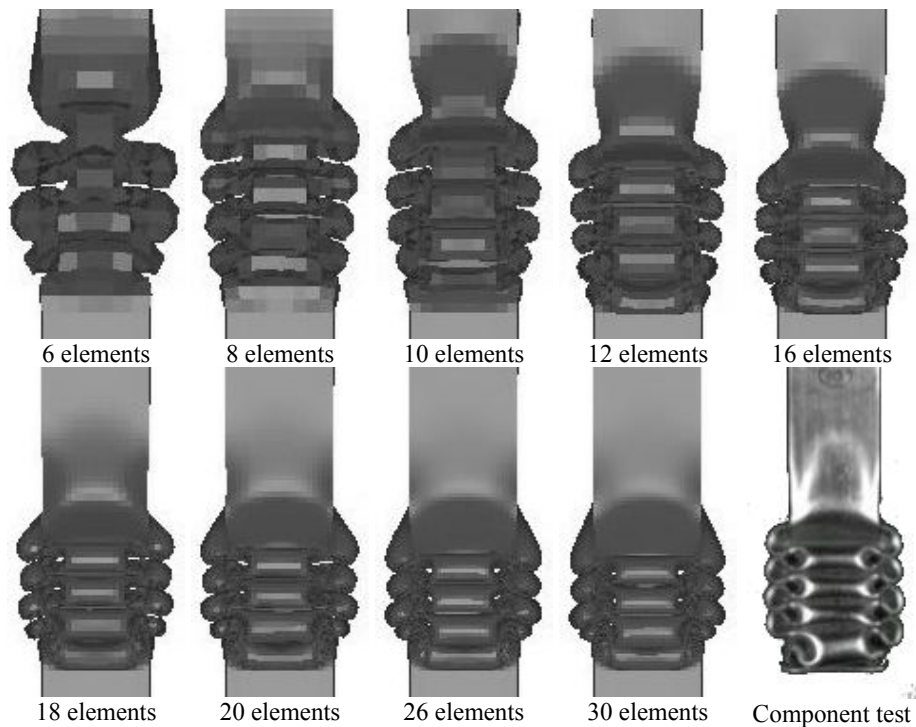
Figure 5-2 Folding shape vs. # elements.

The deformation started at the clamped end in all the simulations and in the experimental test, see Figure 5-2. In the experimental test an average lobe length of 50 mm was found. The coarsest mesh with 6 elements over the width gave an average lobe length of 58 mm. The other meshes gave an average lobe length of 46 mm.

In the experimental test the first lobe was an extensional lobe followed by axi-symmetric lobes. At 20 m/s this was observed for all thicknesses when the deformation started at the clamped end. In the simulations only axi-symmetric lobes were observed. However, for higher thicknesses, 3.5 mm and 4.5 mm, this change from extensional mode to axi-symmetric mode was also observed in the numerical simulations.

The mean force vs. deformation is presented in Figure 5-3. The mean force of the model is directly related to the number of elements used. If the model is too coarse the mean force will be too high. The mean force appears to converge for 20 elements or more.

# Elements	Mean force [kN]	Deformation [mm]
6	61.58	299
8	55.58	301
10	51.78	302
12	50.79	302
16	48.48	303
18	46.64	304
20	45.95	304
26	44.79	304
30	44.45	304
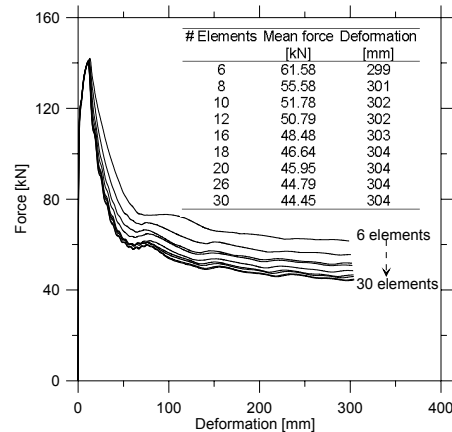
Figure 5-3 Mean force level vs. # elements.

In the experimental test the local deformation mode was the same for all thicknesses. Thus, it was assumed that the required number of elements over the width was the same for all thicknesses. The local collapse in the extrusion walls during global buckling is similar to the folding mechanism found in the progressive buckling mode. Accordingly it was assumed that if the model was capable of describing the progressive collapse mode it would be good enough for the global mode as well.

Based on the folding shape and mean force level it was concluded that 20 elements over the width would give a relatively good description of the folding mechanism. This will give an element size of approximately 4 mm.

In the simulations the average thickness and width specified in Section 3.1 was used and not the nominal thickness.

The simulations were run on a SGI Origin 3800L with 512 CPUs and 512 GB total memory, except the mesh sensitivity simulations and the simulations in Chapter 6.3.2.2 which were run on a Linux cluster.

5.1.1   Explicit simulations

In the explicit simulations the specimens were modelled using Belytschko-Tsai shell elements with seven integration points through the thickness and one point in the plane. To reduce CPU costs the impacting mass was modelled as a rigid body using brick elements, see Figure 5-1a. The contact between the impacting mass and the specimen was modelled using automatic nodes to surface (Hallquist, 2003) with a friction coefficient of 1.0 to avoid unrealistic lateral movement of the upper end of the specimen.

The explicit simulations were run using LS-DYNA version 970. The mpp (massive parallel processing) version with 16 CPUs was used. Some preliminary simulations

were run to check the correlation between results from the single CPU and the mpp version of LS-DYNA. No difference in deformation mode was found and the difference in force level was negligible. In addition a number of simulations were run to check the CPU efficiency for different number of CPUs. When increasing the number of CPUs used in a mpp simulation, the simulation run time will in general decrease but the total cost (#CPUs times simulation time) will increase. It was concluded that 16 CPUs gave a relatively good mix of reduction in simulation time and efficient use of the CPUs.

5.1.2   Implicit simulations

Element type 16 with seven integration points through the thickness was used in the implicit simulations. The contact between the impacting mass and the test specimens created numerical problems in the implicit simulations. Thus an alternative way of applying the deformation had to be adopted. To deform the specimen a set of rigid elements were attached to the upper part and given a constant velocity in the negative z-direction, see Figure 5-1b. The rigid body was constrained from rotation and lateral displacement. The implicit simulations were run in LS-DYNA version 970. As it is not feasible to use the mpp version in implicit simulations, the smp (shared memory parallel) version was used. The CPU efficiency per CPU when increasing the number of CPUs is decreasing at a higher rate in the smp version. The preliminary simulations showed that using 4 CPUs gave the most efficient use of the CPUs.

5.2   Validation of numerical simulations

5.2.1   Quasi-static analysis

In the quasi-static component tests different collapse modes were observed for the different thicknesses when the length was increased. Members with wall thickness 2.0 mm and 2.5 mm collapsed in either progressive buckling or in a transition from

progressive to global buckling. When the wall thickness was increased to 3.5 mm the members collapsed in either progressive buckling, global buckling or in a transition from progressive to global buckling. However, members with wall thickness 4.5 mm collapsed in either progressive or global buckling. Thus it is important that the simulations are able to describe the different collapse modes correctly.

5.2.1.1 Implicit simulations

Numerical instabilities caused the simulations of the members with nominal wall thickness 2.0 mm, 2.5 mm and all except two of the members with wall thickness 3.5 mm to end prematurely. The numerical instabilities occurred at a very early stage and it is not possible to say if the implicit simulations are capable of describing the transition from progressive folding to a global buckling mode that was found in the experimental tests for members with nominal wall thickness 2.0 mm, 2.5 mm and 3.5 mm.

The results from the simulations are presented in Table 5-1. The mean force for the simulations is calculated at the deformation level given in the third column in Table 5-1 and will be compared with the mean force found in the experimental tests in Figure 5-7b. The peak force found in the experiments is presented together with the corresponding peak force from the simulations for easy comparison.

As can be seen from Figure 5-4, both the progressive local folding mode and the global buckling mode can be described by the implicit simulations. Figure 5-4a shows that the simulations give a reasonable accurate description of the progressive buckling pattern found in the experimental tests. The simulations are also able to give a relatively accurate description of the global buckling mode, Figure 5-4b.

Table 5-1 Results from implicit simulations, quasi-static tests.

L (mm)	h (mm)	d_{max} (mm)	P_m (kN)	P_{max} (kN)		Mode[1]	
				Sim	Exp	Sim	Exp
640	3.35	447	41	206	218	G	P
800	3.35	549	31	202	216	G	P
400	4.39	277	143	297	291	P	P
454	4.39	318	137	293	301	P	P
480	4.39	239	90	291	292	G	G
560	4.39	276	77	284	290	G	P
640	4.39	439	62	278	284	G	G
800	4.39	180	76	272	267	G	G
1280	4.39	635	33	263	267	G	G

[1] G = global buckling, P = progressive buckling and T = transition.

| a) L = 400 mm, h = 4.5 mm | b) L = 640 mm, h = 4.5 mm |
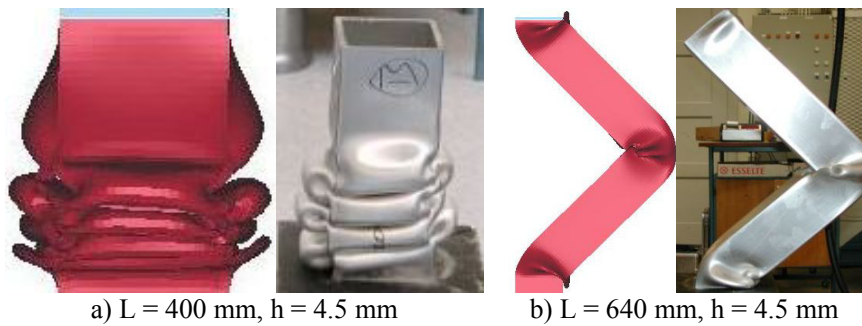
Figure 5-4 Collapse modes, implicit simulations of quasi-static tests.

In both simulations and experimental tests it was observed that the deformation started at the clamped end for the specimens with wall thickness 4.5 mm.

The simulations gave a reasonably good prediction of the collapse modes for members with wall thickness 4.5 mm, see Figure 5-5. For members with wall thickness 3.5 mm the critical buckling length is under-predicted. Global buckling was predicted even for the shortest members.

As can be seen from Figure 5-6, the implicit simulations give a very accurate description of the force-displacement history for members with wall thickness

4.5 mm collapsing in progressive local folding and in global buckling. Both the peak force and the force-displacement history are well described.

Correlation plots for peak and mean force for members with wall thickness 4.5 mm are given in Figure 5-7. Only the tests where the correct collapse modes were found are presented. A very good agreement between the peak force in the tests
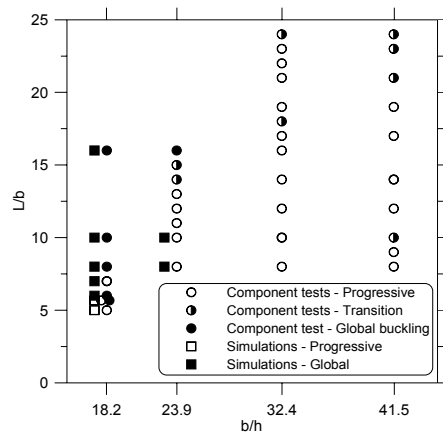
Figure 5-5 Response implicit simulations.

a) L = 400 mm, h = 4.5 mm   b) L = 640 mm, h = 4.5 mm
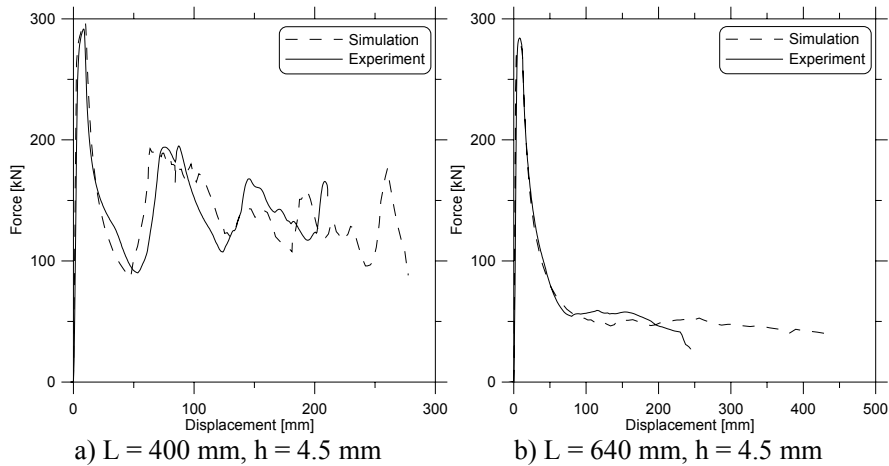
Figure 5-6 Force displacement plots, implicit simulations of quasi-static experiments.

a) Peak force   b) Mean force
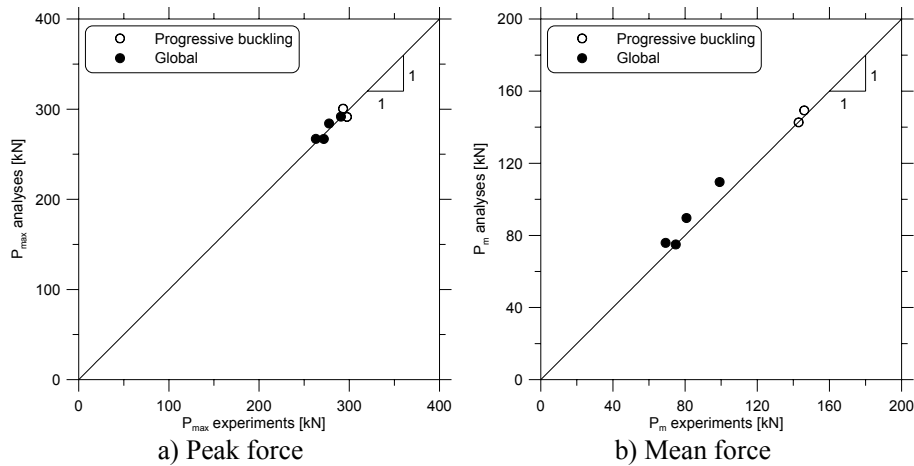
Figure 5-7 Correlation plots, implicit simulations of quasi-static tests.

and in the implicit simulations is found, see Figure 5-7a. The deviation is less than 2.7 % regardless of collapse mode. The correlation in mean force is also relatively good, see Figure 5-7b, especially for the members collapsing in progressive folding mode. The mean force is calculated at the same level in both experiments and simulations.

The implicit version of LS-DYNA gave a very good agreement with the experimental tests for members with wall thickness 4.5 mm, both with respect to collapse mode and force level. Unfortunately numerical instabilities led to premature ending of the simulations for members with wall thickness 2.0 mm and 2.5 mm. Numerous variations of the implicit parameters in the keyword file was tried but to no avail. Thus, the quasi-static experiments were attempted modelled with the explicit version of LS-DYNA.

5.2.1.2 Explicit simulations

The quasi-static tests were performed at a constant deformation speed of 150 mm/min. It is not feasible to do the explicit numerical simulations with the

same deformation speed without increasing the critical timestep. Two alternative methods of applying the deformation were investigated. Using a constant deformation speed of 150 mm/min and using mass scaling to increase the critical time step. The other method was to start with a low deformation speed and increase the velocity gradually.

When using mass scaling in explicit simulations of quasi-static problems, the mass scaling will introduce undesired kinetic energy to the system. It is important that the kinetic energy and the change in kinetic energy are small compared to the internal energy and the change in internal energy, respectively. Even if these objectives were fulfilled it was found that the mass scaling could have a rather strong influence on the local and global collapse mode. Only extensional local collapse modes were found in the simulations with wall thickness 4.5 mm even in simulations with a relatively limited amount of mass scaling. In addition mass scaling will increase the inertia forces which may prevent global buckling or a transition from progressive to global buckling. Some initial simulations showed a very poor agreement with the experimental tests and it was concluded that mass scaling was not usable in this type of simulations.

Ramping up the velocity did not introduce any numerical difficulties. However, a very bad agreement with experimental tests was found. Global buckling mode was not found in the simulations, and the critical buckling length was underestimated for the members with wall thickness 2.0 mm and 2.5 mm, and overestimated for members with wall thickness 3.5 mm and 4.5 mm. It was concluded that gradually increasing the velocity gave very poor results and could not be used in the simulation of quasi-static tests.

It was concluded that using an explicit code to simulate the quasi-static experiments yielded very poor results. The implicit code gave better results, but numerical problems were encountered.

5.2.2 Dynamic analysis

The results from the simulations of dynamic tests are presented in Table 5-2 and Table 5-3. The mean force for the simulations is calculated at the deformation level given in the third column in the tables and will be compared with the mean force found in the experimental tests in Figure 5-12. For comparison the collapse mode from the corresponding experimental test is presented in the same table.

As in the implicit simulations a relatively good description of the progressive buckling pattern was found, see Figure 5-8a. The model is also capable of giving a relatively accurate description of the transition from progressive to global buckling mode, see Figure 5-8b. However, the direct global buckling mode that was found in the impact tests for members with 4.5 mm wall thickness at 13 m/s was not found in the numerical simulations.

In the experiments global, progressive and transition deformation modes were observed at an impact velocity of 13 m/s for members with wall thickness 4.5 mm. Members with wall thickness 2.0 mm, 2.5 mm and 3.5 mm collapsed in either progressive buckling or in transition between progressive and global buckling, see Figure 5-9a. At 20 m/s all members collapsed in either progressive or in transition mode independent of wall thickness, see Figure 5-9b. As earlier mentioned, only

a) $v_0 = 13$ m/s   b) $v_0 = 13$ m/s
L = 1120 mm, h = 2.5 mm   L = 1520 mm, h = 2.0 mm

Figure 5-8 Collapse modes, explicit simulations of dynamic tests.

Table 5-2 Results from explicit simulations, V_0 = 13 m/s.

L	h	d_{max}	P_m	Mode[1]	
(mm)	(mm)	(mm)	(kN)	Sim.	Exp.
1120	1.93	784	26	P	-
1200	1.93	840	26	T	P
1280	1.93	896	27	P	P
1360	1.93	952	27	P	P
1440	1.93	1008	24	T	P
1520	1.93	1064	23	T	T
1600	1.93	1120	23	T	T
960	2.47	672	42	P	P
1120	2.47	784	41	P	P
1200	2.47	840	42	P	P
1280	2.47	896	42	P	P
1360	2.47	952	41	P	T
1440	2.47	1008	41	P	-
1520	2.47	1064	41	P	-
1600	2.47	1120	32	T	T
800	3.35	560	73	P	P
880	3.35	616	74	P	P
1120	3.35	784	73	P	P
1200	3.35	840	73	P	P
1280	3.35	896	61	T	-
1360	3.35	952	62	T	P
1440	3.35	1008	53	T	P
1600	3.35	1120	62	T	T
680	4.39	450	143	P	P
800	4.39	511	142	P	P
880	4.39	550	140	P	G
960	4.39	637	136	P	P
1040	4.39	719	134	P	P
1120	4.39	784	134	P	T
1200	4.39	840	133	P	G
1280	4.39	896	117	T	-
1360	4.39	916	109	T	G
1600	4.39	1082	93	T	G

[1] G = global buckling, P = progressive buckling and T = transition.

Table 5-3 Results from explicit simulations, $V_0 = 20$ m/s.

L (mm)	h (mm)	d_{max} (mm)	P_m (kN)	Mode[1]	
				Sim.	Exp.
640	1.93	434	30	P	P
800	1.93	539	30	P	P
880	1.93	591	29	P	P
960	1.93	643	29	P	-
1040	1.93	728	29	P	-
1120	1.93	784	29	T	P
1200	1.93	840	28	T	-
1280	1.93	896	29	T	-
1440	1.93	1008	24	T	T
1520	1.93	1064	28	T	T
640	2.47	427	46	P	P
800	2.47	528	45	P	P
880	2.47	578	45	P	-
960	2.47	672	44	P	-
1040	2.47	728	44	T	-
1120	2.47	784	43	P	P
1200	2.47	840	43	P	-
1280	2.47	896	43	T	P
1360	2.47	952	43	T	T
1440	2.47	1008	42	P	T
1520	2.47	1064	40	T	-
1600	2.47	1120	42	T	-
640	3.35	409	84	P	P
800	3.35	560	84	P	P
960	3.35	672	79	P	P
1120	3.35	784	78	P	P
1360	3.35	952	76	P	-
1440	3.35	1008	74	P	P
1520	3.35	1064	64	T	P
1600	3.35	1120	63	T	T
1760	3.35	972	69	T	P
1840	3.35	1288	63	T	T
1920	3.35	1344	57	T	T
640	4.39	383	141	P	P
800	4.39	516	134	P	P
960	4.39	649	131	P	P
1120	4.39	766	129	P	P
1440	4.39	912	126	P	P
1600	4.39	951	126	P	P
1760	4.39	947	126	P	P
1840	4.39	914	131	P	P
1920	4.39	907	132	T	T

[1] G = global buckling, P = progressive buckling and T = transition.

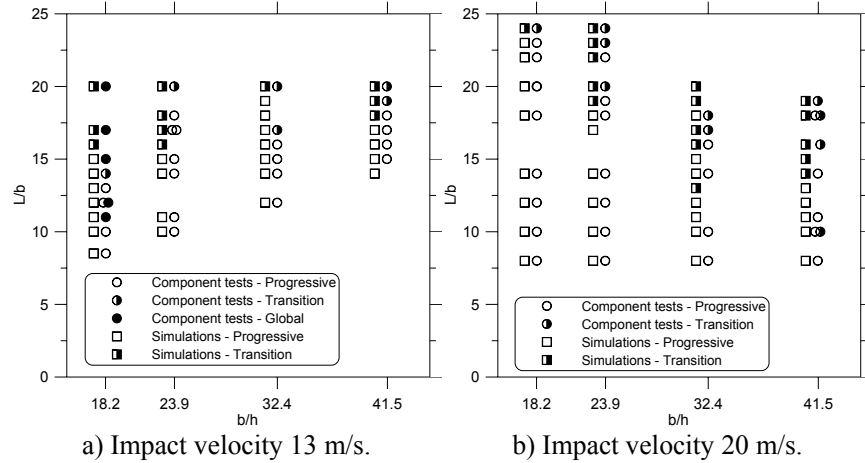a) Impact velocity 13 m/s.   b) Impact velocity 20 m/s.

Figure 5-9 Response.

progressive and transition mode were observed in the simulations for all wall thicknesses at both impact velocities. As can be seen from Figure 5-9, a relatively good agreement is found between the numerical simulations and the experimental results. The critical buckling length is in some cases over- or underestimated, but the general trend is captured. However, the numerical simulations were not capable of predicting the global buckling mode observed in the tests specimens with wall thickness 4.5 mm at an impact velocity of at 13 m/s. This may be the cause of the over-prediction of the critical buckling length of members with wall thickness 4.5 mm.

In the experimental tests with impact velocity 13 m/s, it was observed that the deformation started at the clamped end for all members with wall thickness 2.0 mm, 2.5 mm and 3.5 mm. The starting point was more random for members with wall thickness 4.5 mm. In the simulations, the deformation started at the clamped end for all members with thickness 2.0 mm and 2.5 mm. However, for the members with wall thickness 3.5 mm and 4.5 mm the deformation started at the impacted end in all the simulations.

At 20 m/s the formation of the first lobes was more or less random for the members with wall thickness 2.5 mm and 4.5 mm in the experimental tests. In seven of the tests with a wall thickness 2.0 mm the deformation started at the impacted end and only once at the clamped end. For nine of the tests with a wall thickness of 3.5 mm the deformation started at the clamped end and only once at the impacted end. In the simulations the deformation started at clamped end for all specimens with wall thickness 3.5 mm and 4.5 mm. In the more thin-walled members with wall thickness 2.0 mm and 2.5 mm, the formation of lobes started simultaneously at both ends, see Figure 5-10. This tendency to form lobes at both ends was to some degree also observed in the experimental tests.
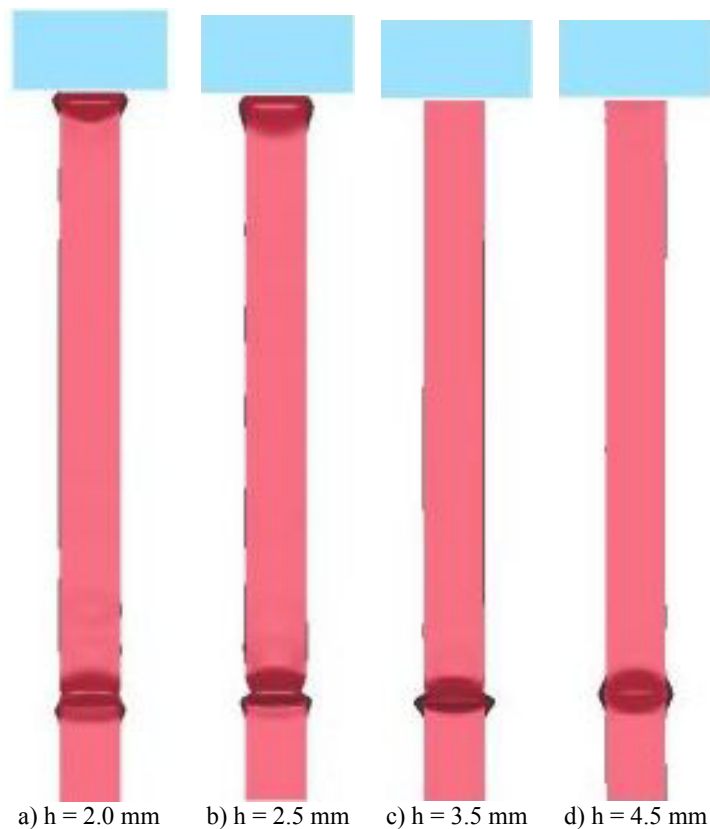

a) h = 2.0 mm   b) h = 2.5 mm   c) h = 3.5 mm   d) h = 4.5 mm

Figure 5-10 Formation of first lobes at 20 m/s.

Figure 5-11 shows that the force level is underestimated by the numerical model for members collapsing in both progressive and transition mode. The reasons for this will be discussed later. As can be seen from Figure 5-11b there is a drop in force level when the transition from progressive to global buckling occurs. It is obviously important that the model is capable of predicting this transition.

The mean force was calculated at the total deformation, d_{max}, in Table 5-2 and Table 5-3, which in most cases corresponds to a deformation equal to approximately 70 % of the free length of the members. In some of the simulations with a transition from progressive to global buckling mode, the contact between the impactor and the tests specimen was lost, thus the mean force had to be calculated at a lower level of deformation. The mean force plotted in Figure 5-12, however, is calculated at the same deformation level as the mean force of the corresponding experimental tests. In Figure 5-12 only the results from members collapsing in progressive mode in both the numerical simulations and experimental tests are presented. The mean force level for members collapsing in a transition mode is very dependent on the time of transition and the transition seldom occurs at exactly
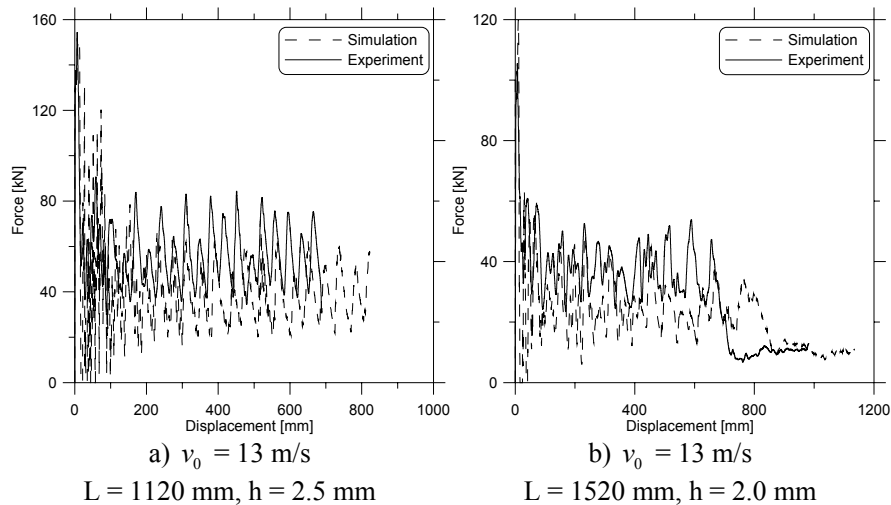

a) v_0 = 13 m/s

L = 1120 mm, h = 2.5 mm

b) v_0 = 13 m/s

L = 1520 mm, h = 2.0 mm

Figure 5-11 Force-displacement plots, explicit simulations.

the same level of deformation in the simulations and experimental tests, thus the comparison of members collapsing in a transition from progressive to global buckling mode is omitted. As can be seen from Figure 5-12, the mean force level is underestimated in the numerical simulations. In the simulations with impact velocity 13 m/s the mean force is underestimated with 42 %, 36 %, 27 % and 12 % for the 2.0 mm, 2.5 mm, 3.5 mm and 4.5 mm respectively. At 20 m/s the mean force is underestimated with 23 %, 26 %, 16 % and 14 % respectively. The deviation in mean force is decreasing for increasing wall thickness.

The baseline model gives a very good prediction of the collapse modes found in the experimental tests, but the mean force level is underestimated. Thus, in the parametric study in Section 5.3 the main focus has been placed on the collapse mode of the extrusions and not on the force level. Reyes et al (2002, 2003, 2004) also found LS-DYNA to underestimate the mean force level when studying oblique loading of aluminium extrusions.
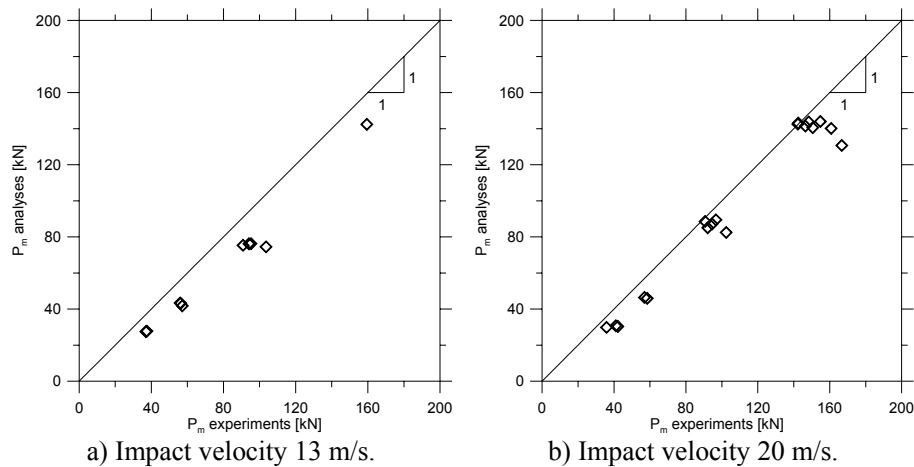

a) Impact velocity 13 m/s.   b) Impact velocity 20 m/s.

Figure 5-12 Correlation plot mean force explicit simulations of impact tests.

5.2.3   Improvement of the baseline model

As mentioned in Section 5.2.2 the mean force level is underestimated in the explicit simulations. In this section, focus will be on identifying the cause of this underestimation of mean force level. The influence from both physical and purely numerical parameters will be investigated. When comparing the mean force level it corresponds to an axial deformation of 66 % of the initial length of the test specimens.

5.2.3.1 Corners

Some simplifications with respect to geometry were done in the numerical model. The cross-section was modelled as perpendicular plates with constant wall thickness. The cross-section of the tested extruded members, however, has a small curvature at the corners and a somewhat larger wall-thickness in this area, see Figure 5-13.

The curvature in the corners leads to a somewhat larger cross-sectional area. Through some simple geometrical considerations the total increase in cross sectional area was found to be 13.76 mm^2 independent on wall thickness.
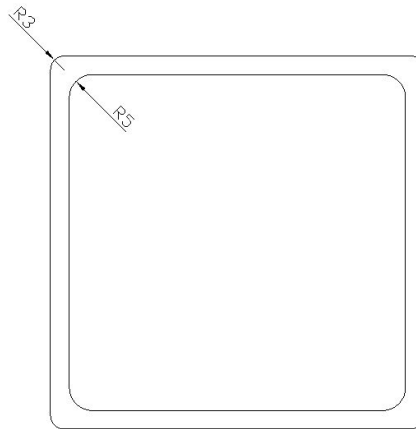

Figure 5-13 Corner geometry.

In order to take the increased cross-sectional area into account the wall thickness in the two corner elements was increased. The relative increase in cross-sectional area and element thickness is presented in Table 5-4. As the outer curvature of the corners is relatively high it was chosen to continue modeling the corners with perpendicular walls.

It is well known that a major part of the energy absorption for square tubes collapsing in an axi-symmetric mode takes place in the corner section. Thus a small increase in cross-sectional area might lead to a significant increase in mean force since the additional cross-sectional area is located in the corner elements.

The length of the member was kept constant at 800 mm, and four specimens with wall thickness 2.0 mm, 2.5 mm, 3.5 mm and 4.5 mm, respectively, were analysed at an impact velocity of 20 m/s.

Changing the wall thickness in the two corner elements did not have any effect on the folding mode. However, with an exception of the members with wall thickness 3.5 mm the mean force was increased for all simulations. The increase in mean force level was 10.47 %, 7.15 % and 3.42 % for the members with 2.0 mm, 2.5 mm and 4.5 mm respectively. It was as expected that the increase in force was larger for the more thin-walled members as the relative increase in cross-sectional area was larger for these members. However, the decrease in mean force level of 2.71 % for the member with 3.5 mm wall thickness was unexpected. It can be concluded that some of the reduced mean force level in the numerical simulations compared to the experimental test can be attributed to the simplified modeling of the corners.

Table 5-4 Corner properties.

Wall thickness	2.0 mm	2.5 mm	3.5 mm	4.5 mm
Increase in cross sectional area	2.28 %	1.80 %	1.34 %	1.04 %
Increase in corner element thickness	22.76 %	17.91 %	13.36 %	10.33 %

5.2.3.2 Amplitude of local imperfections

The cross-sectional imperfections used in the baseline simulations were based on the production tolerances given by the extrusion supplier. It was assumed that the amplitude of the local imperfections would have little influence on the mean force level as long as they were large enough to trigger the correct deformation mode.

Søvik Opheim (1996) measured the initial imperfections of a 500 mm length of an aluminium alloy 6060 temper T4 extrusion with wall thickness 2.5 mm. An irregular imperfection pattern with maximum amplitude of 0.07 mm (b/2286) was found. The data is limited, and does not allow for general conclusions regarding the distribution and amplitude of initial out-of-plane imperfections (Søvik Opheim, 1996).

Simulations of an 800 mm long member with a wall thickness of 2.5 mm with varying amplitude of local imperfection were carried out. In the baseline simulations the amplitude of local imperfections, δ_l, was b/200. Four simulations with local imperfection amplitude of b/100, b/400, b/800 and b/2000 were run at an impact velocity of 20 m/s.

Mean force vs. displacement curves are presented in Figure 5-14a. As can be seen from the figure the force vs. displacement history is influenced by the choice of amplitude of the local imperfections. The mean force is increased by 8.58 %, 9.31 % and 10.08 % for initial imperfections of b/400, b/800 and b/2000 respectively. As can be seen from Figure 5-14b there is a lot of high frequency oscillations in the force level. This is probably due to elastic stress waves propagating in the member. These oscillations were not present when the amplitude of the local imperfection was equal or larger than b/200.

a) Mean force vs. displacement.

b) Force vs. displacement
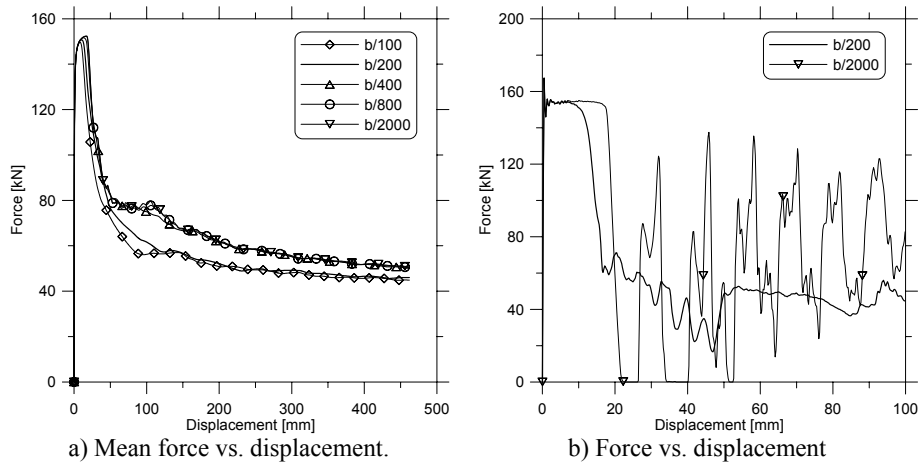
Figure 5-14 Influence from amplitude of local imperfections.

From Figure 5-14a it can be concluded that the mean force level is converging towards a constant value for local imperfections amplitudes of b/400 or less.

As can be seen from Figure 5-14b the peak force is not heavily influenced by the choice of local imperfection amplitude. Since the stresses are well inside the plastic area this is not unexpected in a material experiencing a limited amount of strain hardening.

Some additional simulations on a more thick-walled member with wall thickness 3.5 mm and 4.5 mm were preformed. The results from members with wall thickness 3.5 mm are not conclusive, see Table 5-5. However, as can be seen from Figure 5-15, a decrease in local imperfection amplitude leads to a change in folding mode for members with wall thickness 4.5 mm.

The extruded members started folding in an extensional mode instead of the axisymmetric mode that was observed in the experimental tests, and a transition from progressive to global buckling occurred in one simulation.

$$\delta_l = b/100 \qquad \delta_l = b/200 \qquad \delta_l = b/400 \qquad \delta_l = b/2000$$
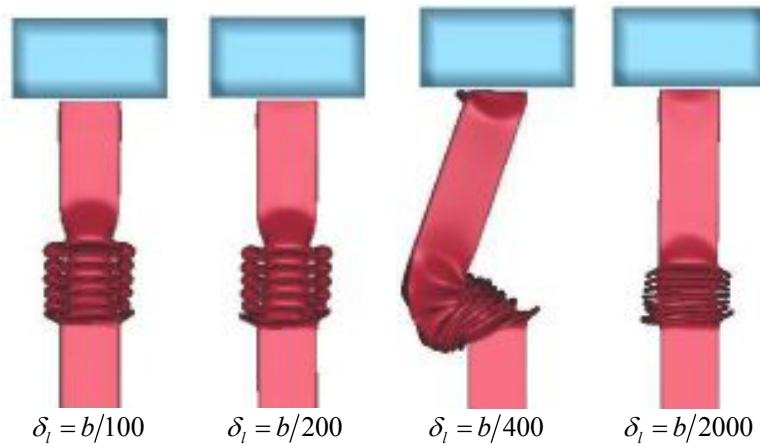
Figure 5-15 Influence from local imperfection amplitude on buckling mode of members with wall thickness 4.5 mm.

From the simulations it can be concluded that the amplitude of the imperfections might have an influence on the mean force level but great care should be taken in order not to trigger the wrong local deformation mode. It is possible that the imperfection amplitude is dependent on the wall-thickness.

5.2.3.3 Strain rate

In the baseline model the material is assumed to be strain rate insensitive. However, material tests performed by Enjalbert (2003) have shown that there is a small strain rate sensitivity in aluminium alloy 6060-T6. Even though the strain rate sensitivity is small it may have an influence on both the mean force level and the behaviour of the extruded members, i.e. the transition from progressive to global buckling. Enjalbert (2003) performed tensile tests on specimens cut from aluminium alloy 6060-T6 tubes in a hydraulic testing machine and in a "Split Hopkinson Tension Bar". Specimens cut from a tube with wall thickness 4.5 mm were tested at different strain rates. Figure 5-16 shows the strain rate sensitivity at different levels of plastic strain.
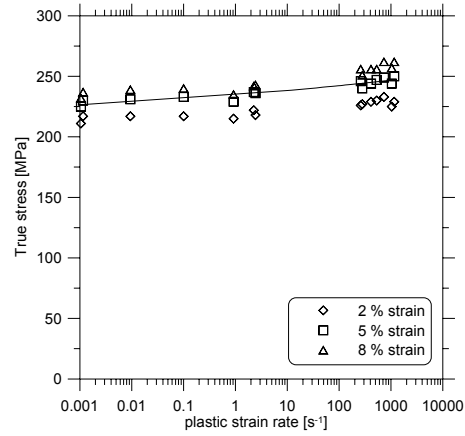
Figure 5-16 Strain rate sensitivity in aluminium alloy 6060-T6 (Enjalbert, 2003)*.*

As can be seen from the figure there is a small positive strain rate sensitivity in aluminium alloy 6060-T6. To take strain rate effects into account material model 103 in LS-DYNA was used

$$\sigma_{eff}\left(\varepsilon_{eff}^{p},\dot{\varepsilon}_{eff}^{p}\right)=\sigma_0+\sum_{i=1}^{2}Q_i(1-\exp(-C_i\varepsilon_{eff}^{p}))+V_k\dot{\varepsilon}_{eff}^{p\ Vm} \qquad (5\text{-}1)$$

Using the method of least squares the constants V_k and V_m was estimated to 26.05 and 0.055 at a plastic strain level of 0.005. It was assumed that the strain rate sensitivity was the same for all wall thicknesses.

To establish the influence from strain rate on the mean force level, simulations of an 800 mm long extruded tube were performed at 13 m/s and 20 m/s. Four thicknesses were tested at both impact velocities. In addition, a simulation series with constant wall thickness of 2.5 mm at 20 m/s and varying length was performed to investigate the influence from strain rate on the transition from progressive to global buckling.

The simulations showed that the influence from the strain rate on the mean force level was very small for most combinations of wall thickness and velocities. At 13 m/s the change in mean force was less than ± 1 % independent of wall thickness. However, at 20 m/s an increase in mean force level of 8.85 % was observed for the 2.0 mm thick specimen. For the other wall thicknesses the change in mean force level was relatively small.

The simulation series with constant wall thickness 2.5 mm and impact velocity 20 m/s showed that the strain rate sensitivity had an effect on the transition from progressive to global buckling. The specimen with length 1360 mm collapsed in a transition mode in the simulations without strain rate effects and in a progressive mode in the simulations with strain rate sensitivity. For the member with length 1400 mm the opposite was observed.

From the simulations it can be concluded that the strain rate sensitivity has minimal influence on the mean force level. However, it may influence the transition from progressive to global buckling.

5.2.3.4 Self contact

As the extruded tube deforms, contact between the lobes will occur. Thickness offsets are not included in surface to surface and node to surface contact algorithms. In single surface contact algorithms they are always included. However, the default thickness $h_{contact}$ used in the contact formulation is given by

$$h_{contact} = \min\left(h_{initial}, 0.4 \cdot l_{edge}\right) \qquad (5\text{-}2)$$

where $h_{initial}$ is the initial shell thickness and l_{edge} is the length of the side edge of the shell element. In thin shells this is not a problem as the thickness of the shell is much smaller than the other dimensions, but for thick shells the thickness and the

length of the side edge can be of similar size and the thickness used in the contact formulation will be much smaller than the real thickness.

In the current simulations an element size of 4x4 mm is used giving a shell thickness in the contact formulation of 1.6 mm. Simulations were carried out using the shell thickness in the contact formulation equal to the initial thickness of the shell. All four thicknesses were tested at an impact velocity of 20 m/s. A decrease in mean force level of 6.75 % was found for the member with wall thickness 3.5 mm. For the other thicknesses the change in mean force level was less than 1 %. Thus it was concluded that the use of the actual thickness in the contact algorithm in LS-DYNA had little influence on the mean force level. The thickness of the shell will change during deformation, this thickness change is per default not included in the contact formulation of LS-DYNA. However, since the use of the actual thickness had very little influence on the mean force level, it was assumed that the change in mean force because of the change of thickness in the contact algorithm would have a very small influence on the mean force.

5.2.3.5 Element type

In the simulations, Belytschko-Tsai (type 2) (Hallquist, 2003) shell elements were used. This element type is very CPU efficient and thus a natural choice. Two other element types were tested, namely the Hughes-Liu element (type 1) (Hallquist, 2003) and a fully integrated element (type 16) (Hallquist, 2003). Again all four thicknesses were tested at an impact velocity of 20 m/s. The length was kept constant at 800 mm.

When using the Hughes-Liu elements (type 1) there were some problems with hourglassing for the member with wall thickness 4.5 mm and the simulations ended prematurely. For the other thicknesses a decrease in mean force level in the range of 0.24 – 3.4 % was observed.

The fully integrated element type 16 gave an increase in force level of 4.21 %, 3.50 % and 1.20 % for the members with wall thickness 2.0 mm, 2.5 mm and 4.5 mm respectively. The member with wall thickness 3.5 mm experienced a decrease in force level of -4.59 %.

The simulations with different element types are not conclusive, but it seems that the choice of element type does not have any major influence on the mean force level.

5.2.3.6 Summary

Table 5-5 summarizes the effect on the mean force level from the different investigated parameters. The table gives the percentage increase/decrease compared to the baseline model.

It can be concluded from Table 5-5 that the amplitude of the local imperfections is the most important parameter influencing the mean force level. The tendencies were not that conclusive for the other parameters investigated. However, it seems that modelling of the corners and the use of element type 16 have in general a positive effect on the mean force level.

Table 5-6 gives the relative CPU cost for the different parameters investigated in this study. Studying the CPU cost directly may be misguiding as it is very dependent on the number of cycles needed in the simulation. The number of cycles in one simulation may be significantly increased if one element experiences a large decrease in size. Thus, in Table 5-6 the relative CPU cost pr cycle for the investigated parameter and the baseline model is presented.

Table 5-6 shows that only the change of element type leads to a significant increase in relative CPU cost. For all other parameters the increase in relative CPU cost is

73 % or less. Especially the use of the fully integrated element type 16 is very CPU costly.

The influences from the different parameters presented in Table 5-5 are not necessarily additive. In order to check this, a simulation including all the parameter variations that had a positive effect on the mean force was carried out. The 2.5 mm thick specimen was selected and element type 16, local imperfection amplitude of b/2000 and thicker corners were used.

Table 5-5 Influence on mean force level from some selected parameters.

	2.0 mm	2.5 mm	3.5 mm	4.5 mm
Corners	+10.47 %	+7.15 %	-2.71 %	+3.42 %
Imperfections (b/100)	-	-2.55 %	-12.88 %	-1.42 %
Imperfections (b/400)	-	+8.59 %	-6.08 %	+11.06 % [1]
Imperfections (b/800)	-	+9.31 %	+2.28 %	-
Imperfections (b/2000)	-	+10.08 %	-3.80 %	+13.77 % [1]
Strain rate (13 m/s)	+0.22 %	+0.10 %	+0.00 %	-0.98 %
Strain rate (20 m/s)	+8.85 %	+0.20 %	-2.67 %	+0.16 %
Contact	-0.08 %	+0.54 %	-6.75 %	+0.69 %
Element type 16	+4.21 %	+3.50 %	-4.59 %	+1.20 %
Element type 1	-0.29 %	-0.24 %	-3.40 %	HG[2]

[1] Mode change.

[2] Simulation terminated because of hourglassing.

Table 5-6 Relative CPU cost.

	2.0 mm	2.5 mm	3.5 mm	4.5 mm	Average
Corners	1.17	1.03	1.02	0.89	1.03
Imperfections (b/100)	-	1.00	-	-	-
Imperfections (b/400)	-	1.01	-	-	-
Imperfections (b/800)	-	1.02	-	-	-
Imperfections (b/2000)	-	1.03	-	-	-
Strain rate (13 m/s)	1.24	1.15	1.31	1.23	1.23
Strain rate (20 m/s)	1.73	1.31	1.20	1.15	1.35
Contact	1.14	0.97	0.78	0.98	0.97
Element type 16	4.20	3.53	3.21	3.53	3.62
Element type 1	2.09	1.45	1.43	HG[1]	1.66

[1] Simulation terminated because of hourglassing.
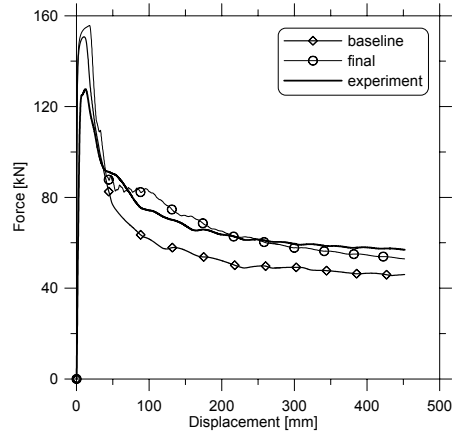
Figure 5-17 Mean force level using the updated numerical model.

As can be seen from the figure the mean force is increased with 15.31 % compared to the baseline model. However, the updated model still underestimates the mean force level with 6.87 % compared to the experimental tests at a deformation of 453 mm. The author can at the present time not give an adequate explanation for this, but as earlier mentioned Reyes et al. (2003) also reported that LS-DYNA gave conservative predictions of the mean force.

5.3   Parametric study

The baseline model establish in Section 5.2 has been used in a parametric study on the response of axially loaded thin-walled extrusions. The parameters that have been investigated in this section are the impact velocity, material properties and the use of a trigger to stabilize the deformation to a progressive buckling mode. Since the numerical model underestimates the mean force level the main focus has been on the collapse mode.

5.3.1 Velocity

The experimental tests in Section 4 and numerical simulations in Section 5.2 show that the response of axially loaded aluminium extrusions is sensitive to the impact velocity. Thus, in this section the influence of velocity on the critical global slenderness and mean force level for members collapsing in progressive buckling has been investigated.

To reduce the number of simulations it was chosen to focus on one local slenderness ratio. The width and thickness was kept constant at 80 mm and 2.5 mm respectively. This is a typical combination of width/thickness for components in a spaceframe. The main focus in this section has been on the collapse mode and not on the force level. The experimental tests showed that the critical global slenderness was decreased in the impact tests compared to the quasi-static tests. For the chosen geometry the critical global slenderness was approximately the same in impact tests with 13 m/s and 20 m/s.

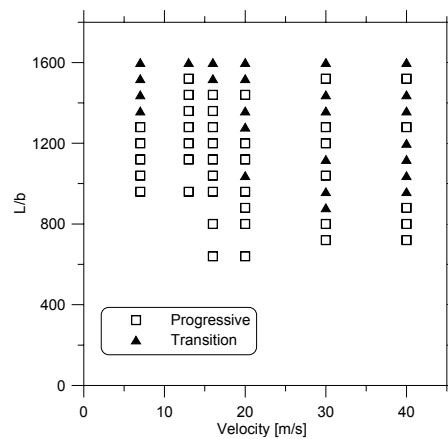The collapse modes found in the numerical simulations are presented in Figure 5-18.

Figure 5-18 Collapse mode vs. velocity.

The critical global slenderness increased with the velocity from 7 to 13 m/s. A further increase in impact velocity led to a decrease in critical global slenderness. It was observed that the members had a tendency to develop lobes at several places along the length of the member simultaneously, thus making the member more unstable and increasing the probability of a transition from progressive to global buckling. As the figure shows, an increasingly anomalous response was observed when the impact velocity was increased to 20 m/s and above. This makes it difficult to give a definite value for the critical global slenderness.

Figure 5-19 shows the average mean force vs. velocity for members collapsing in progressive buckling mode. As expected the average mean force is increasing for increasing velocity.

The mean force appears to increase linearly for increasing impact velocity. This is in agreement with the results obtained by Hanssen et al. (2000) and Langseth et al. (1999).

In conclusion, the response of the axially loaded aluminium extrusions is very dependent on the impact velocity. The mean force is increasing linearly with the
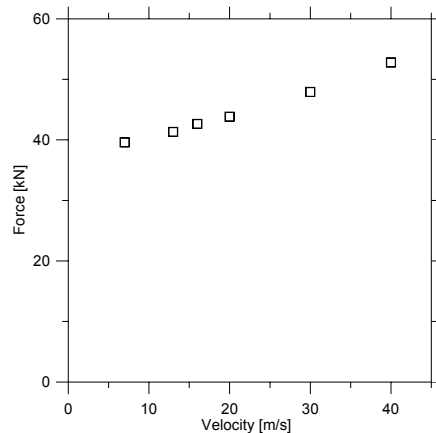
Figure 5-19 Mean force vs. velocity.

impact velocity but the global stability will decrease and the response will be more anomalous.

5.3.2   Temper

To study the influence from the material properties on the structural behaviour, simulations using the material properties of AA6060 temper T4 (Reyes et al., 2003) were carried out. A comparison between the strain hardening properties of AA6060 T4 and T6 is presented in Figure 5-20.

As can be seen from Figure 5-20, the temper T6 material has a relatively high yield strength and little strain hardening compared to the temper T4 material. The strain-hardening properties were the only difference between the model used in this and previous chapters.

Components with a wall thickness of 2.5 mm impacted at 13 m/s and 20 m/s were studied. Figure 5-21 shows the deformation of the members at an early stage.
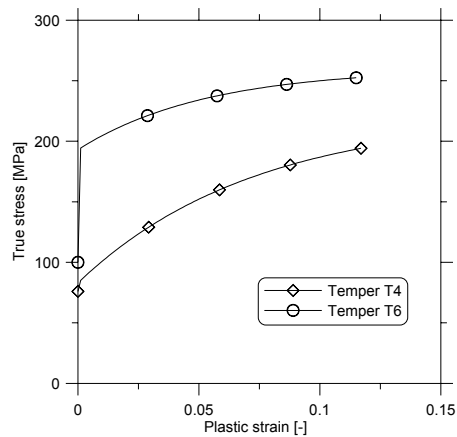
Figure 5-20 Strain hardening curves for temper T4 and T6.

Temper T6 $v_0 = 13$ m/s	Temper T4 $v_0 = 13$ m/s	Temper T6 $v_0 = 20$ m/s	Temper T4 $v_0 = 20$ m/s

a)	b)	c)	d)

Figure 5-21 Buckling pattern, L=1120 mm and h=2.5 mm.

The deformation pattern is quite similar for the members in Figure 5-21a, b and c. The deformation is localized at one or both ends. In Figure 5-21d a typical example of dynamic plastic buckling can be observed. This was only observed for the T4 members at 20 m/s. Dynamic plastic buckling is characterized by an initial wrinkling within a sustained plastic flow along the shell length during the first phase of deformation. According to Karagiozova and Jones (2004, 2002) dynamic plastic buckling can occur in square tubes for high velocity impacts and particular material properties. In general, when the components start to develop folds

simultaneously along the length of the member, they become unstable and a transition from progressive to global buckling occurred for relatively short columns.

In Figure 5-22 a comparison of the response of members made from extrusions in temper T4 and T6 is presented.

Figure 5-22 shows that the critical global slenderness is significantly reduced for the T4 members. However, the anomalous response that was observed at 20 m/s with members made of 6060-T6 was not present for members made of 6060-T4. At 20 m/s the decrease in critical global slenderness is probably related to the dynamic plastic buckling that was observed in the members made of 6060-T4. The initial wrinkling weakens the stability of the member and the transition from progressive to global buckling will occur for relatively short columns. At 13 m/s it was observed that the deformation was localized at both ends for the columns in temper T4, whereas the members made of 6060-T6 experienced folding either at the impacted or clamped end. It is believed that folding at the clamped and impacted end at the same time will reduce the stability of the column and thus increase the probability of a transition from progressive to global buckling.
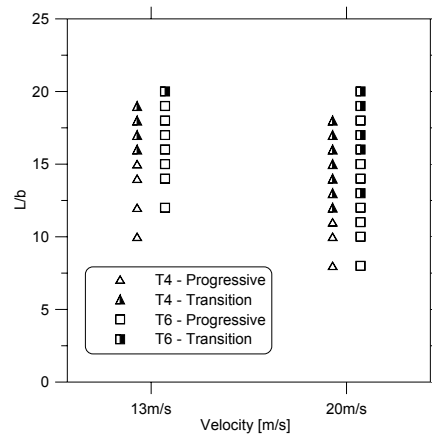

Figure 5-22 Response T4 vs. T6.

In summary, the average mean force for members in temper T4 collapsing in progressive buckling mode was 31.55 kN and 35.30 kN at 13 m/s and 20 m/s respectively. The mean force was calculated at a deformation length equal to 70 % of the original length of the member. This is a reduction in mean force of 23.88 % and 19.34 %, respectively, compared to the simulations with the T6 members.

The critical buckling length was significantly reduced for the temper T4 members compared to the temper T6 members. This is partly because of the dynamic plastic buckling mode that was found in the high speed simulations for the T4 members. As expected, a reduction in mean force was observed compared to the T6 specimens.

5.3.3   Triggers

The behaviour of the extruded profiles was found to be dependent on the position of the first lobes. Different methods are currently being used to control the deformation behaviour of thin-walled aluminium extrusions, e.g. non-uniform plate thickness, tilted partitions or other geometrical details. The physical geometrical features are, however, often time consuming and expensive to produce (Bjørneklett and Myhr, 2003). Bjørneklett and Myhr (2003) used local material design to initiate a favourable buckling mode as a means of controlling the energy absorption in a product during crash. This type of design feature is highly cost-effective compared to alternative processes of making complex protrusions, embossments, stampings etc (Bjørneklett and Myhr, 2003).

By introducing a thermally induced trigger at the impacted end an attempt to increase the critical global slenderness was made. Bjørneklett and Myhr (2003) showed that the yield stress can be reduced over a very limited area. The borders between areas with different yield strength are relatively sharp. Bjørneklett and Myhr (2003) used a heat induced trigger with a width of 20 mm situated a small distance below the upper end of the extrusion. They found the heat induced trigger

to function well, the deformation was initiated at the location of the heat induced trigger and the peak force was reduced by approximately 50 % (Bjørneklett and Myhr, 2003).

In the present simulations it was chosen to model the upper 80 mm with reduced yield stress. The hardening characteristics of the heat induced trigger is not known, thus two different hardening curves were investigated for the thermally induced triggers, labelled as "material 1" and "material 2" in Figure 5-23 respectively. For "material 1", σ_0 in Equation (2-4) is reduced by 50 MPa, this will reduce the yield stress but the hardening is the same as in the base material. For "material 2", σ_0 is reduced by 50 MPa and Q_1 is increased by 50 MPa. The yield stress is reduced compared to the base material, and the strain hardening is increased.

To compare the two materials, a series of simulations for the members with 2.0 mm wall thickness impacted at 20 m/s was performed. No difference in response was observed. The collapse mode was identical for both materials and the variation in mean force was less than 0.5 %. The average peak force was 100 MPa for material 1 and 112 MPa for material 2 giving a ratio between the peak and mean force of
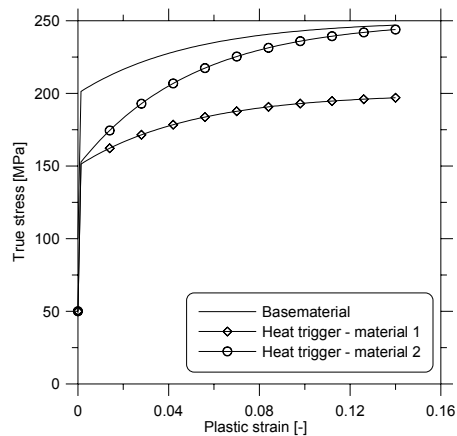

Figure 5-23 Material properties of triggers.

3.48 and 3.89 respectively. Since the difference in response was negligible, it was chosen to use only the "material 1" trigger in the subsequent simulations.

Two runs of simulations were performed, one at 13 m/s and one at 20 m/s. The same width and four thicknesses as in Section 5.2.2 were tested at both impact velocities. The deformation started at the impacted end in all simulations independent of wall thickness and impact velocity. As expected the trigger mechanism at the upper end of the extrusion lead to a reduction in peak force.

In the simulations with impact velocity 13 m/s the peak force was reduced by approximately 21% for all thicknesses. It was observed that the length of the member had no influence on the peak force. The reduction in mean force was only compared for members collapsing in progressive folding mode, since the energy absorption and thus the mean force is very dependent on the time of transition. No reduction in mean force was observed for members with wall thickness 2.0 mm and 2. 5 mm. However, a small reduction of 2.5 % was observed for the 3.5 mm thick specimens. For members with wall thickness 4.5 mm the reduction was as high as 10 %.

At an impact velocity of 20 m/s the reduction in peak force was approximately 55 % and independent of wall thickness and extrusion length. For members collapsing in progressive local folding the difference in mean force was negligible for the members with wall thickness 2.0 mm and 2.5 mm. The average reduction in mean force was 3 % and 11 % for the members with wall thickness 3.5 mm and 4.5 mm respectively.

The collapse modes found in the numerical simulations are presented in Figure 5-24.

a) $v_0 = 13$ m/s.   b) $v_0 = 20$ m/s.
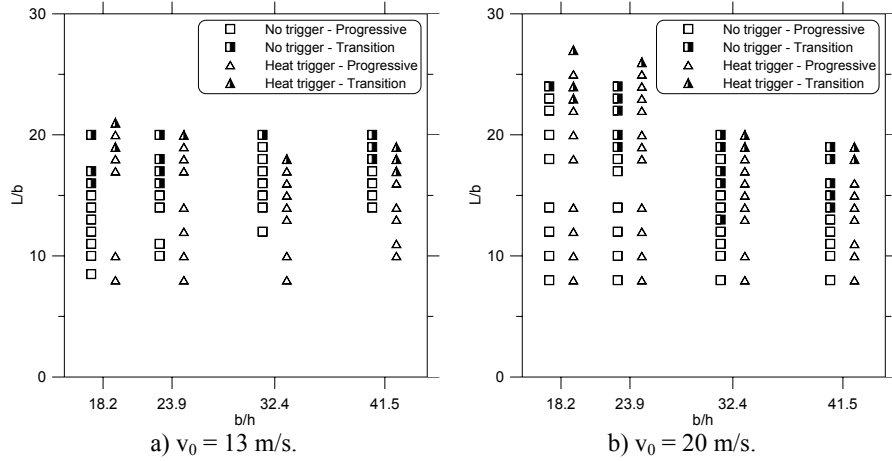
Figure 5-24 Response with heat trigger.

At 13 m/s triggering of the deformation by the heat treatment had a positive influence on the critical buckling length for the members with wall thickness 3.5 mm and 4.5 mm. However, the members with wall thickness 2.0 mm and 2.5 mm experienced a small decrease in critical buckling length.

The heat induced trigger had a better effect when the impact velocity was increasd to 20 m/s. A relatively large increase in critical global slenderness was observed for all thicknesses except 4.5 mm.

It can be concluded from the simulations that the introduction of a heat trigger in general had a very positive influence on the stability of the axial loaded components. In most cases an increase in critical global slenderness was observed. The reduction in force level was relatively small and a significant reduction in peak force was found for all thicknesses and velocities.

6   Theory

This chapter consists of three main parts. In Section 6.1 the buckling load for columns and plates will be presented. Solutions according to both elastic and plastic theories are considered. In Section 6.2 the experimental results for mean force and peak force obtained in Chapter 4 are compared with existing models and the design code Eurocode 9 (2004). Section 6.3 deals with analytical models for predicting the collapse mode of axially loaded thin-walled tubes.

6.1   Axially loaded structural components

Axially loaded components are quite common in structural and automotive design. Components in compression can collapse in several buckling modes as well as by plastification of the cross section depending on the local and global slenderness of the component.

Instability because of buckling is not necessarily associated with failure. Plate buckling in the extrusion walls leads to progressive buckling which is the favoured collapse mode in a crash box. Global buckling, however, is an undesired collapse mode due to the large lateral deflections and the reduction in energy absorption. Thus, the understanding of the different buckling modes and their interaction is important in the design of axially loaded components.

6.1.1   Column buckling

Axially loaded components made of materials such as steel and aluminium often have high slenderness. Thus they are vulnerable to buckling.

Unfortunately the term buckling is often used both for the response of a perfectly straight column loaded axially as well as when a column with imperfections is loaded laterally and axially. This mix is unfortunate, since the first example is an instability problem while the other is a second order bending problem (Larsen, 1997). In this section both problems will be considered.

It is common to divide the problem of buckling of axially loaded columns into either elastic or plastic buckling dependent on whether the column collapses in the elastic or plastic regime respectively. In general long slender columns will buckle elastically and short stocky columns will collapse in the plastic area. In the following both elastic and plastic buckling will be described.

6.1.1.1 Euler buckling

The behaviour of an axially loaded column is fairly complicated. Therefore the idealized Euler column will first be considered. Euler, as a mathematician, was interested principally in the geometrical forms of elastic curves (Timoshenko, 1982). Euler found the buckling load of a column clamped at one end and free at the other to be

$$N_E = \frac{C\pi^2}{4l^2} \tag{6-1}$$

The buckling load of an axially loaded column is derived under the following assumptions:

- ➢ Axial loading i.e. the centre of gravity of the load passes through the centre of gravity of the cross-section
- ➢ Linear elastic material, i.e. no plasticity
- ➢ The deflections are small

Using these assumptions, the Euler buckling load for an axially loaded column can easily be found as

$$N_E = \frac{\pi^2 EI}{L_k^2}$$

(6-2)

where L_k is the buckling length. The buckling length is dependent on the boundary conditions of the column. The Euler buckling stress is found by dividing the buckling load by the nominal cross-sectional area

$$\sigma_{cr}^E = \frac{\pi^2 EI}{L_k^2 A} = \frac{\pi^2 Ei^2}{L_k^2} = \frac{\pi^2 E}{\lambda_k^2}$$

(6-3)

Here the slenderness ratio $\lambda_k = L_k / i$, $i = \sqrt{I/A}$. By introducing the reduced slenderness ratio

$$\bar{\lambda}_k = \frac{\lambda_k}{\pi \sqrt{E/\sigma_{0.2}}}$$

(6-4)

where $\sigma_{0.2}$ is the 0.2 % proof strength, the relation between the dimensionless Euler critical stress and the reduced slenderness can be expressed as

$$\frac{\sigma_{cr}^E}{\sigma_{0.2}} = \frac{1}{\bar{\lambda}_k^2}$$

(6-5)

When using Equation (6-5), columns made of different materials can be compared.

6.1.1.2 Tangent modulus theory

The Euler critical stress is only valid if the material response is elastic until buckling occurs. For short columns a plastic collapse will occur at a critical stress $\sigma_{cr} < \sigma_{cr}^E$.

If strain hardening is neglected, a column is not capable of carrying a stress larger than the yield stress or proportional limit. According to Larsen (1997), a transition curve is required when the reduced slenderness is smaller than a critical limit, i.e. when

$$\lambda \leq \lambda_p = \pi \sqrt{\frac{E}{f_p}} \tag{6-6}$$

where f_p is the proportionality limit of the material. Engesser suggested in 1889 that the critical load for members with low slenderness ratio could be found by replacing the Young's modulus E in Equation (6-3) with the tangent modulus E_t, given as the slope of the stress strain curve, $E_t = d\sigma/d\varepsilon$, at buckling (Gaylord jr and Gaylord, 1972), i.e.

$$\sigma_{cr}^{pl,t} = \frac{\pi^2 E_t}{\lambda_k^2} \tag{6-7}$$

It is assumed that the column is initially perfectly straight and without internal stresses. The dimensionless critical stress according to the tangent modulus theory can be expressed in terms of the reduced slenderness ratio as

$$\frac{\sigma_{cr}^{pl,t}}{\sigma_{0.2}} = \frac{E_t}{E} \frac{1}{\bar{\lambda}_k^2} \tag{6-8}$$

The tangent modulus theory is based on the fact that there is no strain reversal when a column passes from the straight to a bent configuration (Iyengar, 1988). Shanley (1947) showed that the bending of a column may proceed simultaneously with increase in the axial load.

6.1.1.3 Double modulus theory

The tangent modulus theory was criticised by Considére (1889) and Jasinski (1895) for not taking into account the elastic strain reversal in parts of the cross-section during buckling (Larsen, 1997). The double modulus theory takes this effect into accounts by replacing the Young's modulus E with a double modulus E_r, see Equation (6-9). The double modulus for a rectangular cross section is given by (Larsen, 1997)

$$E_r = \frac{4EE_t}{\left(\sqrt{E} + \sqrt{E_t}\right)^2} \tag{6-9}$$

The dimensionless buckling stress according to the double modulus theory reads

$$\frac{\sigma_{cr}^{pl,d}}{\sigma_{0.2}} = \frac{E_r}{E} \frac{1}{\bar{\lambda}_k^2} \tag{6-10}$$

The double modulus theory will give a buckling stress that is slightly higher than the buckling stress estimated by the tangent modulus theory.

6.1.1.4 Buckling of a real column with initial imperfections

For simplicity, a pin ended column is chosen. It is assumed that the initial geometric imperfection and the total deflection are given by:

$$u_0 = \delta_0 \sin\frac{\pi x}{L} \tag{6-11}$$

$$u = \delta \sin\frac{\pi x}{L} \tag{6-12}$$

where δ_0 and δ are the initial imperfection and total deflection amplitude. L is the length of the column. Moment equilibrium of the axially loaded pin ended column gives

$$Nu = -EI\left(u_{,xx} - u_{0,xx}\right)$$ (6-13)

and when introducing Equations (6-11) and (6-12)

$$N\delta = EI\left(\frac{\pi}{L}\right)^2 [\delta - \delta_0] = N_E\left(\delta - \delta_0\right)$$ (6-14)

The deflection of the column can be expressed as a function of the initial imperfection and the axial load

$$\delta = \frac{\delta_0}{1 - N/N_E}$$ (6-15)

For simplicity a linear interaction between moment and axial load is considered

$$\sigma_y = \frac{N}{A} + \frac{M}{W}$$ (6-16)

Introducing $M = N \cdot \delta$ givers

$$\frac{N}{N_p} + \frac{M}{M_p} = \frac{N}{N_p} + \frac{N\delta}{M_p} = 1$$ (6-17)

where axial and moment capacity is given by

$$N_p = \sigma_y A$$ (6-18)

$$M_p = \sigma_y W$$ (6-19)

Introducing δ from Equation (6-15) gives the critical buckling load N_k

$$\frac{N_k}{N_p} + \frac{N_k}{M_p} \frac{\delta_0}{1 - \frac{N_k}{N_E}} = \frac{N_k}{N_p} + \frac{N_k}{N_p} \frac{N_p}{M_p} \frac{\delta_0}{1 - \frac{N_k}{N_p} \frac{N_p}{N_E}} = 1 \tag{6-20}$$

$$\frac{N_k}{N_p} = \frac{1}{2} \left[1 + \frac{1+\alpha}{\bar{\lambda}^2} - \sqrt{\left(1 + \frac{1+\alpha}{\bar{\lambda}^2}\right)^2 - \frac{4}{\bar{\lambda}^2}} \right] \tag{6-21}$$

where

$$\alpha = \delta_0 \frac{N_p}{M_p} \tag{6-22}$$

$$\bar{\lambda}^2 = \frac{N_p}{N_E} \tag{6-23}$$

The imperfection amplitude, δ_0, is often related to the length of the column, e.g. in design codes an initial imperfection amplitude of $\delta_0 = L/1000$ for a pin ended column is often used. Assuming that the initial imperfection is proportional to the length of the column, the relation between the critical buckling load and the imperfection amplitude is as given in Figure 6-1.

Be aware that the shape of the curve is a function of the imperfection amplitude δ_0 as well as the interaction curve for the cross section capacity.
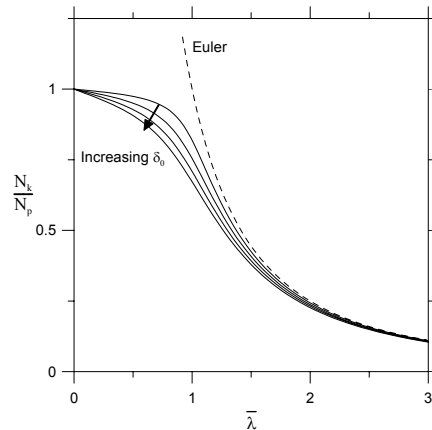
Figure 6-1 Critical load vs. imperfection amplitude.

6.1.1.5 Comparison

Experiments on small specimens of rectangular cross-section columns of mild steel conducted by von Karman supported the observations made by Considére. However, Shanley (1947) performed experiments on aluminium columns with different shapes and concluded that the results theoretically obtained by using the double modulus are different from those arrived at experimentally. He found that the theoretical values obtained by the tangent modulus theory were closer to the experimental values. He attributed this to differences in the stress-strain curves for mild steel and aluminium. However, he further observed that this is only valid if no strain reversal takes place. If strain reversal takes place the double modulus theory will give the correct result. The double modulus, E_r, will in general be larger than the tangent modulus, E_t, thus the stress according to the double modulus theory will be higher than the stress estimated by the tangent modulus theory. In Figure 6-5 the results from members collapsing in a global buckling mode in the quasi-static experiments have been compared with the Euler, tangent and double modulus theory.

6.1.2 Plate buckling

Many of the structural components used in an e.g. a spaceframe have a slender cross-section. If the wall thickness is small compared to the width, the extrusion walls will be sensitive to plate buckling. In the following sections, theories for elastic and plastic buckling of plates will be presented.

6.1.2.1 Elastic buckling of thin plates

If the local slenderness (width/thickness) ratio is small, the extrusion walls will collapse at a stress level that is lower than the yield stress, similar to the Euler buckling of axially loaded columns. To derive the equilibrium equation the following assumptions are made

i. The effect of shear strains on bending is negligible in a plate whose thickness is small compared to the lateral dimensions. (As a consequence, the lines normal to the middle surface before bending will remain straight and normal after bending.)

ii. The normal stress σ_z and the corresponding strain ε_z are negligible. (Therefore, the transverse deflection w at any point $w(x, y, z)$ is equal to the transverse deflection at the corresponding point $(x, y, 0)$ along the middle surface).

The differential equation for an initially plane plate subjected to in-plane uniaxial uniform compression $(-N_x)$ is given by

$$\nabla^4 w + \frac{N_x}{D} \frac{\partial^2 w}{\partial x^2} = 0 \qquad (6\text{-}24)$$

where the plate stiffness is given by

$$D = \frac{Eh^3}{12\left(1 - v^2\right)} \qquad (6\text{-}25)$$

E is the modulus of elasticity and h is the plate thickness. For a simply supported plate the following displacement function satisfies the boundary conditions and the differential equation given in Equation (6-24)

$$w(x,y) = w_{mn} \sin\frac{m\pi x}{a} \sin\frac{n\pi y}{b} \qquad (6\text{-}26)$$

where a and b are the plate length and width. Introducing the displacement function in the differential equation gives the following condition for elastic buckling

$$\left[\pi^4\left(\frac{m^2}{a^2}+\frac{n^2}{b^2}\right)^2 - \frac{N_x}{D}\left(\frac{m\pi}{a}\right)^2\right] w_{mn} \sin\frac{m\pi x}{a}\sin\frac{n\pi y}{b} = 0 \qquad (6\text{-}27)$$

The non trivial solution is given by

$$N_x = N_{xe} = \frac{\pi^2 D}{b^2}\left(m\frac{b}{a}+\frac{n^2}{m}\frac{a}{b}\right)^2 = k_\sigma\frac{\pi^2 D}{b^2} \qquad (6\text{-}28)$$

$$k_\sigma = \left(m\frac{b}{a}+\frac{n^2}{m}\frac{a}{b}\right)^2 \qquad (6\text{-}29)$$

$$\sigma_{cr,pl}^{el} = k_\sigma\frac{\pi^2 E}{12\left(1-v^2\right)}\left(\frac{h}{b}\right)^2 \qquad (6\text{-}30)$$

Minimization of k_σ with respect to m, n, a and b shows that k_σ is equal to 4 for $n=1$ and $m=a/b$ is an integer. When the aspect ratio (a/b) increases, the buckling load coefficient k_σ approaches four independent on the aspect ratio being an integer or not.

6.1.2.2 Stowell's theory

The elastic critical stress is only valid if the material response is elastic until buckling occurs. If strain hardening is neglected a plate is not capable of carrying a stress larger than the yield stress. Thus, as with the axial loaded columns, a transition curve is required.

For thick plates a plastic collapse will occur at a critical stress $\sigma_{cr,pl} < \sigma_{cr,pl}^{el}$. The Stowell theory is based on Shanley's approach for inelastic columns, where it is assumed that there is no strain reversal. In addition to the two assumptions made for the elastic buckling of a thin plate, the following three assumptions have been made

iii.   The plate material is continuous and isotropic.

iv.   The principal axes of plastic stress and strain coincide at all times.

v.   The volume of the material remains constant. This assumption requires that Poisson's ratio must increase from its elastic value of ca. 0.3 to the value of 0.5 for the plastic condition.

According to the Stowell theory the inelastic buckling stress of a plate can be expressed as

$$\sigma_{cr,pl}^{St} = \eta_S \sigma_{cr,pl}^{el} \tag{6-31}$$

where

$$\eta_s = \frac{E_s}{E}\left(0.5 + 0.25\sqrt{1 + \left(3\frac{E_t}{E_s} \right)} \right) \tag{6-32}$$

In the elastic region $E_t = E_s = E$ and the buckling stress according to Stowell theory is equal to the elastic buckling stress for a plate, if the Poisson's ratio $\nu = 0.3$.

Langseth and Hopperstad (1996) proposed a modification of the Stowell theory to take post-buckling strength into account. For a 6060-T6 alloy they found that a plate is fully effective for $\bar{\lambda} < 1.2$. As the sidewalls in the present extrusions have a reduced slenderness ratio in the range of $0.48 - 1.13$, post-buckling strength has not been considered when comparing the results with the Stowell theory.

In Figure 6-6 the results from members collapsing in a progressive buckling mode in the quasi-static experiments have been compared with elastic plate buckling theory and Stowell theory.

6.2   Comparison with analytical formulas and Eurocode 9

In this section the maximum force found in the quasi-static tests and the mean force from the quasi-static and dynamic tests have been compared with theoretical/empirical models and Eurocode 9 (2004).

6.2.1   Mean force and energy absorption

In order to compare the mean force and thus the energy absorption in members collapsing in progressive buckling mode the structural effectiveness η is defined by

$$\eta = P_m / A s_1 \tag{6-33}$$

where P_m is the mean axial crushing force taken at a crushing distance equal to δ in the quasi-static tests and w_b in the dynamic tests, A is the cross-sectional area and s_1 is a characteristic stress. If $s_1 = s_0$, where s_0 is the plastic flow stress for a perfect plastic material, the axial force required to cause uniform plastic deformation is then given by $A s_0$. The structural effectiveness $\eta = P_m / A s_0$ is then

a ratio between the mean crushing load and the squash load. To take into account the strain hardening of the material, s_1 is here defined as

$$s_1 = \frac{\int_0^{e_u} s(e)\, de}{e_u} \tag{6-34}$$

when using the engineering stress-strain curve. The strain e_u is taken at maximum engineering stress.

The solidity ratio ϕ is defined as (Jones, 1989)

$$\phi = A / A_c \tag{6-35}$$

where A_c is the area enclosed by the cross-section. For a thin-walled quadratic cross-section with constant wall thickness the solidity ratio is given by

$$\phi = 4bh / b^2 = 4h / b \tag{6-36}$$

For quasi-static progressive buckling of a square tubes, the relationship between η and ϕ, can be expressed as follows (Jones, 1989)

$$\eta = 1.3\phi^{2/3} \tag{6-37}$$

The relation between the structural effectiveness and solidity ratio given in Equation (6-37) is found from equating the internal energy consumed in one complete layer of lobes to the external work done by the mean axial crushing force. This expression is then minimized to give the mean axial crushing force (Jones, 1989). The structural effectiveness is then found using Equation (6-33).

Figure 6-2 shows the structural effectiveness vs. solidity ratio for the quasi-static tests. The structural effectiveness is an increasing function of the solidity ratio for

members collapsing in progressive buckling. As can be seen from Figure 6-2, good agreement was observed between the test results and the analytical prediction given by Equation (6-37) (Jones, 1989).

At 13 m/s the members experienced an increase in structural effectiveness in the range of 4-13 %, compared to the quasi-static tests, see Figure 6-2 and Figure 6-3a. The increase in structural effectiveness was increasing for decreasing solidity ratio, i.e. the most thin-walled members experienced a relatively larger increase in structural effectiveness than the members with high wall thickness. The strain rate sensitivity in aluminium is relatively small (Enjalbert, 2003) indicating that the increase in structural effectiveness is mainly due to inertia forces.

The members collapsing in the progressive buckling mode did not experience any increase in structural effectiveness when the impact velocity was increased from 13 m/s to 20 m/s, see Figure 6-3b.
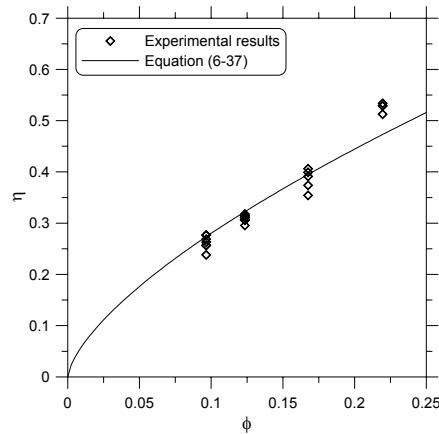
Figure 6-2. Quasi-static tests. Structural effectiveness vs. solidity ratio.

a) $v_0 = 13$ m/s   b) $v_0 = 20$ m/s
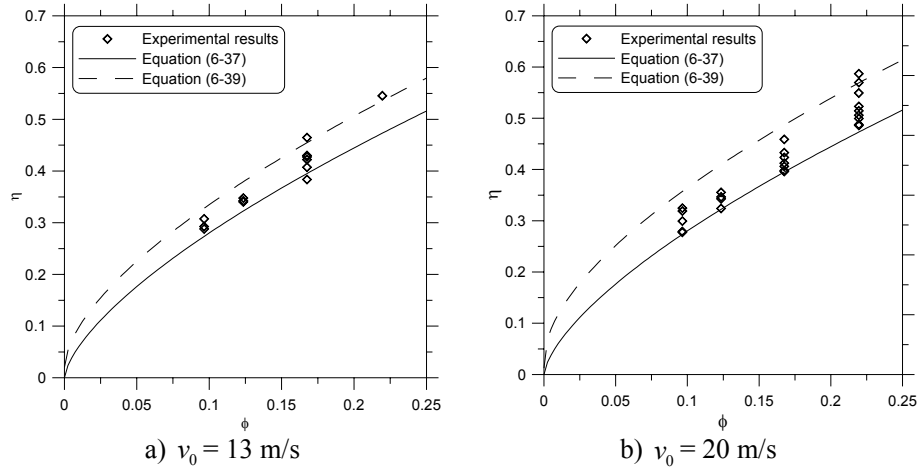
Figure 6-3 Impact tests. Structural effectiveness vs. solidity ratio.

The analytical formula given by Jones (1989), Equation (6-37), is only valid for quasi-static progressive buckling. There is, however, a modified version where strain rate effects but not inertia effects are taken into account (Jones, 1989). Hanssen et al. (2000), however, suggested the following expression for the mean force which takes into account the impact velocity v_0 and thus the inertia forces set up in the profile during axial crushing

$$F_{avg}^0 = 13.06\sigma_0 b_m^{1/3} h^{5/3} \left\{ 1 + C_{ine} \left[\frac{b_m}{h} \frac{\rho_0}{\sigma_0} v_0^2 \right]^{1/2} \right\} \tag{6-38}$$

Here C_{ine} is an experimentally determined dynamic amplification factor and ρ_0 is the density of the extrusion material. By introducing the expressions for the solidity ratio and the structural effectiveness, Equation (6-38) can be rewritten as

$$\eta = 1.3\phi^{2/3} \left\{ 1 + C_{ine} \left[\frac{4}{\phi} \frac{\rho_0}{\sigma_0} v_0^2 \right]^{1/2} \right\} \tag{6-39}$$

According to Hanssen et al. (2000) the factor C_{ine} is equal to 0.66 for extrusions collapsing with 4 or more lobes.

Figure 6-3 shows as expected that the analytical formula given by Jones (1989) somewhat underestimates the structural effectiveness for members collapsing by progressive buckling at an impact velocity of 13 m/s. The structural effectiveness for members with wall thicknesses of 2.0 mm ($\phi = 0.097$), 2.5 mm ($\phi = 0.12$), and 3.5 mm ($\phi = 0.17$) is somewhat overestimated when using the expression given in Equation (6-39), while a very good estimate of the structural effectiveness is found for members with wall thickness of 4.5 mm ($\phi = 0.22$).

Figure 6-4 considers each wall thickness and shows the ratio between the energy absorbed at transition (E_T) and the corresponding energy at bottoming out (E_P) as a function of the corresponding displacement ratio ($w_T/0.73L$).

As expected the energy and displacement ratio are related by a straight line where $E_T/E_P = P_m^*/P_m = w_T/0.73L$. P_m^* is defined in Chapter 4. The main conclusion that can be drawn from Figure 6-4 is that for members collapsing in a transition between progressive and global buckling the energy absorption is very dependent on the time of the transition. If the transition occurs at a late stage, the energy absorption will be almost as high as for the members collapsing in a progressive buckling mode. Further, the figure shows that the deformation at transition is increased when increasing the impact velocity due to inertia forces. This prevents the early transition from progressive to global buckling. As a reference, the energy ratios for members collapsing in global buckling mode have been plotted in Figure 6-4. As can be seen, there is a significant reduction in energy absorption when global buckling occurs.
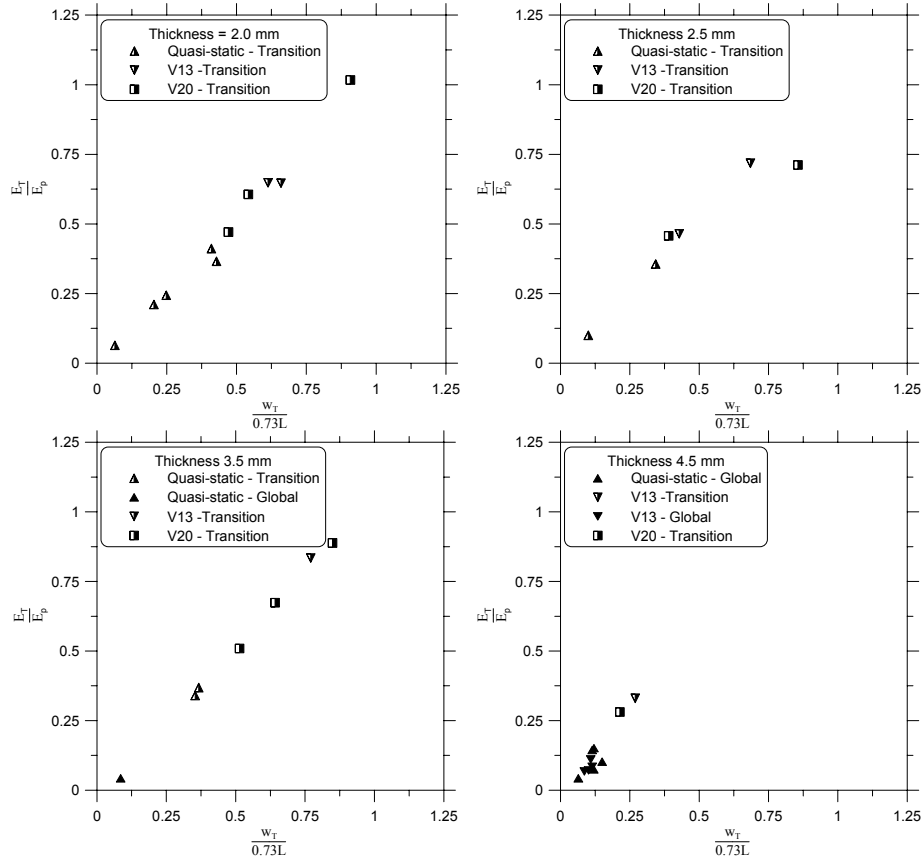
Figure 6-4 Relative energy absorption vs. "time" of transition.

6.2.2   Buckling of columns

The peak force of the members collapsing in a direct global mode in the quasi-static tests is now compared with analytical formulas and Eurocode 9. The relation between the dimensionless Euler critical stress and the reduced slenderness can be expressed as (cf. Section 6.1.1.1)

$$\frac{\sigma_{cr}^{E}}{\sigma_{0.2}} = \frac{1}{\overline{\lambda}_{k}^{2}}$$

(6-40)

From Section 6.1.1.2 and Equation (6-3) the buckling stress according to the tangent modulus theory is given by (Gaylord jr and Gaylord, 1972)

$$\frac{\sigma_{cr}^{pl,t}}{\sigma_{0.2}} = \frac{E_t}{E} \frac{1}{\overline{\lambda}_k^2}$$

(6-41)

According to the double modulus theory, see Section 6.1.1.3 and Equation (6-10), the dimensionless buckling stress is given by

$$\frac{\sigma_{cr}^{pl,d}}{\sigma_{0.2}} = \frac{E_r}{E} \frac{1}{\overline{\lambda}_k^2}$$

(6-42)

where the double modulus E_r is given by Equation (6-9). The tangent modulus is calculated from the parameterized stress-strain curve given by Equation (2-4). In the calculation of E_t the results from tensile tests in the 0° direction for test specimens with wall thickness 3.5 mm were used.

In Equations (6-40), (6-41) and (6-42), no effect of initial geometrical imperfections and residual stresses are taken into account. However, measurements have shown that the geometrical imperfections and residual stresses in extrusions are small (Mazzolani, 1985). Thus, Equations (6-40), (6-41) and (6-42) may give good estimates of the global buckling resistance of extruded members in aluminium.

Eurocode 9 (EC9) "Design of aluminium structures" (2004) gives design rules for the ultimate resistance of members and plated structures. For axially loaded tubes the design buckling resistance is given as

$$N_{b,Rd} = \kappa \chi A_{eff} f_0 / \gamma_{m1}$$

(6-43)

Here, χ is the reduction factor for flexural buckling, A_{eff} is the effective area allowing local buckling of class 4 elements, κ is a reduction factor that accounts

for the weakening effects due to welding and f_0 is the characteristic stress equal to $\sigma_{0.2}$. For unwelded sections κ is equal to 1.0. The reduction factor χ is a function of the non-dimensional slenderness, i.e.

$$\chi = \frac{1}{\varphi + \sqrt{\varphi^2 - \overline{\lambda}_k^2}} \tag{6-44}$$

$$\varphi = 0.5\left[1 + \alpha\left(\overline{\lambda}_k - \overline{\lambda}_0\right) + \overline{\lambda}_k^2\right] \tag{6-45}$$

Here, α is an imperfection factor for heat-treated members and $\overline{\lambda}_0$ is the limit of the horizontal plateau (i.e. $\chi < 1$ for $\overline{\lambda}_k > \overline{\lambda}_0$) (Eurocode 9, 2004). For the actual case $\alpha = 0.2$ and $\overline{\lambda}_0 = 0.1$.

In the quasi-static tests the lower end of the member is clamped while the upper end is prevented from sideways movement by friction between the member and the rigid steel plate used to apply the load. Rotation of the upper end is negligible until buckling occurs. Thus, the specimens have been considered as clamped at both ends when the buckling length was estimated ($L_k = 0.5L$).

In Figure 6-5 the results from the quasi-static tests have been compared with the tangent and double modulus theories and Eurocode 9 when $\gamma_{m1} = 1.0$. The results from the quasi-static tests are a little higher than the values given by the tangent and double modulus theories. As expected, the design code gives conservative estimates of the buckling strength. All the quasi-static tests are well within the plastic region.

As can be seen from the Figure 6-5, the agreement between the test results and the analytical formulas is very good. The design code gives conservative values for the buckling stress.
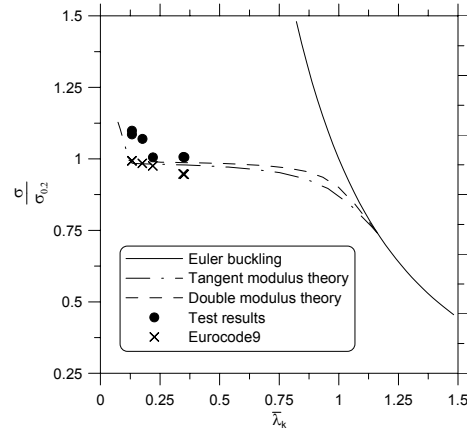
Figure 6-5 Quasi-static tests. Column buckling stress vs. slenderness.

6.2.3 Local buckling

The peak force of the members collapsing in a progressive buckling mode and in transition from progressive to global buckling is compared with analytical formulas in the following. Due to the axisymmetric folding mode, the sidewalls of the extrusions have been modelled as long imperfection-free, simply-supported plates. Li and Reid (1990) investigated the buckling behaviour of axially loaded square tubes by taking the realistic edge conditions into account. Based on their calculations the tubes in the present study will have a buckling factor k_σ in the range $3.85 - 4$ with the lowest value occurring for $h = 4.5$ mm. However, for design purposes it is convenient to use $k_\sigma = 4$, which will be used in the following. The elastic buckling stress of a plate is as previously shown given by (cf. Section 6.1.2.1)

$$\sigma_{cr,pl}^{el} = k_\sigma \frac{\pi^2 E}{12(1-v^2)} \left(\frac{h}{b_m} \right)^2 \tag{6-46}$$

where $b_m = b - h$. The reduced slenderness ratio for the plate is given by (Langseth and Hopperstad, 1996)

$$\bar{\lambda}_p = 1.04 \frac{b_m}{h} \frac{1}{\sqrt{k_\sigma}} \sqrt{\frac{\sigma_{0.2}}{E}} = \frac{1}{1.92} \frac{b_m}{h} \sqrt{\frac{\sigma_{0.2}}{E}} \qquad (6\text{-}47)$$

Stowell's classical formula has been used to calculate the critical stress (cf. Section 6.1.2.2), i.e.

$$\sigma_{cr,pl}^{St} = \eta_s \sigma_{cr,pl}^{el} \qquad (6\text{-}48)$$

$$\eta_s = \frac{E_s}{E} \left(0.5 + 0.25 \sqrt{1 + \left(3 \frac{E_t}{E_s} \right)} \right) \qquad (6\text{-}49)$$

where E_s is the secant modulus.

The local buckling resistance of the cross-section according to Eurocode 9 (2004) is given by

$$N_{b,Rd} = A_e \cdot f_0 / \gamma_{m1} \qquad (6\text{-}50)$$

$$A_e = 4(b - h) h_{eff} \qquad (6\text{-}51)$$

$$h_{eff} = h \cdot \rho_c \qquad (6\text{-}52)$$

where the effective cross-sectional area, A_e, accounts for the reduced thickness, h_{eff}, of class 4 elements. ρ_c is a local buckling coefficient used to factor down the thickness of all class 4 elements that are wholly or partly in compression.

In Figure 6-6 the results from the quasi-static tests have been compared with elastic plate buckling theory, Stowell theory and Eurocode 9.
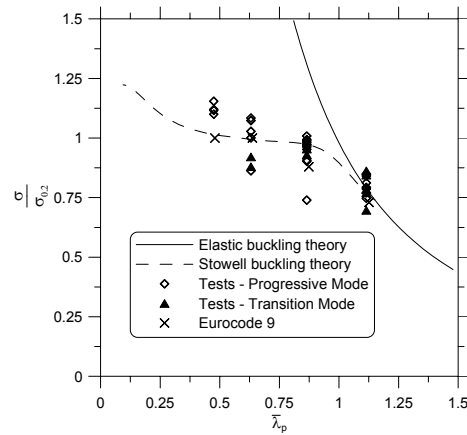
Figure 6-6 Quasi-static tests. Local buckling stress vs. slenderness.

As can be seen from Figure 6-6, the quasi-static test results are scattered around the predictions using the Stowell theory. However, the variation in critical stress for the quasi-static tests is relatively large, which implies that the estimated capacity after Eurocode 9 gives non-conservative results for some of the tested components. The reason for this variation is not clear and further studies are required.

6.3   Analytical models for predicting the collapse mode

The energy absorption is extremely dependent on the collapse mode, thus it is important to be able to predict the mode of deformation of axially loaded thin-walled extrusions. In this section analytical models used to predict the collapse mode will be presented.

Ideally an analytical model should be able to deal with both quasi-static and dynamic loading. However, the response of dynamically loaded extrusions is very complicated. A fundamental change in response was observed in the dynamic tests compared to the quasi-static tests. The change in response is related to inertia caused by global and local buckling of the members. Due to this complex response, the dynamic case was omitted in this study.

6.3.1 Progressive and global buckling

A simplified model was first presented by Abramowicz and Jones (1997). This model considers progressive and direct global buckling. The model is valid for axially loaded thin-walled extrusions collapsing in both the elastic and plastic region.

It is assumed that progressive buckling is initiated by plate buckling in the extrusion walls and global buckling is initiated by column buckling. For a given local slenderness of the plate elements a progressive buckling load can be calculated. As long as this load is smaller than the global buckling load, progressive buckling will occur. When the global slenderness is increased, the global buckling load will decrease, and global buckling will occur when the global slenderness reaches a critical value. Thus, for a given local slenderness a corresponding critical global slenderness can be found, see Figure 6-7.

If the plate and column buckling loads are the same for a column with a given cross-section, an increase in length will lead to global buckling.
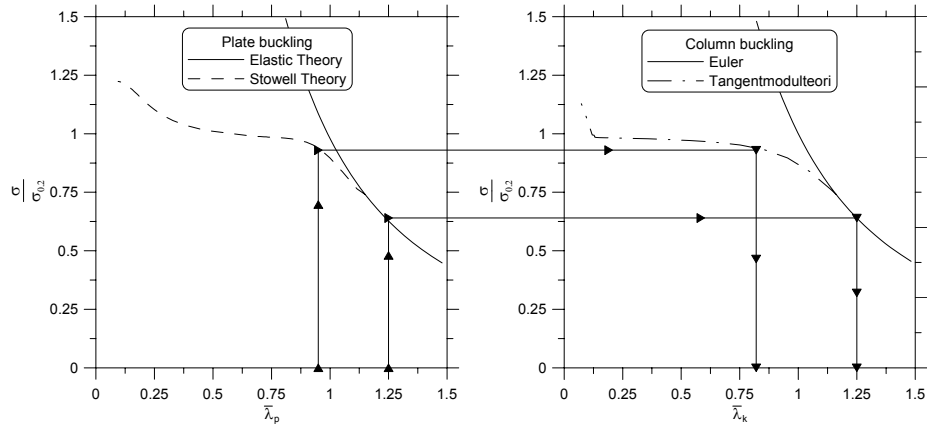
Figure 6-7 Plate and column buckling loads.

Abramowicz and Jones (1997) considered a simple supported column. The columns in this study, however, were assumed to be clamped at both ends, thus the calculations by Abramowicz and Jones (1997) were adjusted to allow for these boundary conditions.

6.3.1.1 Transition between local and global buckling in the elastic range

In the following a distinction is made between elastic plate buckling $\sigma_{cr,pl}^{el}$ and Euler, or column buckling, σ_{cr}^{E}. The elementary theoretical condition that separates the two regions is given by

$$\sigma_{cr,pl}^{el} = \sigma_{cr}^{E} \qquad (6\text{-}53)$$

Provided that the interaction between local and global buckling is neglected, the stress when global buckling takes place for a perfect column fully clamped at both ends is given by

$$\sigma_{cr}^{E} = \frac{4\pi^2 EI}{AL^2} \qquad (6\text{-}54)$$

When assuming $b \gg h$, the cross-sectional area and second moment of area can be written as

$$A \approx 4bh \qquad (6\text{-}55)$$

$$I \approx \frac{2}{3}b^3 h \qquad (6\text{-}56)$$

As shown in Section 6.1.2.1, the buckling stress for a thin, imperfection-free, simply supported, square, elastic plate can be written as

$$\sigma_{cr,pl}^{el} = \frac{4\pi^2 E}{12(1-\nu^2)}\left(\frac{h}{b}\right)^2 \qquad (6\text{-}57)$$

Introducing Equations (6-54), (6-55), (6-56) and (6-57) into Equation (6-53), the critical global slenderness ratio as a function of the local slenderness ratio can be written as

$$\left(\frac{L}{b}\right)_{cr} = \sqrt{2\left(1 - v^2\right)}\left(\frac{b}{h}\right)$$

(6-58)

For most metals, including aluminium the Poisson's ratio v is equal to 0.3 giving the following linear relation for the critical global slenderness in the elastic range

$$\left(\frac{L}{b}\right)_{cr} \approx 1.35\left(\frac{b}{h}\right)$$

(6-59)

i.e. the critical global slenderness is a linear function of the local slenderness.

6.3.1.2 Transition between local and global buckling in the plastic range

In the plastic range, the theoretical condition that separates local and global buckling is

$$\sigma_{cr,pl}^{pl} = \sigma_{cr}^{pl}$$

(6-60)

Using the tangent modulus theory, the critical plastic buckling stress of a perfect column, fully clamped at both ends, is as shown in Section 6.1.1.2 and given by

$$\sigma_{cr}^{pl} = \frac{4\pi^2 E_t I}{AL^2}$$

(6-61)

The critical plastic buckling stress for an imperfection-free, simply supported plate is given by (Abramowicz and Jones, 1997)

$$\sigma_{cr,pl}^{pl} = \frac{\pi^2}{9}E_s\left[2 + \sqrt{1 + 3\frac{E_t}{E_s}}\right]\left(\frac{h}{b}\right)^2$$

(6-62)

Solving Equation (6-60) for the critical global slenderness using Equations (6-61) and (6-62), the following relation is obtained

$$\left(\frac{L}{b}\right)_{cr} = \sqrt{\frac{6E_t / E_s}{2 + \sqrt{1 + 3E_t / E_s}}} \left(\frac{b}{h}\right)$$

(6-63)

The stress-strain behaviour of the column material can be expressed using a power-type stress-strain relation

$$\sigma = \sigma_y \left(\frac{\varepsilon}{\varepsilon_0}\right)^n , \varepsilon \geq \varepsilon_0$$

(6-64)

Using Equation (6-64) the tangent modulus, the secant modulus and the ratio between the tangent and secant modulus can be expressed as follows

$$E_t = \frac{n\sigma_y}{\varepsilon_0} \left(\frac{\varepsilon}{\varepsilon_0}\right)^{n-1}$$

(6-65)

$$E_s = \frac{\sigma_y}{\varepsilon_0} \left(\frac{\varepsilon}{\varepsilon_0}\right)^{n-1}$$

(6-66)

$$\frac{E_t}{E_s} = n$$

(6-67)

The critical global slenderness can now be expressed as

$$\left(\frac{L}{b}\right)_{cr} = \sqrt{\frac{6n}{2 + \sqrt{1 + 3n}}} \left(\frac{b}{h}\right)$$

(6-68)

Equation (6-68) indicates that the response is very dependent on the hardening parameter n. Figure 6-8 shows the variation of the slope of Equation (6-68) as a function of the hardening parameter n.
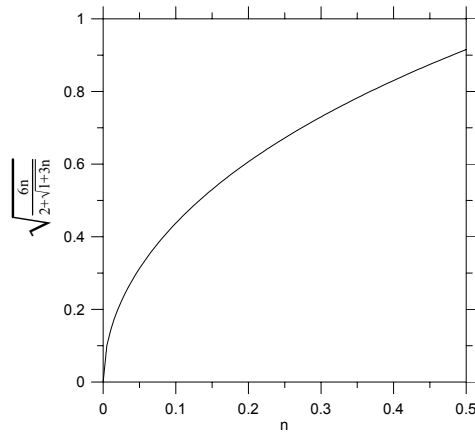
Figure 6-8 Influence from the hardening parameter n.

The power-type stress-strain relation is not able to give an accurate description of both the small and large strain part of the stress-strain curve of a typical T6 material. Since buckling occurs at relatively low levels of plastic strains, the material hardening parameter is determined for corresponding strain levels. Based on the material tests presented in Section 2, a hardening parameter n equal to 0.043 was chosen, which will give the following relation between the critical global slenderness and local slenderness

$$\left(\frac{L}{b}\right)_{cr} = 0.29\left(\frac{b}{h}\right)$$
(6-69)

As in the elastic region, a linear relation is observed between the critical global slenderness and the local slenderness but the slope is significantly lower, especially for materials with little strain hardening.

6.3.1.3 Limits of the elastic and plastic region

The critical aspect ratio, b/h, that separates the elastic and plastic response of the plate can be obtained from

$$\sigma_{cr,pl}^{el} = \sigma_y \tag{6-70}$$

where $\sigma_{cr,pl}^{el}$ is given by Equation (6-57). Here the yield stress, σ_y, is taken as the $\sigma_{0.2}$ proof stress. The critical aspect ratio is given by

$$\left(\frac{b}{h}\right)_{cr} = \sqrt{\frac{\pi^2}{3(1-\nu^2)}}\sqrt{\frac{E}{\sigma_y}} \tag{6-71}$$

Introducing E = 70 000 N/mm², ν = 0.3 and $\sigma_{0.2}$ = 200 MPa (typical values for aluminium alloy 6060-T6), Equation (6-71) reads

$$\left(\frac{b}{h}\right)_{cr} = 35.55 \tag{6-72}$$

The Euler formula for elastic buckling is assumed valid until the axial compressive force, P, reaches the squash load $P = \sigma_y A$. Thus the critical aspect ratio $\left(L/b\right)_{cr}$, separating the elastic and plastic global buckling regions, is given by

$$\left(\frac{L}{b}\right)_{cr} = \sqrt{\frac{2}{3}\pi^2 \frac{E}{\sigma_y}} \tag{6-73}$$

$$\left(\frac{L}{b}\right)_{cr} \approx 48 \tag{6-74}$$

6.3.1.4 Summary

The result from Equations (6-59), (6-69), (6-72) and (6-74) are summarized in Figure 6-9. The plot shows what type of response is expected for different combinations of local and global slenderness.
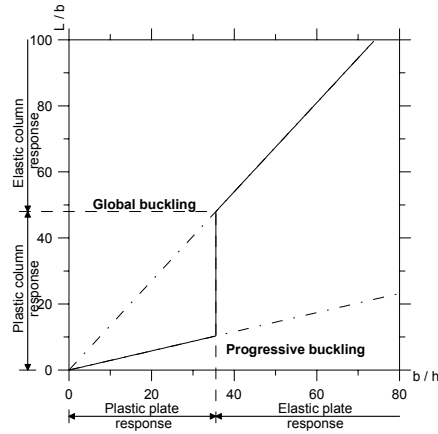
Figure 6-9 Areas with global and local elastic and plastic buckling.

In Section 6.3.1.6 the analytical model will be compared with the experimental results.

6.3.1.5 Modification of the model proposed by Abramowicz and Jones

In the model proposed by Abramowicz and Jones (1997) there is a leap in critical global slenderness when going from the plastic to the elastic region. This is due to the characteristics of the chosen material model. Abramowicz and Jones (1997) used a power type stress-strain relation, see Equation (6-64), in which $d\sigma/d\varepsilon$ is a discontinuous function when going from elastic to the plastic material behaviour. In this section the Ramberg-Osgood strain hardening model given by

$$\varepsilon = \frac{\sigma}{E} + \varepsilon_0 \left(\frac{\sigma}{\sigma_{0.2}} \right)^m \tag{6-75}$$

will be used. The hardening is roughly the same for both models if the hardening parameters are related by

$$m = \frac{1}{n} \tag{6-76}$$

Tangent modulus theory and Stowell theory are used for column buckling and plate buckling respectively. If buckling occurs in the elastic range, the buckling stress according to the tangent modulus theory will be the same as the buckling stress according to Euler theory. The same applies to the Stowell and elastic plate buckling theory if Poisson's ratio $v = 0.3$.

Using Equations (6-30), (6-31) and (6-32) the local slenderness can be expressed as

$$\left(\frac{b}{h}\right) = \sqrt{\eta_S \frac{\pi^2 E}{3\sigma\left(1-v^2\right)}} \qquad (6\text{-}77)$$

where η_S is given by Equation (6-32). Using the tangent modulus theory for the global buckling of the fully clamped column, the slenderness of the column can be expressed as follows

$$\lambda = \sqrt{\frac{4\pi^2 E_t}{\sigma}} \qquad (6\text{-}78)$$

Assuming thin-walled cross-sections and disregarding second and higher order thickness contributions, the length width ratio can be written as

$$\frac{L}{b} = \frac{\lambda}{\sqrt{6}} \qquad (6\text{-}79)$$

When using the Ramberg-Osgood strain hardening model, it is not possible to find a closed form solution like the one found by Abramowicz and Jones (1997) in the previous section.

For a given stress, the tangent and secant moduli can be calculated from Equation (6-75) Subsequently Equations (6-77), (6-78) and (6-79) can be used to calculate local and global slenderness pairs where transition from progressive to global

buckling will occur. The calculated critical global slenderness is plotted in Figure 6-10.

As can be seen from the figure the modified Abramowicz and Jones model gives a smother transition from the elastic to plastic range.

6.3.1.6 Comparison with experimental results.

In Figure 6-11 the analytical models are compared with the experimental results. Only the experimental results for thicknesses where the column collapsed in progressive or global mode are included. Thus, the results for columns with wall thicknesses 2.0 mm and 2.5 mm are omitted, as these columns collapsed in either a progressive mode or a transition mode.

The model presented by Abramowitz and Jones (1997) gives conservative estimates of the critical global buckling length. However, when the local slenderness is increased the model be very conservative. The modified model, however, is non conservative for the lowest local slenderness, but seems to capture the physical behaviour better than the Abramowitz and Jones model.
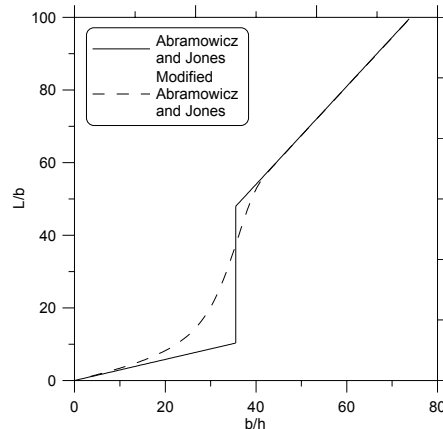
Figure 6-10 Modified Abramowicz and Jones.
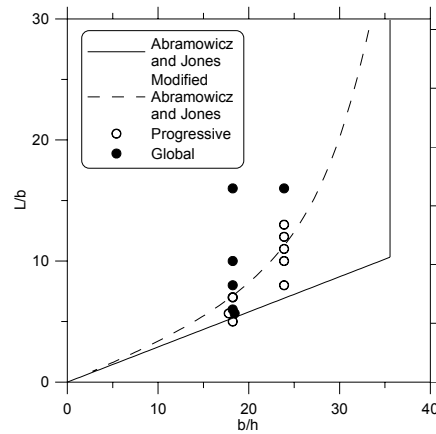
Figure 6-11 Comparison of experimental results and analytical model.

6.3.2 An analytical approach to the transition from progressive to global buckling of thin-walled columns.

In the previous model it is assumed that if a member starts with progressive buckling, it will continue with progressive buckling and no transition to global buckling will occur. The experimental tests, however, showed that this assumption is only correct for the most thick-walled members subjected to quasi-static loading.

In this section a simplified analytical model for predicting the transition from progressive to global buckling will be presented. Focus is placed on describing the effects, not on giving an accurate quantitative estimate of the critical global slenderness where a transition from progressive to global buckling occurs.

Figure 6-12a shows a column subjected to an axial load N_m. It is assumed that the column will start to collapse progressively and any transition to global buckling will take place after some axial deformation.
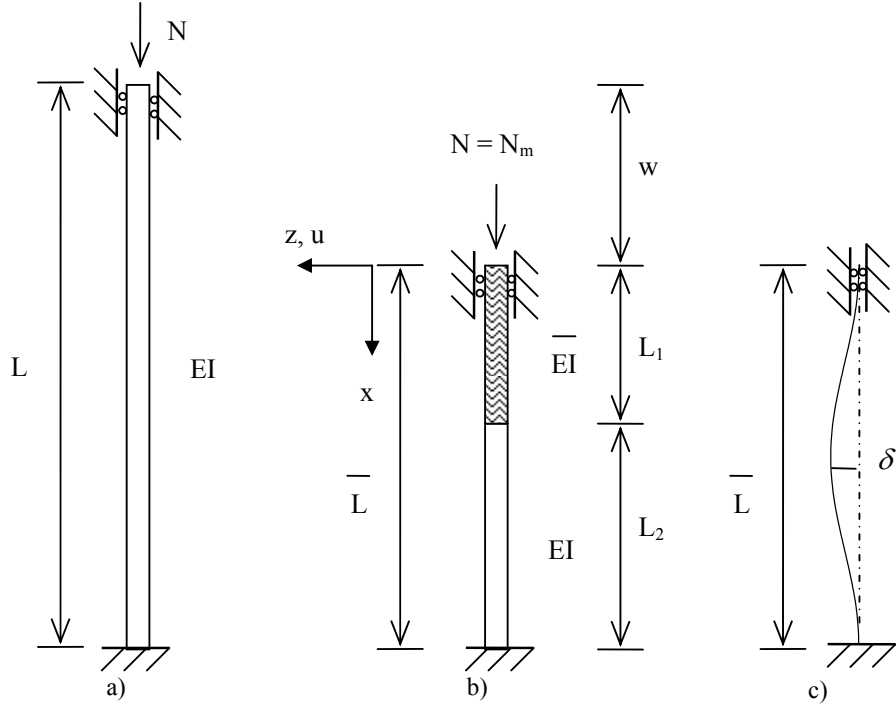
Figure 6-12 Column under axial loading.

A bottoming out length of $0.27L$ is used in the following, which gives a deformation, w, at bottoming out of $0.73L$. For an axially loaded column collapsing progressively the following kinematic relations can be established, see Figure 6-12b:

$$w = 0.73\left(w + L_1\right) \tag{6-80}$$

$$L_1 = \frac{0.27}{0.73}w = 0.37w \tag{6-81}$$

$$L_2 = L - \left(L_1 + w\right) = L - \left(0.37w + w\right) = L - 1.37w \tag{6-82}$$

$$\overline{L} = L_1 + L_2 = L - w \tag{6-83}$$

Here, w is the deformation, L is the initial length, L_1 is the length of the progressively deformed part of the column, L_2 is the length of the un-deformed part and $\overline{L}$ is the total length.

Assuming the column is clamped at both ends, the lateral deflection can be approximated by

$$u = \delta \left(\frac{1}{2} - \frac{1}{2} \cos \left(2\pi x \Big/ \overline{L} \right) \right)$$ (6-84)

Furthermore, it is assumed that the compressed part has a bending stiffness $\overline{EI}$, which for simplicity is assumed not to be influenced by the axial load.

6.3.2.1 *Behaviour of partly compressed column*

The global buckling load of a column with varying bending stiffness will now be calculated. It is assumed that the column in Figure 6-12b has a bending stiffness $\overline{EI}$ in the upper part $\left(0 < x < L_1\right)$ and EI in the lower part $\left(L_1 < x < \overline{L}\right)$ and total deflections, see Figure 6-12c, given by Equation (6-84).

Neglecting the energy due to axial strains the internal elastic energy of the deflected column can be expressed as

$$U = \frac{1}{2} \int_0^{L_1} \overline{EI} \cdot u_{,xx}^2 \, dx + \frac{1}{2} \int_{L_1}^{\overline{L}} EI \cdot u_{,xx}^2 \, dx$$ (6-85)

Introducing Equation (6-84) gives

$$U = \frac{\pi^4}{\overline{L}^3} \delta^2 EI^*$$ (6-86)

Here EI^* is defined as

$$EI^* = \overline{EI}\left(\frac{1}{4\pi}\sin\left(\frac{4\pi L_1}{\overline{L}}\right) + \frac{L_1}{\overline{L}}\right) + EI\left(1 - \frac{1}{4\pi}\sin\left(\frac{4\pi L_1}{\overline{L}}\right) - \frac{L_1}{\overline{L}}\right) \qquad (6\text{-}87)$$

The potential of the external axial load, N, reads

$$H = -N\Delta = -\frac{N}{2}\int_0^{\overline{L}}\left(u_{,x}^2\right)dx \qquad (6\text{-}88)$$

$$H = -\frac{N\pi^2}{4\overline{L}}\delta^2 \qquad (6\text{-}89)$$

For equilibrium

$$\delta(U + H) = 0 \qquad (6\text{-}90)$$

$$\frac{\pi^4}{\overline{L}^3}4\delta EI^* = \frac{N\pi^2}{\overline{L}}\delta \qquad (6\text{-}91)$$

$$N_{cr} = \frac{4\pi^2 EI^*}{\overline{L}^2} \qquad (6\text{-}92)$$

For an un-deformed and fully compressed column, respectively, the total length, bending stiffness and critical load are given by

$$\left.\begin{array}{l} L_1 = w = 0 \\ \overline{L} = L_2 = L \end{array}\right\} \Rightarrow EI^* = EI, N_{cr} = \frac{4\pi^2 EI}{L^2} \qquad (6\text{-}93)$$

$$L = \overline{L}_1 \Rightarrow EI^* = \overline{EI}, N_{cr} = \frac{4\pi^2 \overline{EI}}{\overline{L}^2} \qquad (6\text{-}94)$$

As can be seen from Equation (6-93), the critical load is correctly estimated compared to the value given by Bergan and Syvertsen (1977). This is because the energy method will give correct values when the correct deflection is assumed. Using the same procedure the buckling load for a partly compressed column clamped at one end and free to rotate at the other and for a simply supported column can be calculated.

6.3.2.2 Bending stiffness of crushed column

In order to calculate the critical load given by Equation (6-92) it is necessary to find an expression for the bending stiffness, $\overline{EI}$, of the deformed part of the column. Several different possibilities exist for determining this bending stiffness, i.e. experimentally/numerically by doing bending tests on a column that has collapsed progressively, or analytically by considering the shape of the deformed cross-section. The analytical approach is very complicated since the cross-section is changing along the length of the deformed column. Thus it was chosen to determine the bending stiffness of the progressively deformed part of the column using numerical simulations.

Accordingly, numerical simulations of thin-walled extrusions collapsing progressively were carried out. Four different thicknesses with initial length 640 mm were investigated. The deformed geometries were used in series of new simulations. In one series with wall thickness 2.0 mm, different axial force levels were applied together with end rotation, see Figure 6-13.
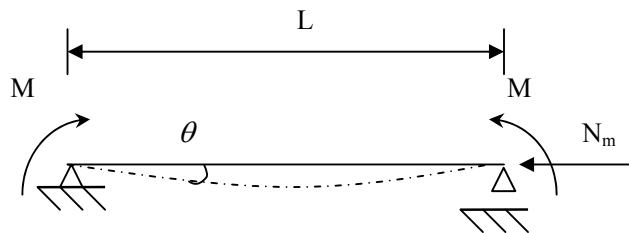
Figure 6-13 Rotation of deformed coumn.

These simulations were performed to check if the bending stiffness was influenced by the axial load level. In the analytical model the partly compressed column is assumed to deform progressively subjected to a constant axial load equal to N_m. Thus the bending stiffness of the compressed part of the column subjected to a constant axial load had to be established. The numerical simulations showed, however, that the bending stiffness was not influenced by the axial load, see Figure 6-14a. Thus in the second series of simulations with wall thickness 2.5 mm, 3.5 mm and 4.5 mm the axial force was kept equal to N_m, where N_m is the mean force level when the column collapses progressively.

In Figure 6-14 moment-rotation curves for compressed columns with different thicknesses are presented. The moment-rotation relation for simply supported columns with concentrated end moment at both ends are given by

$$M = \frac{2\overline{EI}}{L}\theta \tag{6-95}$$

Using Equation (6-95) the bending stiffness of the progressively deformed column can be found as a function of the thickness. A validation test on an undeformed column was performed to check the validity of the simulations. A very good agreement was found between the bending stiffness found analytically and from Equation (6-95). Based on the numerical simulations the reduction in bending stiffness can be expressed as

$$\overline{EI} = k_{EI}EI \tag{6-96}$$

where k_{EI} is a reduction factor that is dependent on the wall-thickness in the extrusions. The calculated reduction factor for the different thicknesses is presented in Table 6-1
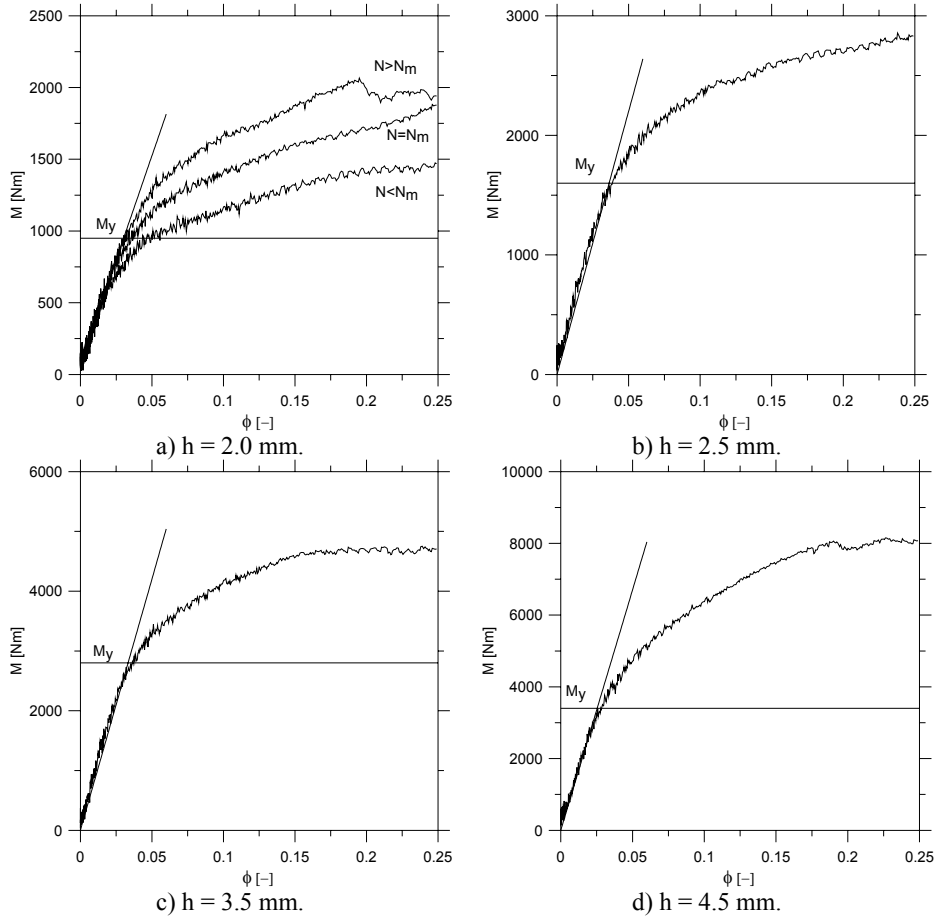
Figure 6-14 Moment-rotation relation for compressed columns with different thickness.

Table 6-1 Bending stiffness of deformed column.

h	2.0 mm	2.5 mm	3.5 mm	4.5 mm
EI [Nm^2]	44313	54349	73240	90623
$\overline{EI}$ [Nm^2]	2030	3080	5880	9380
k_{EI} [-]	0.0458	0.0567	0.0803	0.1035

Based on the results from the numerical simulations presented in Table 6-1 it was found that k_{EI} is proportional to the thickness. Using the method of least squares the following expression was found for the reduction factor k_{EI}

$$k_{EI} = 0.023 \cdot h \cdot \frac{1}{mm} - 0.0002 \approx 0.023 \cdot h \cdot \frac{1}{mm} \qquad (6\text{-}97)$$

where h is the thickness in mm.

6.3.2.3 Procedure for calculation of the critical length

A similar procedure as the one used in Section 6.3.1 is adopted to calculate the critical global slenderness where a transition from progressive buckling to global buckling occurs. However, in this model progressive buckling is not governed by plate buckling in the extrusion walls. A column collapsing progressively will deform with a force-deformation history similar to the one given in Figure 4-1b. As can be seen from the figure the force level oscillates around a mean force level. However, for simplicity it is assumed that the column will collapse progressively at a constant force level N_m given by

$$\sigma_{prog.} = \frac{N_m}{A} = \frac{13.06 s_1 \left(b/h \right)^{1/3} h^2}{4bh} \qquad (6\text{-}98)$$

where s_1 is given by Equation (6-34). In these analyses the column is assumed to be clamped at both ends. This gives a buckling length of $0.5\overline{L}$ thus the critical global buckling stress for the partly compressed column is found from Equation (6-92) and given by

$$\sigma_{global} = \frac{N_{cr}}{A} = \frac{4\pi^2 EI^*}{\overline{L}^2 \, 4bh} \qquad (6\text{-}99)$$

It is assumed that the column will start to buckle progressively and continue to do so if the progressive stress level given by Equation (6-98) is less than the stress level required for global buckling given by Equation (6-99).

The following procedure is used for calculating the critical global slenderness as a function of the local slenderness. For a given local slenderness the stress required for progressive buckling is calculated using Equation (6-98). Using the same width and thickness the global buckling stress is calculated as follows. A relatively short initial length is chosen, the column is given a small deformation and the buckling stress according to Equation (6-99) is calculated. If the column buckling stress is larger than the progressive buckling stress the column will collapse progressively, the deformation is increased successively until a transition to global buckling occurs or the column is fully compressed. If the column is compressed completely and no transition to global buckling occurred, the initial length will be increased and the procedure of increasing the deformation is repeated. The initial length is increased until a transition from progressive to global buckling occurs. When the critical global slenderness is found the local slenderness is increased and the procedure is repeated.

6.3.2.4 *Comparison with experimental results.*

In Figure 6-15 the results from the quasi-static tests are compared to the analytical model. The critical buckling length for columns with three different boundary conditions is presented in the figure.

As can be seen from the figure the critical buckling lengths estimated by the analytical model significantly overestimates the critical buckling length found in the experimental tests. In the analytical model the progressive buckling is assumed not to introduce any obliqueness or load eccentricity to the partly compressed column. In the experimental tests, however, it was observed that the new lobes sometimes formed "off-centre". This will introduce imperfections and load eccentricity, which will decrease the stability of the partly compressed column. In addition, the column is assumed to collapse progressively at a constant force level equal to the mean force given by Equation (6-98). However, as can be seen from Figure 4-1 the force level oscillates as the column collapses progressively.
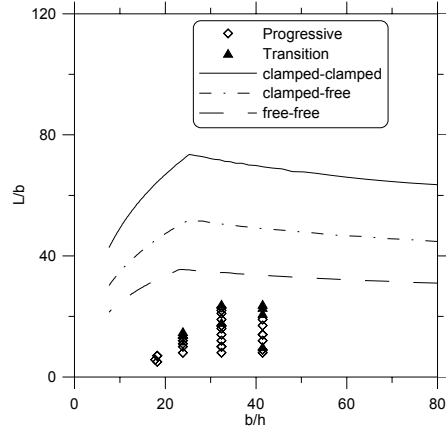
Figure 6-15 Comparison between experimental results and analytical model

6.3.3 Alternative approach to the transition from progressive to global buckling

In this section an alternative approach to the transition from progressive to global buckling will be presented. In Section 6.3.2 the column is assumed to be perfectly straight. In the model that will be presented in this section initial imperfections are included. In the experimental tests it was observed that the lobes in some tests formed "of-centre", an attempt to include this is done by letting the imperfections increase with the deformation of the column.

For simplicity an axially loaded simple supported partly compressed column with initial imperfections given by Equation (6-11) will be considered. The total deflection can be expressed as (cf. Section 6.1.1.4)

$$\delta = \frac{\delta_0}{1 - N/N_E} \tag{6-100}$$

Here N_E is the Euler buckling load for a partly compressed column given by

$$N_{cr} = \frac{\pi^2 EI^*}{\bar{L}^2} \tag{6-101}$$

where $\bar{L}$ is the total length of the partly compressed column defined by Equation (6-83). EI^* for a simply supported column can be calculated using the same procedure as in Section 6.3.2.1

$$EI^* = \overline{EI} \left(\frac{L_1}{\bar{L}} - \frac{1}{2\pi} \sin\left(\frac{2\pi L_1}{\bar{L}}\right) \right) + EI \left(1 - \frac{L_1}{\bar{L}} + \frac{1}{2\pi} \sin\left(\frac{2\pi L_1}{\bar{L}}\right) \right) \tag{6-102}$$

It is assumed that the axial load is constant and equal to N_m which will give a moment in the column equal to

$$M = N_m \cdot u = N_m \cdot \delta \cdot \sin\left(\frac{\pi x}{\bar{L}}\right) = N_m \cdot \frac{\delta}{1 - N_m / N_E} \cdot \sin\left(\frac{\pi x}{\bar{L}}\right) \tag{6-103}$$

If the moment given by Equation (6-103) exceeds the moment capacity of the cross-section, a transition from progressive to global buckling will occur. In the undeformed part of the column, a linear interaction between the moment and the axial load is assumed

$$\frac{N}{N_p} + \frac{M}{M_p} = 1 \implies M_{cap} = M_p \left[1 - \frac{N_m}{N_p} \right] \tag{6-104}$$

To determine the moment capacity of the compressed part of the column, $0 \leq x \leq L_1$, the moment-rotation relationship for $N = N_m$ is establish as described in Section 6.3.2.2. The capacity is taken when "yielding" takes place, i.e. $M_{cap} = M_y$.

The procedure described in Section 6.3.2.3 is used to calculate the critical length, only with a different transition criterion, i.e. $M \geq M_{cap}$.

In the experimental tests it was observed that the new lobes sometimes formed "off-centre". This will introduce imperfections and load eccentricity, which will decrease the stability of the partly compressed column.

To account for the imperfections and the formation of lobes "off-centre" it is assumed that the initial imperfection amplitude will increase during the deformation of the column. It is assumed that the initial imperfection will start with a value equal to δ_{00} and increase to δ_{0f}. The increase in initial imperfection amplitude is given by

$$\delta_0 = \delta_{00}\left(1 - \frac{w}{0.73L}\right) + \delta_{0f}\frac{w}{0.73L} \qquad (6\text{-}105)$$

Here $\delta_{00} = L/1000$ and $\delta_{0f} = L/100$ has been used. The results from the model are very dependent on the choice of imperfections. The critical slenderness found by the model is especially dependent on the value chosen for δ_{0f}. This value can be based on the measured imperfections from experimental tests, or it can be adjusted to calibrate for the observed response.

In Figure 6-16 the model is compared with the results for members collapsing in either a progressive or in a transition mode.

A relatively good agreement is found between the model and the experimental tests on columns with wall thickness 2.0 and 2.5 mm. However, the critical global slenderness is overestimated for members with wall thickness 3.5 mm.

In the model it is assumed that the column is free to rotate at both ends. In the experiments the lower end of the column is clamped. The upper end is neither free to rotate nor clamped. The boundary conditions will have some influence on the critical global slenderness.
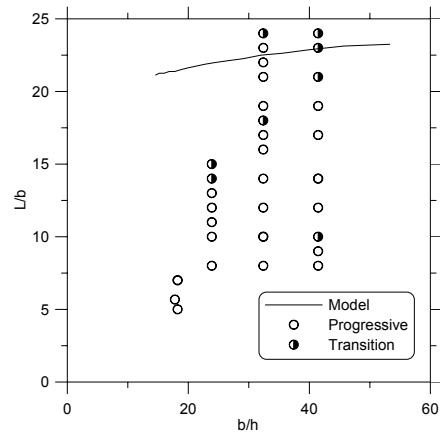
Figure 6-16 Comparison of experimental results and model.

6.3.4   Summary

In Figure 6-17 the results from two of the models (Section 6.3.1.5 and Section 6.3.3) are presented together with the collapse modes observed in the quasi-static tests.

The figure gives the collapse modes for columns with different local and global slenderness. Columns in the different regions in Figure 6-17a will collapse as follows:

A. Progressive buckling.
B. Transition from progressive to global buckling.
C. Columns without a trigger will collapse in direct global buckling, a triggered column will collapse in progressive buckling mode.
D. Columns without a trigger will collapse in direct global buckling, triggered columns will collapse in transition from progressive to global buckling.

a) Regions with different collapse modes   b) Comparison with experimental test results
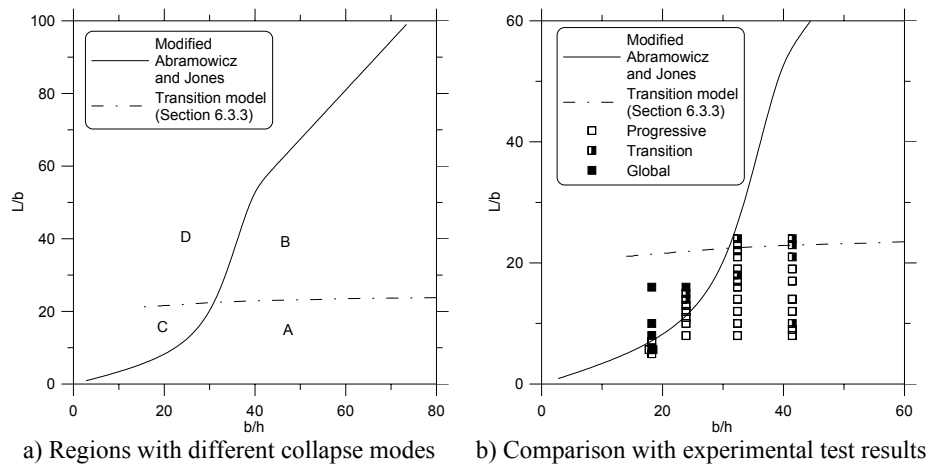
Figure 6-17 Regions with different collapse modes.

In region C and D it is assumed that a triggered specimen will not be subjected to direct global buckling, however, a transition from progressive to global buckling may occur after some deformation. A specimen in one of these regions without a trigger mechanism will be subjected to direct global buckling.

As can be seen from Figure 6-17b the models are in relatively good agreement with the collapse modes observed in the experimental tests.

7 Conclusions and recommendations for further work

7.1 Conclusions

An experimental study has been carried out to study the behaviour of axially loaded extrusion. Both quasi-static and dynamic tests have been performed and the primary variables have been the wall thickness of the extrusions and the impact velocity. The experimental tests have been used to validate a numerical model which has been used in a parametric study on the behaviour of axially loaded extrusions. The results can be summarized as follows:

- ➤ The collapse mode is very dependent on impact velocity.
- ➤ An increasing critical global slenderness as a function of the local slenderness was found in the quasi-static tests.
- ➤ At 13 m/s the critical global slenderness is increased compared to the quasi-static tests for members with a wall thickness of 3.5 mm and 4.5 mm and reduced for members with wall thicknesses of 2.0 mm and 2.5 mm.
- ➤ A decreasing critical global slenderness as a function of the local slenderness was found in the dynamic tests with an impact velocity of 20 m/s.
- ➤ Anomalous response was observed for all slenderness ratios, i.e. different collapse modes were found in parallel tests with the same local and global slenderness.
- ➤ LS-DYNA gives a relatively good description of the collapse mode found in the experimental tests. However, the mean force is underestimated when the baseline model is used.

- The mean force is increasing linearly with the impact velocity but the global stability will decrease and the response will be more anomalous when the impact velocity is increased.
- The use of heat induced triggers had a positive effect on the critical buckling length of the extruded members.
- The difference in structural effectiveness between members collapsing in a progressive mode and in a transition or direct global mode is increased for increasing solidity ratio.
- The difference in structural effectiveness for members collapsing in different collapse modes is decreasing for increasing impact velocity.
- Eurocode 9 (2004) gives conservative estimates of the buckling strength for members collapsing in a direct global mode.
- High variation in peak load was found for members collapsing in progressive buckling and in transition from progressive to global buckling. Some of the members collapsed at a load that was lower than the design values given by Eurocode 9 (2004).
- The analytical model for predicting progressive and global buckling gives a relatively good agreement with the experimental results.

7.2   Recommendations for further work

Based on the present project the following subjects need further investigation:

- The anomalous behaviour should be studied more closely. In order to ensure a robust design, simulations using stochastic variations on the most important parameters should be performed.
- More work on analytical models is required, both improving the model for transition and establishing a model for impact.
- Effect of triggers on critical buckling length and stability should be validated by experimental tests.

> ➢ The mean force found in the explicit numerical simulations of the impact tests under-estimates the mean force and the cause of this needs further investigation.

> ➢ A relatively large variation in critical stress was found for components collapsing in progressive buckling mode. As a result, Eurocode 9 gave non-conservative predictions of the buckling capacity of the extruded tubes.

8   References

Abramowicz W, 2003. *Thin-walled structures as impact energy absorbers*. Thin-walled structures 41, 91-107.

Abramowicz W & Jones N, 1984. *Dynamic axial crushing of square tubes*. International Journal of Impact Engineering 2 (2), 179-208.

Abramowicz W & Jones N, 1986. *Dynamic progressive buckling of circular and square tubes*. International Journal of Impact Engineering 4 (4), 243-270.

Abramowicz W & Jones N, 1997. *Transition from initial global bending to progressive buckling of tubes loaded statically and dynamically*. International Journal of Impact Engineering 19 (5-6), 415-437.

Alghamdi AAA, 2001. *Collapsible impact energy absorbers: an overview*. Thin-walled structures 39 (2), 189-213.

Bergan PG & Syvertsen TG, 1977. *Knekkingsberegning ved bruk av differensialligning*, Knekking av søyler og rammer. Tapir, Trondheim.

Bjørneklett BI & Myhr OR, 2003. *Material design and thermally induced triggers in crash management*. International body engineering conference, Tokyo

Enjalbert P, 2003. Strain-rate sensitivity of aluminium alloy AA6060-T6. Master Thesis NTNU,

Eurocode 9, 2004. Design of aluminium structures, Part 1.1:General structural rules prEN 1999-1-1 (stage34). European Commitee for Standardisation, CEN.

Gaylord jr EH & Gaylord CN, 1972. *Inelastic buckling of columns*, Design of Steel Structures. McGraw-Hill book company,

Gupta NK & Abbas A, 2001. *Some considerations on axisymmetric folding of metallic round tubes*. International Journal of Impact Engineering 25, 331-334.

Hallquist JO, 1998. *LS-DYNA Theoretical Manual*. Livermore Software Technology Corporation, California.

References

Hallquist JO, 2003. *LS-DYNA Keyword User's Manual, Version 970*. Livermore Software Technology Corporation, California.

Hanssen AG, Auestad T, Tryland T & Langseth M, 2003. *The kicking machine: A device for impact testing of structural components*. International Journal of Crashworthiness 8 (4)

Hanssen AG, Langseth M & Hopperstad OS, 2000. *Static and dynamic crushing of square aluminium extrusions with aluminium foam filler*. International Journal of Impact Engineering 24 (4), 347-383.

Hosford WF & Caddel RM, 1993. *Metal Forming: Mechanics and Metallurgy*, Second edition, PRT Prentice Hall, ISBN 0-13-588526-4.

Hsu SS & Jones N, 2003. *Dynamic axial impact loading of 6061-T6 aluminium alloy cylindrical shells*. In: Proceedings of 8th International Symposium on IMPLAST 2003. N K Gupta (ed.), Phoenix Publishing House PVT LTD, New Delhi.

Hsu SS & Jones N, 2004. *Quasi-static and dynamic axial crushing of thin-walled circular stainless steel, mild steel and aluminium alloy tubes*. International Journal of Crashworthiness 9 (2), 195-217.

Iyengar NGR, 1988. Structural Stability of Columns and Plates. Wiley, New York.

Johnson W & Reid SR, 1978. *Metallic Energy Dissipating Systems*. Applied Mechanics Reviews 31 (3), 277-288.

Johnson W & Reid SR, 1986. *Update to "Metallic energy dissipating systems" [AMR 31 (1978):277-288]*. Applied Mechanics Update , 315-319.

Jones N, 1989. *Dynamic progressive buckling*, Structural Impact. Cambridge University Press, Cambridge. 385-432, ISBN 0-521-62890-3.

Jones N, 2003. *Several phenomena in structural impact and structural crashworthiness*. European Journal of Mechanics A/Solids 22, 693-707.

Karagiozova D, 2003. *Velocity and mass sensitivity of circular and square tubes under axial impact*. In: Proceedings of 8th International Symposium on IMPLAST 2003. N K Gupta (ed.), Phoenix Publishing House PVT LTD, New Delhi.

Karagiozova D, 2004. *Dynamic buckling of elastic-plastic square tubes under axial impact-I: stress wave propagation phenomenon*. International Journal of Impact Engineering 30 (2), 143-166.

Karagiozova D & Alves M, 2004a. *Transition from progressive buckling to global bending of circular shells under axial impact-part I: Experimental and numerical observations*. International Journal of Solids and Structures 41 (5-6), 1565-1580.

Karagiozova D & Alves M, 2004b. *Transition from progressive buckling to global bending of circular shells under axial impact—Part II: Theoretical analysis*. International Journal of Solids and Structures 41 (5-6), 1581-1604.

Karagiozova D, Alves M & Jones N, 2000. *Inertia Effects in Axisymetrically Deformed Cylindrical Shells Under Axial Impact*. International Journal of Impact Engineering 24 (10), 1083-1115.

Karagiozova D & Jones N, 2001. *Dynamic effects on buckling and energy absorption of cylindrical shells under axial impact*. Thin-Walled Structures 39 (7), 583-610.

Karagiozova D & Jones N, 2002. *On dynamic buckling phenomena in axially loaded elastic-plastic cylindrical shells*. International Journal of Non-Linear Mechanics 37 (7), 1223-1238.

Lademo O, 1999. *Engineering Models of Elastoplasticity and Fracture for Aluminium Alloys*. Dr Ing. Thesis, Department of Strucutral Engineering, Norwegian University of Science and Technology, Trondheim, Norway, ISBN 82-471-0367-2.

Langseth M & Hopperstad OS, 1996. *Static and Dynamic Axial Crushing of Square Thin-Walled Aluminium Extrusions*. International Journal of Impact Engineering 18 (7-8), 949-968.

Langseth M, Hopperstad OS & Berstad T, 1999. *Crashworthiness of aluminium extrusions: validation of numerical simulation, effect of mass ratio and impact velocity*. International Journal of Impact Engineering 22 (9-10), 829-854.

References

Larsen PK, 1997. *Inelastisk knekking av staver*, Dimensjonering av stålkonstruksjoner. Tapir Forlag, Trondheim, ISBN 82-519-0946-5.

Li S & Reid SR, 1990. *Relationship Between the Elastic Buckling of Square Tubes and Rectangular Plates*. Journal of Applied Mechanics 57, 969-973.

Mazzolani FM, 1985. The Structural Material, Aluminium Alloy Structures. E & FN Spon, London.

Phantom C, 2004. [cited 2004-10-30] Avaiable from Internet: <*http://www.visiblesolutions.com/*>

Reid SR, 1993. *Plastic deformation mechanisms in axially compressed metal tubes used as impact energy absorbers*. International Journal of Mechanical Sciences 35 (12), 1035-1052.

Reyes A, Hopperstad OS & Langseth M, 2004. *Aluminum foam-filled extrusions subjected to oblique loading: experimental and numerical study*. International Journal of Solids and Structures 41 (5-6), 1645-1675.

Reyes A, Langseth M & Hopperstad OS, 2002. *Crashworthiness of aluminum extrusions subjected to oblique loading: experiments and numerical analysis*. International Journal of Mechanical Sciences 44 (9), 1965-1984.

Reyes A, Langseth M & Hopperstad OS, 2003. *Square aluminum tubes subjected to oblique loading*. International Journal of Impact Engineering 28 (10), 1077-1106.

Shanley FR, 1947. *Inelastic column theory*. J Aero Sc 14, 261-267.

Søvik Opheim B, 1996. Bending of Thin-walled Aluminium Extrusions. Dr Ing. Thesis, Department of Strucutral Engineering, Norwegian University of Science and Technology, Trondheim, Norway, ISBN 82-7119-947-1.

Su XY, Yu TX & Reid SR, 1995. *Inertia-sensitive impact energy-absorbing structures Part II: Effect of strain rate*. International Journal of Impact Engineering 16 (4), 673-689.

Teramoto SS & Alves M, 2004. *Buckling transition of axially impacted open shells*. International Journal of Impact Engineering 30 (8-9), 1241-1260.

Timoshenko SP, 1982. *Euler's contribution to the strength of materials*, History of strength of materials. Dover, Toronto, ISBN 0-486-611-876.

Appendix A. Material tests

Table A-1 Material tests different thicknesses.

Test no.	σ_0	Q_1	C_1	Q_2	C_2	$\sigma_0 + \sum_i Q_i$	$\sigma_{0.2}$
	[N/mm^2]	[/mm^2]	[-]	[N/mm^2]	[-]	[N/mm^2]	[N/mm^2]
20-1	104	46	24	97	5216	249	203
20-2	122	47	24	81	6086	246	205
20-3	107	46	24	93	5201	262	202
25-1	115	68	19	79	7565	260	196
25-2	100	67	19	93	6081	259	195
25-3	95	65	19	99	5307	247	196
35-1	87	50	21	110	5226	244	199
35-2	104	49	22	92	5669	246	198
35-3	148	49	22	48	10492	250	199
45-1	90	47	24	114	4295	253	206
45-2	76	47	23	129	4132	251	208
45-3	75	47	23	129	3791	249	206

Table A-2 Material tests different directions.

Test no.	σ_0	Q_1	C_1	Q_2	C_2	$\sigma_0 + \sum_i Q_i$	$\sigma_{0.2}$
	[N/mm^2]	[N/mm^2]	[-]	[N/mm^2]	[-]	[N/mm^2]	[N/mm^2]
0-1	128	78	2749	49	21	255	208
0-2	153	53	2179	51	19	257	207
45-1	179	31	1201	42	20	252	209
45-2	166	44	1621	43	19	253	209
45-3	178	33	1413	43	19	253	210
90-1	167	38	1764	42	20	247	206
90-2	174	20	1347	43	20	247	204
90-3	180	25	1142	43	20	248	204
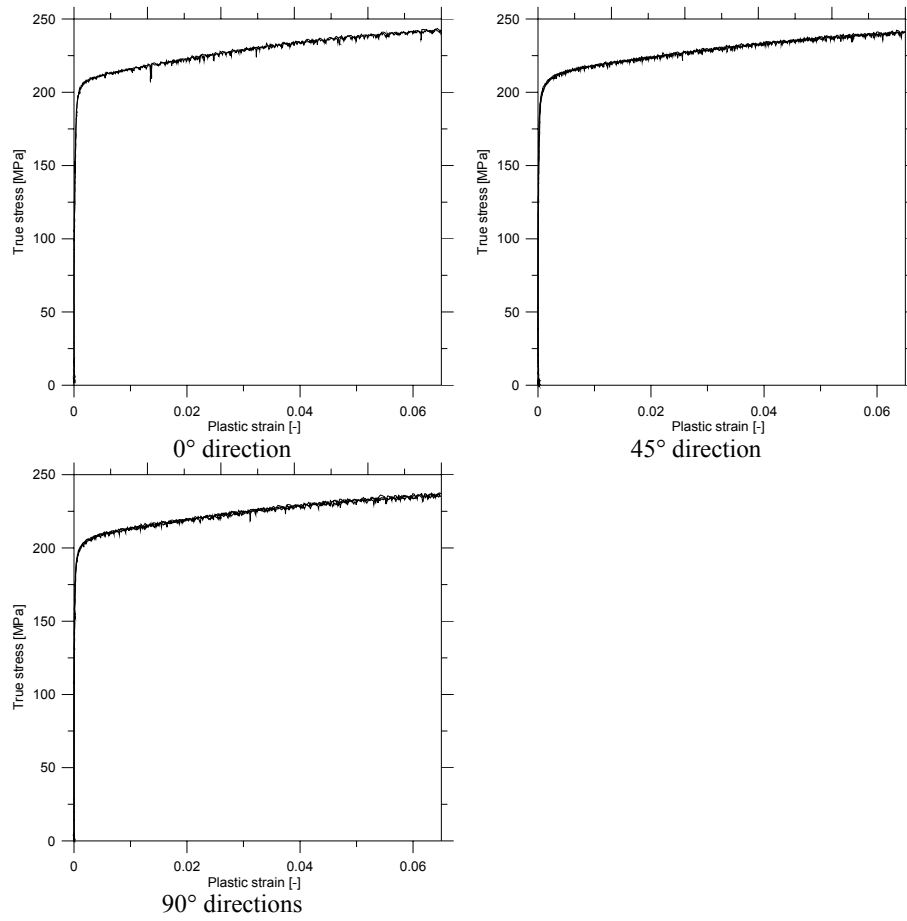
Figure A-1 Stress-strain curves from different directions.

h = 2.0 mm   h = 2.5 mm

h = 3.5 mm   h = 4.5 mm
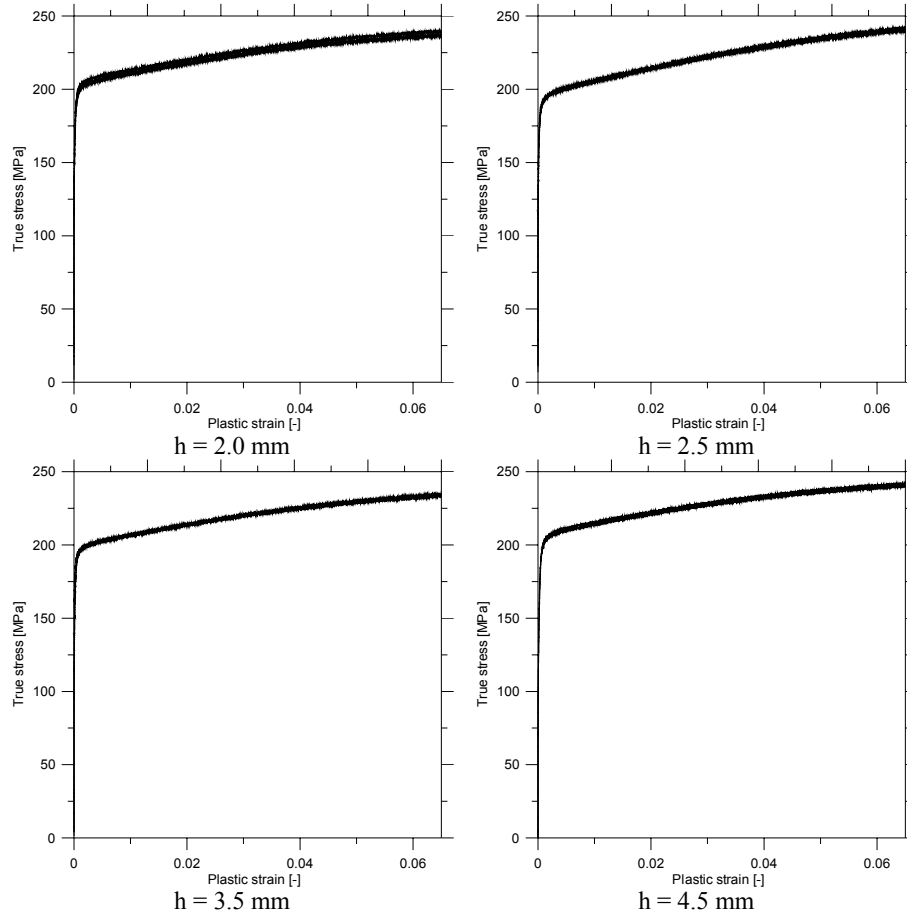
Figure A-2 Stress-strain curves from different thicknesses.

Appendix B.   Quasi-static tests

In the following tables a summary of the results together with a force-displacement plot and a picture of the deformed geometry will be presented. Test #, Length (L), Thickness (h), Deformation (δ), Peak Force (P_{max}), Mean Force (P_{mean}) and Collapse Mode is as defined in Table 4-1. In "Start Point" a "C" and "I" denotes that the deformation started at the clamped end and impacted end respectively.

Comments (in the tables):
1. Deformation started ca 15 cm from top.
2. Deformation started ca 50 cm from the lower end.

Test #	S1		Test #	S2	
Length	1280		Length	1278	
Thickness	4.5		Thickness	3.5	
Deformation	76		Deformation	138	
Peak Force	267		Peak Force	207	
Mean Force	99		Mean Force	39	
Collapse Mode	G		Collapse Mode	G	
Start point	-		Start point	-	
Comments	-		Comments	-	
Test #	S3		Test #	S4	
Length	959		Length	959	
Thickness	2.5		Thickness	2	
Deformation	718		Deformation	725	
Peak Force	136		Peak Force	91	
Mean Force	49		Mean Force	32	
Collapse Mode	P		Collapse Mode	P	
Start point	C		Start point	C	
Comments	-		Comments	-	
Test #	S5		Test #	S6	
Length	799		Length	802	
Thickness	4.5		Thickness	3.5	
Deformation	236		Deformation	595	
Peak Force	267		Peak Force	216	
Mean Force	60		Mean Force	87	
Collapse Mode	G		Collapse Mode	P	
Start point	-		Start point	C	
Comments	-		Comments	-	

Test #	S7			Test #	S8		
Length	799			Length	639		
Thickness	2.5			Thickness	4.5		
Deformation	605			Deformation	244		
Peak Force	111			Peak Force	284		
Mean Force	50			Mean Force	75		
Collapse Mode	P			Collapse Mode	G		
Start point	C			Start point	-		
Comments	-			Comments	-		
Test #	S9			Test #	S10		
Length	638			Length	800		
Thickness	2.5			Thickness	2		
Deformation	446			Deformation	335		
Peak Force	148			Peak Force	100		
Mean Force	50			Mean Force	25		
Collapse Mode	P			Collapse Mode	T		
Start point	C			Start point	I		
Comments	-			Comments	1		
Test #	S11			Test #	S12		
Length	800			Length	720		
Thickness	2.5			Thickness	2		
Deformation	610			Deformation	539		
Peak Force	146			Peak Force	94		
Mean Force	50			Mean Force	30		
Collapse Mode	P			Collapse Mode	P		
Start point	I			Start point	C		
Comments	-			Comments	-		

Test #	S13			Test #	S14		
Length	639			Length	638		
Thickness	3.5			Thickness	2		
Deformation	456			Deformation	455		
Peak Force	218			Peak Force	99		
Mean Force	85			Mean Force	35		
Collapse Mode	P			Collapse Mode	P		
Start point	C			Start point	C		
Comments	-			Comments	-		
Test #	S15			Test #	S16		
Length	1280			Length	1280		
Thickness	2			Thickness	2.5		
Deformation	477			Deformation	974		
Peak Force	102			Peak Force	147		
Mean Force	23			Mean Force	49		
Collapse Mode	T			Collapse Mode	P		
Start point	-			Start point	C		
Comments	2			Comments	-		
Test #	S17			Test #	S18		
Length	1120			Length	879		
Thickness	2			Thickness	3.5		
Deformation	900			Deformation	633		
Peak Force	96			Peak Force	201		
Mean Force	34			Mean Force	80		
Collapse Mode	P			Collapse Mode	P		
Start point	I			Start point	I		
Comments	-			Comments	-		

Test #	S19
Length	560
Thickness	4.5
Deformation	375
Peak Force	286
Mean Force	142
Collapse Mode	P
Start point	C
Comments	-

Test #	S20
Length	1120
Thickness	2.5
Deformation	860
Peak Force	136
Mean Force	50
Collapse Mode	P
Start point	-
Comments	-

Test #	S21
Length	1200
Thickness	2
Deformation	962
Peak Force	93
Mean Force	33
Collapse Mode	P
Start point	I
Comments	-

Test #	S22
Length	1360
Thickness	2
Deformation	1081
Peak Force	88
Mean Force	32
Collapse Mode	P
Start point	I
Comments	-

Test #	S23
Length	1438
Thickness	2.5
Deformation	492
Peak Force	143
Mean Force	43
Collapse Mode	T
Start point	I
Comments	1

Test #	S24
Length	1360
Thickness	2.5
Deformation	982
Peak Force	146
Mean Force	50
Collapse Mode	P
Start point	I
Comments	-

Test #	S25			
Length	1520			
Thickness	2			
Deformation	1222			
Peak Force	100			
Mean Force	35			
Collapse Mode	P			
Start point	I			
Comments	-			

Test #	S26			
Length	560			
Thickness	4.5			
Deformation	375			
Peak Force	290			
Mean Force	146			
Collapse Mode	P			
Start point	I			
Comments	-			

Test #	S27			
Length	480			
Thickness	4.5			
Deformation	251			
Peak Force	292			
Mean Force	81			
Collapse Mode	G			
Start point	-			
Comments	-			

Test #	S28			
Length	454			
Thickness	4.5			
Deformation	223			
Peak Force	288			
Mean Force	100			
Collapse Mode	G			
Start point	-			
Comments	-			

Test #	S29			
Length	454			
Thickness	4.5			
Deformation	249			
Peak Force	301			
Mean Force	147			
Collapse Mode	P			
Start point	C			
Comments	-			

Test #	S30			
Length	1040			
Thickness	3.5			
Deformation	741			
Peak Force	174			
Mean Force	76			
Collapse Mode	P			
Start point	I			
Comments	-			

Test #	S31	
Length	959	
Thickness	3.5	
Deformation	702	
Peak Force	207	
Mean Force	84	
Collapse Mode	P	
Start point	-	
Comments	-	

Test #	S32	
Length	1679	
Thickness	2	
Deformation	493	
Peak Force	82	
Mean Force	25	
Collapse Mode	T	
Start point	I	
Comments	-	

Test #	S33	
Length	1839	
Thickness	2	
Deformation	634	
Peak Force	93	
Mean Force	31	
Collapse Mode	T	
Start point	C	
Comments	-	

Test #	S34	
Length	1200	
Thickness	3.5	
Deformation	398	
Peak Force	177	
Mean Force	71	
Collapse Mode	T	
Start point	N	
Comments	-	

Test #	S35	
Length	1120	
Thickness	3.5	
Deformation	496	
Peak Force	185	
Mean Force	66	
Collapse Mode	T	
Start point	I	
Comments	-	

Test #	S36	
Length	1520	
Thickness	2.5	
Deformation	973	
Peak Force	151	
Mean Force	51	
Collapse Mode	P	
Start point	I	
Comments	-	

Test #	S37		Test #	S38	
Length	1760		Length	1680	
Thickness	2.5		Thickness	2.5	
Deformation	970		Deformation	740	
Peak Force	149		Peak Force	143	
Mean Force	49		Mean Force	47	
Collapse Mode	P		Collapse Mode	P	
Start point	I		Start point	C	
Comments	-		Comments	-	

Test #	S39		Test #	S40	
Length	400		Length	1919	
Thickness	4.5		Thickness	2	
Deformation	211		Deformation	233	
Peak Force	291		Peak Force	91	
Mean Force	146		Mean Force	26	
Collapse Mode	P		Collapse Mode	T	
Start point	C		Start point	I	
Comments	-		Comments	-	

Test #	S41		Test #	S42	
Length	1919		Length	1840	
Thickness	2.5		Thickness	2.5	
Deformation	232		Deformation	726	
Peak Force	140		Peak Force	145	
Mean Force	43		Mean Force	49	
Collapse Mode	T		Collapse Mode	P	
Start point	-		Start point	I	
Comments	2		Comments	-	

Appendix C.   Dynamic tests V13

In the following tables a summary of the results together with a force-displacement plot and a picture of the deformed geometry will be presented. Test #, Length (L), Thickness (h), Buffer distance (l_b), Deformation (d_b), Accuracy (Δ_b), Mean Force (P_{mean}) and Collapse Mode is as defined in Table 4-2. In "Start Point" a "C" and "I" denotes that the deformation started at the clamped end and impacted end respectively.

Comments (in the tables):
1. No film.
2. Lobes start forming at both ends after some time.
3. No force signal recorded.
4. Load cell destroyed.
5. Bad strain gauges.

Test #	D1-1
Length	1598
Thickness	2.5
Buffer distance	939
Deformation	951
Accuracy	1.01
Mean Force	51
Collapse Mode	T
Start point	C
Comments	-

Test #	D1-2
Length	1360
Thickness	2.5
Buffer distance	751
Deformation	751
Accuracy	1.00
Mean Force	57
Collapse Mode	T
Start point	C
Comments	1

Test #	D1-3
Length	1597
Thickness	2
Buffer distance	940
Deformation	934
Accuracy	0.99
Mean Force	33
Collapse Mode	T
Start point	-
Comments	1

Test #	D1-4
Length	1598
Thickness	4.5
Buffer distance	942
Deformation	309
Accuracy	-
Mean Force	99
Collapse Mode	G
Start point	-
Comments	-

Test #	D1-5
Length	1359
Thickness	2
Buffer distance	873
Deformation	848
Accuracy	0.97
Mean Force	38
Collapse Mode	P
Start point	C
Comments	-

Test #	D1-6
Length	1598
Thickness	3.5
Buffer distance	1015
Deformation	904
Accuracy	0
Mean Force	98
Collapse Mode	T
Start point	C
Comments	2

Test #	D1-7		Test #	D1-8	
Length	1358		Length	1199	
Thickness	3.5		Thickness	4.5	
Buffer distance	732		Buffer distance	684	
Deformation	705		Deformation	393	
Accuracy	0.96		Accuracy	-	
Mean Force	96		Mean Force	86	
Collapse Mode	P		Collapse Mode	G	
Start point	C		Start point	-	
Comments	-		Comments	-	
Test #	D1-9		Test #	D1-10	
Length	799		Length	1201	
Thickness	4.5		Thickness	3.5	
Buffer distance	426		Buffer distance	693	
Deformation	-		Deformation	680	
Accuracy	-		Accuracy	0.98	
Mean Force	-		Mean Force	94	
Collapse Mode	P		Collapse Mode	P	
Start point	I		Start point	C	
Comments	3		Comments	1	
Test #	D1-11		Test #	D1-12	
Length	798		Length	1198	
Thickness	3.5		Thickness	2	
Buffer distance	370		Buffer distance	685	
Deformation	357		Deformation	676	
Accuracy	0.97		Accuracy	0.99	
Mean Force	104		Mean Force	37	
Collapse Mode	P		Collapse Mode	P	
Start point	C		Start point	C	
Comments	-		Comments	-	

Test #	D1-13		Test #	D1-14	
Length	1361		Length	1040	
Thickness	4.5		Thickness	4.5	
Buffer distance	979		Buffer distance	507	
Deformation	462		Deformation	-	
Accuracy	0		Accuracy	-	
Mean Force	85		Mean Force	-	
Collapse Mode	G		Collapse Mode	P	
Start point	-		Start point	-	
Comments	4		Comments	5	
Test #	D1-15		Test #	D1-16	
Length	959		Length	1380	
Thickness	4.5		Thickness	3.5	
Buffer distance	407		Buffer distance	850	
Deformation	-		Deformation	-	
Accuracy	-		Accuracy	-	
Mean Force	-		Mean Force	-	
Collapse Mode	G		Collapse Mode	P	
Start point	-		Start point	C	
Comments	5		Comments	5	
Test #	D1-17		Test #	D1-18	
Length	958		Length	1120	
Thickness	2.5		Thickness	3.5	
Buffer distance	490		Buffer distance	690	
Deformation	-		Deformation	666	
Accuracy	-		Accuracy	0.97	
Mean Force	-		Mean Force	95	
Collapse Mode	P		Collapse Mode	P	
Start point	C		Start point	C	
Comments	5		Comments	-	

Test #	D1-19
Length	880
Thickness	3.5
Buffer distance	440
Deformation	434
Accuracy	0.99
Mean Force	91
Collapse Mode	P
Start point	C
Comments	-

Test #	D1-20
Length	1437
Thickness	2
Buffer distance	904
Deformation	898
Accuracy	0.99
Mean Force	39
Collapse Mode	P
Start point	C
Comments	-

Test #	D1-21
Length	1197
Thickness	2.5
Buffer distance	745
Deformation	736
Accuracy	0.99
Mean Force	56
Collapse Mode	P
Start point	C
Comments	-

Test #	D1-22
Length	1440
Thickness	3.5
Buffer distance	925
Deformation	903
Accuracy	0.98
Mean Force	86
Collapse Mode	P
Start point	C
Comments	-

Test #	D1-23
Length	1280
Thickness	2.5
Buffer distance	800
Deformation	787
Accuracy	0.98
Mean Force	56
Collapse Mode	P
Start point	C
Comments	-

Test #	D1-24
Length	1120
Thickness	2.5
Buffer distance	696
Deformation	689
Accuracy	0.99
Mean Force	57
Collapse Mode	P
Start point	C
Comments	-

Test #	D1-25		Test #	D1-26
Length	1520		Length	1118
Thickness	2		Thickness	4.5
Buffer distance	990		Buffer distance	670
Deformation	982		Deformation	290
Accuracy	0.99		Accuracy	0
Mean Force	31		Mean Force	151
Collapse Mode	T		Collapse Mode	T
Start point	C		Start point	C
Comments	-		Comments	-

Test #	D1-27		Test #	D1-28
Length	958		Length	878
Thickness	4.5		Thickness	4.5
Buffer distance	527		Buffer distance	490
Deformation	515		Deformation	221
Accuracy	0.98		Accuracy	0
Mean Force	159		Mean Force	90
Collapse Mode	P		Collapse Mode	G
Start point	I		Start point	-
Comments	-		Comments	-

Test #	D1-29		Test #	D1-30
Length	1280		Length	680
Thickness	2		Thickness	4.5
Buffer distance	745		Buffer distance	260
Deformation	-		Deformation	-
Accuracy	-		Accuracy	-
Mean Force	-		Mean Force	-
Collapse Mode	P		Collapse Mode	P
Start point	C		Start point	-
Comments	5		Comments	5

Appendix D. Dynamic tests V20

In the following tables a summary of the results together with a force-displacement plot and a picture of the deformed geometry will be presented. Test #, Length (L), Thickness (h), Buffer distance (l_b), Deformation (d_b), Accuracy (Δ_b), Mean Force (P_{mean}) and Collapse Mode is as defined in Table 4-3. In "Start Point" a "C" and "I" denotes that the deformation started at the clamped end and impacted end respectively.

Comments (in the tables):
1. Missing force signal and time.
2. Specimen was not tested.

Test #	D2-1		Test #	D2-2
Length	640		Length	639
Thickness	4.5		Thickness	3.5
Buffer distance	355		Buffer distance	355
Deformation	343		Deformation	345
Accuracy	0.97		Accuracy	0.97
Mean force	172		Mean force	102
Collapse mode	P		Collapse mode	P
Start point	C		Start point	C
Comments	-		Comments	-

Test #	D2-3		Test #	D2-4
Length	639		Length	639
Thickness	4.5		Thickness	2.5
Buffer distance	355		Buffer distance	380
Deformation	352		Deformation	368
Accuracy	0.99		Accuracy	0.97
Mean force	167		Mean force	58
Collapse mode	P		Collapse mode	P
Start point	I		Start point	C
Comments	-		Comments	-

Test #	D2-5		Test #	D2-6
Length	800		Length	638
Thickness	3.5		Thickness	2
Buffer distance	441		Buffer distance	322
Deformation	431		Deformation	316
Accuracy	0.98		Accuracy	0.98
Mean force	97		Mean force	41
Collapse mode	P		Collapse mode	P
Start point	C		Start point	C
Comments	-		Comments	-

Test #	D2-7		Test #	D2-8	
Length	800		Length	799	
Thickness	4.5		Thickness	2.5	
Buffer distance	442		Buffer distance	462	
Deformation	430		Deformation	453	
Accuracy	0.97		Accuracy	0.98	
Mean force	161		Mean force	57	
Collapse mode	P		Collapse mode	P	
Start point	C		Start point	I	
Comments	-		Comments	-	

Test #	D2-9		Test #	D2-10	
Length	800		Length	959	
Thickness	2		Thickness	4.5	
Buffer distance	536		Buffer distance	541	
Deformation	530		Deformation	546	
Accuracy	0.99		Accuracy	1.01	
Mean force	42		Mean force	151	
Collapse mode	T		Collapse mode	P	
Start point	I		Start point	C	
Comments	-		Comments	-	

Test #	D2-11		Test #	D2-12	
Length	960		Length	720	
Thickness	3.5		Thickness	2	
Buffer distance	588		Buffer distance	-	
Deformation	588		Deformation	-	
Accuracy	1.00		Accuracy	-	
Mean force	95		Mean force	-	
Collapse mode	P		Collapse mode	-	
Start point	C		Start point	-	
Comments	-		Comments	2	

Test #	D2-13		Test #	D2-14	
Length	1119		Length	1120	
Thickness	4.5		Thickness	3.5	
Buffer distance	707		Buffer distance	725	
Deformation	703		Deformation	724	
Accuracy	0.99		Accuracy	1.00	
Mean force	148		Mean force	91	
Collapse mode	P		Collapse mode	P	
Start point	I		Start point	C	
Comments	-		Comments	-	
Test #	D2-15		Test #	D2-16	
Length	1117		Length	879	
Thickness	2.5		Thickness	2	
Buffer distance	708		Buffer distance	469	
Deformation	706		Deformation	465	
Accuracy	1.00		Accuracy	0.99	
Mean force	56		Mean force	36	
Collapse mode	P		Collapse mode	P	
Start point	I		Start point	I	
Comments	-		Comments	-	
Test #	D2-17		Test #	D2-18	
Length	1440		Length	1437	
Thickness	3.5		Thickness	4.5	
Buffer distance	805		Buffer distance	790	
Deformation	794		Deformation	834	
Accuracy	0.99		Accuracy	1.06	
Mean force	92		Mean force	146	
Collapse mode	P		Collapse mode	P	
Start point	C		Start point	C	
Comments	-		Comments	-	

Test #	D2-19		Test #	D2-20
Length	1438		Length	1280
Thickness	2.5		Thickness	2.5
Buffer distance	860		Buffer distance	620
Deformation	480		Deformation	614
Accuracy	-		Accuracy	0.99
Mean force	59		Mean force	53
Collapse mode	T		Collapse mode	P
Start point	I		Start point	I
Comments	-		Comments	-

Test #	D2-21		Test #	D2-22
Length	1119		Length	1600
Thickness	2		Thickness	3.5
Buffer distance	580		Buffer distance	940
Deformation	572		Deformation	928
Accuracy	0.99		Accuracy	0.99
Mean force	36		Mean force	66
Collapse mode	P		Collapse mode	T
Start point	-		Start point	-
Comments	-		Comments	-

Test #	D2-23		Test #	D2-24
Length	1602		Length	1761
Thickness	4.5		Thickness	4.5
Buffer distance	818		Buffer distance	800
Deformation	848		Deformation	788
Accuracy	1.04		Accuracy	0.99
Mean force	142		Mean force	155
Collapse mode	P		Collapse mode	P
Start point	C		Start point	C
Comments	-		Comments	-

Test #	D2-25
Length	1440
Thickness	2
Buffer distance	868
Deformation	848
Accuracy	0.98
Mean force	42
Collapse mode	P
Start point	I
Comments	-

Test #	D2-26
Length	799
Thickness	2
Buffer distance	364
Deformation	375
Accuracy	1.03
Mean force	38
Collapse mode	P
Start point	I
Comments	-

Test #	D2-27
Length	1359
Thickness	2.5
Buffer distance	700
Deformation	684
Accuracy	0.98
Mean force	56
Collapse mode	T
Start point	C
Comments	-

Test #	D2-28
Length	1519
Thickness	3.5
Buffer distance	980
Deformation	976
Accuracy	1.00
Mean force	88
Collapse mode	P
Start point	C
Comments	-

Test #	D2-29
Length	1840
Thickness	4.5
Buffer distance	805
Deformation	854
Accuracy	1.06
Mean force	143
Collapse mode	P
Start point	C
Comments	-

Test #	D2-30
Length	1920
Thickness	4.5
Buffer distance	1443
Deformation	415
Accuracy	-
Mean force	153
Collapse mode	T
Start point	C
Comments	-

Test #	D2-31			Test #	D2-32	
Length	1760			Length	1839	
Thickness	3.5			Thickness	3.5	
Buffer distance	1100			Buffer distance	1199	
Deformation	1088			Deformation	1169	
Accuracy	0.99			Accuracy	0.97	
Mean force	89			Mean force	93	
Collapse mode	P			Collapse mode	T	
Start point	C			Start point	C	
Comments	-			Comments	-	
Test #	D2-33			Test #	D2-34	
Length	1919			Length	1438	
Thickness	3.5			Thickness	2	
Buffer distance	1289			Buffer distance	840	
Deformation	1251			Deformation	822	
Accuracy	0.97			Accuracy	0.98	
Mean force	72			Mean force	31	
Collapse mode	T			Collapse mode	T	
Start point	I			Start point	I	
Comments	-			Comments	-	
Test #	D2-35			Test #	D2-36	
Length	1520			Length	1279	
Thickness	2			Thickness	2	
Buffer distance	1025			Buffer distance	876	
Deformation	-			Deformation	535	
Accuracy	-			Accuracy	-	
Mean force	-			Mean force	35	
Collapse mode	T			Collapse mode	T	
Start point	I			Start point	I	
Comments	1			Comments	-	

"Reliability Analysis of Structural Systems using Nonlinear Finite Element Methods",
C. A. Holm, 1990:23, ISBN 82-7119-178-0.

"Uniform Stratified Flow Interaction with a Submerged Horizontal Cylinder",
Ø. Arntsen, 1990:32, ISBN 82-7119-188-8.

"Large Displacement Analysis of Flexible and Rigid Systems Considering Displacement-Dependent Loads and Nonlinear Constraints", K. M. Mathisen, 1990:33, ISBN 82-7119-189-6.

"Solid Mechanics and Material Models including Large Deformations",
E. Levold, 1990:56, ISBN 82-7119-214-0, ISSN 0802-3271.

"Inelastic Deformation Capacity of Flexurally-Loaded Aluminium Alloy Structures",
T. Welo, 1990:62, ISBN 82-7119-220-5, ISSN 0802-3271.

"Visualization of Results from Mechanical Engineering Analysis",
K. Aamnes, 1990:63, ISBN 82-7119-221-3, ISSN 0802-3271.

"Object-Oriented Product Modeling for Structural Design",
S. I. Dale, 1991:6, ISBN 82-7119-258-2, ISSN 0802-3271.

"Parallel Techniques for Solving Finite Element Problems on Transputer Networks",
T. H. Hansen, 1991:19, ISBN 82-7119-273-6, ISSN 0802-3271.

"Statistical Description and Estimation of Ocean Drift Ice Environments",
R. Korsnes, 1991:24, ISBN 82-7119-278-7, ISSN 0802-3271.

"Properties of concrete related to fatigue damage: with emphasis on high strength concrete",
G. Petkovic, 1991:35, ISBN 82-7119-290-6, ISSN 0802-3271.

"Turbidity Current Modelling",
B. Brørs, 1991:38, ISBN 82-7119-293-0, ISSN 0802-3271.

"Zero-Slump Concrete: Rheology, Degree of Compaction and Strength. Effects of Fillers as Part Cement-Replacement",
C. Sørensen, 1992:8, ISBN 82-7119-357-0, ISSN 0802-3271.

"Nonlinear Analysis of Reinforced Concrete Structures Exposed to Transient Loading",
K. V. Høiseth, 1992:15, ISBN 82-7119-364-3, ISSN 0802-3271.

"Finite Element Formulations and Solution Algorithms for Buckling and Collapse Analysis of Thin Shells", R. O. Bjærum, 1992:30, ISBN 82-7119-380-5, ISSN 0802-3271.

"Response Statistics of Nonlinear Dynamic Systems",
J. M. Johnsen, 1992:42, ISBN 82-7119-393-7, ISSN 0802-3271.

"Digital Models in Engineering. A Study on why and how engineers build and operate digital models for decisison support", J. Høyte, 1992:75, ISBN 82-7119-429-1, ISSN 0802-3271.

"Sparse Solution of Finite Element Equations",
A. C. Damhaug, 1992:76, ISBN 82-7119-430-5, ISSN 0802-3271.

"Some Aspects of Floating Ice Related to Sea Surface Operations in the Barents Sea",
S. Løset, 1992:95, ISBN 82-7119-452-6, ISSN 0802-3271.

"Modelling of Cyclic Plasticity with Application to Steel and Aluminium Structures",
O. S. Hopperstad, 1993:7, ISBN 82-7119-461-5, ISSN 0802-3271.

"The Free Formulation: Linear Theory and Extensions with Applications to Tetrahedral Elements
with Rotational Freedoms", G. Skeie, 1993:17, ISBN 82-7119-472-0, ISSN 0802-3271.

"Høyfast betongs motstand mot piggdekkslitasje. Analyse av resultater fra prøving i Veisliter'n",
T. Tveter, 1993:62, ISBN 82-7119-522-0, ISSN 0802-3271.

"A Nonlinear Finite Element Based on Free Formulation Theory for Analysis of Sandwich Structures", O. Aamlid, 1993:72, ISBN 82-7119-534-4, ISSN 0802-3271.

"The Effect of Curing Temperature and Silica Fume on Chloride Migration and Pore Structure of High Strength Concrete", C. J. Hauck, 1993:90, ISBN 82-7119-553-0, ISSN 0802-3271.

"Failure of Concrete under Compressive Strain Gradients",
G. Markeset, 1993:110, ISBN 82-7119-575-1, ISSN 0802-3271.

"An experimental study of internal tidal amphidromes in Vestfjorden",
J. H. Nilsen, 1994:39, ISBN 82-7119-640-5, ISSN 0802-3271.

"Structural analysis of oil wells with emphasis on conductor design",
H. Larsen, 1994:46, ISBN 82-7119-648-0, ISSN 0802-3271.

"Adaptive methods for non-linear finite element analysis of shell structures",
K. M. Okstad, 1994:66, ISBN 82-7119-670-7, ISSN 0802-3271.

"On constitutive modelling in nonlinear analysis of concrete structures",
O. Fyrileiv, 1994:115, ISBN 82-7119-725-8, ISSN 0802-3271.

"Fluctuating wind load and response of a line-like engineering structure with emphasis on
motion-induced wind forces",
J. Bogunovic Jakobsen, 1995:62, ISBN 82-7119-809-2, ISSN 0802-3271.

"An experimental study of beam-columns subjected to combined torsion, bending and axial actions", A. Aalberg, 1995:66, ISBN 82-7119-813-0, ISSN 0802-3271.

"Scaling and cracking in unsealed freeze/thaw testing of Portland cement and silica fume concretes", S. Jacobsen, 1995:101, ISBN 82-7119-851-3, ISSN 0802-3271.

"Damping of water waves by submerged vegetation. A case study of laminaria hyperborea",
A. M. Dubi, 1995:108, ISBN 82-7119-859-9, ISSN 0802-3271.

"The dynamics of a slope current in the Barents Sea",
Sheng Li, 1995:109, ISBN 82-7119-860-2, ISSN 0802-3271.

"Modellering av delmaterialenes betydning for betongens konsistens",
Ernst Mørtsell, 1996:12, ISBN 82-7119-894-7, ISSN 0802-3271.

"Bending of thin-walled aluminium extrusions",
Birgit Søvik Opheim, 1996:60, ISBN 82-7119-947-1, ISSN 0802-3271.

"Material modelling of aluminium for crashworthiness analysis",
Torodd Berstad, 1996:89, ISBN 82-7119-980-3, ISSN 0802-3271.

"Estimation of structural parameters from response measurements on submerged floating tunnels",
Rolf Magne Larssen, 1996:119, ISBN 82-471-0014-2, ISSN 0802-3271.

"Numerical modelling of plain and reinforced concrete by damage mechanics",
Mario A. Polanco-Loria, 1997:20, ISBN 82-471-0049-5, ISSN 0802-3271.

"Nonlinear random vibrations - numerical analysis by path integration methods",
Vibeke Moe, 1997:26, ISBN 82-471-0056-8, ISSN 0802-3271.

"Numerical prediction of vortex-induced vibration by the finite element method",
Joar Martin Dalheim, 1997:63, ISBN 82-471-0096-7, ISSN 0802-3271.

"Time domain calculations of buffeting response for wind sensitive structures",
Ketil Aas-Jakobsen, 1997:148, ISBN 82-471-0189-0, ISSN 0802-3271.

"A numerical study of flow about fixed and flexibly mounted circular cylinders",
Trond Stokka Meling, 1998:48, ISBN 82-471-0244-7, ISSN 0802-3271.

"Estimation of chloride penetration into concrete bridges in coastal areas",
Per Egil Steen, 1998:89, ISBN 82-471-0290-0, ISSN 0802-3271.

"Stress-resultant material models for reinforced concrete plates and shells",
Jan Arve Øverli, 1998:95, ISBN 82-471-0297-8, ISSN 0802-3271.

"Chloride binding in concrete. Effect of surrounding environment and concrete composition",
Claus Kenneth Larsen, 1998:101, ISBN 82-471-0337-0, ISSN 0802-3271.

"Rotational capacity of aluminium alloy beams",
Lars A. Moen, 1999:1, ISBN 82-471-0365-6, ISSN 0802-3271.

"Stretch Bending of Aluminium Extrusions",
Arild H. Clausen, 1999:29, ISBN 82-471-0396-6, ISSN 0802-3271.

"Aluminium and Steel Beams under Concentrated Loading",

Tore Tryland, 1999:30, ISBN 82-471-0397-4, ISSN 0802-3271.

"Engineering Models of Elastoplasticity and Fracture for Aluminium Alloys",
Odd-Geir Lademo, 1999:39, ISBN 82-471-0406-7, ISSN 0802-3271.

"Kapasitet og duktilitet av dybelforbindelser i trekonstruksjoner",
Jan Siem, 1999:46, ISBN 82-471-0414-8, ISSN 0802-3271.

"Etablering av distribuert ingeniørarbeid; Teknologiske og organisatoriske
erfaringer fra en norsk ingeniørbedrift", Lars Line, 1999:52, ISBN 82-471-0420-2,
ISSN 0802-3271.

"Estimation of Earthquake-Induced Response",
Símon Ólafsson, 1999:73, ISBN 82-471-0443-1, ISSN 0802-3271.

"Coastal Concrete Bridges: Moisture State, Chloride Permeability and Aging
Effects"
Ragnhild Holen Relling, 1999:74, ISBN 82-471-0445-8, ISSN 0802-3271.

"Capacity Assessment of Titanium Pipes Subjected to Bending and External
Pressure",
Arve Bjørset, 1999:100, ISBN 82-471-0473-3, ISSN 0802-3271.

"Validation of Numerical Collapse Behaviour of Thin-Walled Corrugated Panels",
Håvar Ilstad, 1999:101, ISBN 82-471-0474-1, ISSN 0802-3271.

"Strength and Ductility of Welded Structures in Aluminium Alloys",
Miroslaw Matusiak, 1999:113, ISBN 82-471-0487-3, ISSN 0802-3271.

"Thermal Dilation and Autogenous Deformation as Driving Forces to Self-Induced
Stresses in High Performance Concrete",
Øyvind Bjøntegaard, 1999:121, ISBN 82-7984-002-8, ISSN 0802-3271.

"Some Aspects of Ski Base Sliding Friction and Ski Base Structure",
Dag Anders Moldestad, 1999:137, ISBN 82-7984-019-2, ISSN 0802-3271.

"Electrode reactions and corrosion resistance for steel in mortar and concrete",
Roy Antonsen, 2000:10, ISBN 82-7984-030-3, ISSN 0802-3271.

"Hydro-Physical Conditions in Kelp Forests and the Effect on Wave Damping and
Dune Erosion. A case study on Laminaria Hyperborea",
Stig Magnar Løvås, 2000:28, ISBN 82-7984-050-8, ISSN 0802-3271.

"Random Vibration and the Path Integral Method",
Christian Skaug, 2000:39, ISBN 82-7984-061-3, ISSN 0802-3271.

"Buckling and geometrical nonlinear beam-type analyses of timber structures",
Trond Even Eggen, 2000:56, ISBN 82-7984-081-8, ISSN 0802-3271.

"Structural Crashworthiness of Aluminium Foam-Based Components",
Arve Grønsund Hanssen, 2000:76, ISBN 82-7984-102-4, ISSN 0809-103X.

"Measurements and simulations of the consolidation in first-year sea ice ridges,
and some aspects of mechanical behaviour", Knut V. Høyland, 2000:94, ISBN 82-
7984-121-0, ISSN 0809-103X.

"Kinematics in Regular and Irregular Waves based on a Lagrangian Formulation",
Svein Helge Gjøsund, 2000-86, ISBN 82-7984-112-1, ISSN 0809-103X.

"Self-Induced Cracking Problems in Hardening Concrete Structures",
Daniela Bosnjak, 2000-121, ISBN 82-7984-151-2, ISSN 0809-103X.

"Ballistic Penetration and Perforation of Steel Plates",
Tore Børvik, 2000:124, ISBN 82-7984-154-7, ISSN 0809-103X.

"Freeze-Thaw resistance of Concrete. Effect of: Curing Conditions, Moisture
Exchange and Materials", Terje Finnerup Rønning, 2001:14, ISBN 82-7984-165-2,
ISSN 0809-103X

Structural behaviour of post tensioned concrete structures. Flat slab. Slabs on
ground",
Steinar Trygstad, 2001:52, ISBN 82-471-5314-9, ISSN 0809-103X.

"Slipforming of Vertical Concrete Structures. Friction between concrete and
slipform panel",
Kjell Tore Fosså, 2001:61, ISBN 82-471-5325-4, ISSN 0809-103X.

"Some numerical methods for the simulation of laminar and turbulent incompressible
flows",
Jens Holmen, 2002:6, ISBN 82-471-5396-3, ISSN 0809-103X.

"Improved Fatigue Performance of Threaded Drillstring Connections by Cold
Rolling",
Steinar Kristoffersen, 2002:11, ISBN: 82-421-5402-1, ISSN 0809-103X.

"Deformations in Concrete Cantilever Bridges: Observations and Theoretical Modelling",
Peter F. Takâcs, 2002:23, ISBN 82-471-5415-3, ISSN 0809-103X.

"Stiffened aluminium plates subjected to impact loading",
Hilde Giæver Hildrum, 2002:69, ISBN 82-471-5467-6, ISSN 0809-103X.

"Full- and model scale study of wind effects on a medium-rise building in a built up area",
Jónas Thór Snæbjørnsson, 2002:95, ISBN82-471-5495-1, ISSN 0809-103X.

"Evaluation of Concepts for Loading of Hydrocarbons in Ice-infested water",
Arnor Jensen, 2002:114, ISBN 82-417-5506-0, ISSN 0809-103X.

"Numerical and Physical Modelling of Oil Spreading in Broken Ice",
Janne K. Økland Gjøsteen, 2002:130, ISBN 82-471-5523-0, ISSN 0809-103X.

"Diagnosis and protection of corroding steel in concrete",
Franz Pruckner, 20002:140, ISBN 82-471-5555-4, ISSN 0809-103X.

"Tensile and Compressive Creep of Young Concrete: Testing and Modelling",
Dawood Atrushi, 2003:17, ISBN 82-471-5565-6, ISSN 0809-103X.

"Rheology of Particle Suspensions. Fresh Concrete, Mortar and Cement Paste with Various Types of Lignosulfonates",
Jon Elvar Wallevik, 2003:18, ISBN 82-471-5566-4, ISSN 0809-103X.

"Oblique Loading of Aluminium Crash Components", Aase Reyes, 2003:15, ISBN 82-471-5562-1, ISSN 0809-103X.

"Utilization of Ethiopian Natural Pozzolans", Surafel Ketema Desta, 2003:26, ISSN 82-471-5574-5, ISSN:0809-103X.

"Behaviour and strength prediction of reinforced concrete structures with discontinuity regions", Helge Brå, 2004:11, ISBN 82-471-6222-9, ISSN 1503-8181.

"High-strength steel plates subjected to projectile impact. An experimental and numerical study", Sumita Dey, 2004:38, ISBN 82-471-6281-4 (elektr. Utg.), ISBN 82-471-6282-2 (trykt utg.),
ISSN 1503-8181.

"Alkali-reactive and inert fillers in concrete. Rheology of fresh mixtures and expansive reactions." Bård M. Pedersen, 2004:92, ISBN 82-471-6401-9 (trykt utg.), ISBN 82-471-6400-0 (elektr. utg.),
ISSN 1503-8181.

"On the Shear Capacity of Steel Girders with Large Web Openings". Nils Christian Hagen, 2005:9 ISBN 82-471-6878-2 (trykt utg.), ISBN 82-471-6877-4 (elektr. utg.), ISSN 1503-8181.